Reducing Fuel Evaporation Using Floating Objects

Janna Christine Wai

A dissertation

submitted in partial fulfillment of the

requirements for the degree of

Doctor of Philosophy

University of Washington

2022

Reading Committee:

Robert Breidenthal, Chair

Dana Dabiri

Mitsuru Kurosaka

Program Authorized to Offer Degree:

Aeronautics and Astronautics

University of Washington

Abstract

Reducing Fuel Evaporation Using Floating Objects

Janna Christine Wai

Chair of the Supervisory Committee:
Professor Robert Breidenthal
Aeronautics and Astronautics

A numerical investigation of the evaporation and mixing inside two fuel tank designs held at a constant pressure while varying the inlet speed. The cubic fuel tank is filled halfway with water while air is injected at a constant speed through a circular inlet, keeping the pressure inside the tank constant. The effect of adding floating objects on the water surface was investigated. It is found that the volume flow rate of water vapor decreases for inlet speeds less than Re = 340 and increases for speeds greater than Re = 340 for horizontal inlet flow. Adding floating objects to the water surface affected the volume flow rate and volume concentration of water vapor with dependencies on the shape and placement of the objects and the inlet speed.

TABLE OF CONTENTS

LIST OF FIGURES

LIST OF TABLES

ACKNOWLEDGEMENTS

This work was facilitated through the use of the advanced computational, storage, and networking infrastructure provided by the Hyak supercomputer system and funded by the STF at the University of Washington. And it would not have been possible without the support of many people throughout the years who provided guidance and encouragement to get me to this point.

First most, I would like to thank my adviser Robert Breidenthal. Long ago when he first suggested this project, I did not know what to expect. Over the years his sage-like advice helped push through all the setbacks and difficulties and helped me develop as a researcher. Thank you for your guidance, I enjoyed all of your jokes along the way.

I would also like to express gratitude to the rest of my graduate committee: Dana Dabiri, Mitsuru Kurosaka, Marco Salviato, and John Kramlich. Thank you for serving on my committee and helping me complete the program. Without their tough questions, I would not have been able to see the gaps in my understanding. To Jinkyu Yang and the late Kuen Lin, thank you for participating in the general and qualifying exams.

Also, I would like to recognize the individuals who contributed in meaningful ways. Giovanni Nino for always giving feedback and suggestions that were useful in moving the project along each week. Linda Hedges for your software advice and hints when I was starting out. And Fiona Spencer for helping refine my presentation.

To all my friends, a heartfelt thank you. There are so many of you that I cannot begin to name each person individually. Although you did not understand what I talked about most of the time,

you were always ready to listen over a good meal whenever I needed a break. And a special thanks to those who opened their homes and offices when I needed a place to work.

Finally, to my family, without them none of this would have been possible. To my father who answered most CFD questions and connected me with people who could answer specific questions. To my mother who took care of the tedious tasks for me. And to my brother who gave sound advice based on his experience getting the same degree and acted as my personal IT support. Thank you.

Chapter 1. INTRODUCTION

On July 17, 1996, Flight TWA 800 exploded and crashed into the Atlantic Ocean. All 230 people aboard the Boeing 747-131 died, making this the third-deadliest aviation accident in US history. Despite an extensive investigation, the exact cause of the explosion is still unknown [1]. One hypothesis is that the center fuel tank ruptured and allowed fuel vapor to leak where it was ignited by a source outside the tank. Then the fuel vapor trail carried the flame back into the tank where the majority of the fuel vapor was ignited [2].

The plane was delayed for five hours at John F. Kennedy International Airport in 90-95°F temperatures. The air-conditioning systems used to cool the plane during the delay were located underneath the center fuel tank [2]. At the time, the center fuel tank of TWA 800 was nearly empty, containing about 0.4% of fuel by volume [3]. With no insulation, the fuel tank likely absorbed heat from the AC systems, raising the partial pressure of the fuel, and causing the fuel tank to rupture and leak a higher density of fuel vapor [2]. The saturation necessary to reach the lower flammability limit required evaporation 1.4% of the fuel [3].

For combustion to occur, three requirements need to be met: fuel, oxygen, and a spark (or heat source). Measures have been made in tanks to reduce the chance of a spark, but also current systems blow out the fuel-air mixture to ensure it stays below the flammability limit. Inerting systems inject an inert gas, like nitrogen, into the fuel tank to reduce the fuel vapor concentration to below the lower flammability limit.

In this thesis, the use of objects floating on the surface of fuel inside a fuel tank to reduce the fuel vapor concentration is explored. The hypothesis is that covering the surface of the fuel with a

floating barrier will reduce the amount of fuel evaporated, thereby keeping the vapor concentration below the lower flammability limit.

Chapter 2. LITERATURE BACKGROUND

Yuriy Lyulin and Oleg Kabov conducted experiments to study the effect of gas velocity, temperature, and liquid depth has on the evaporation flow rate of a horizontal liquid layer under shear-stress [4]. In the test cell, nitrogen gas was injected over the liquid (HFE-7100) at a constant flow rate and constant temperature while the piston and liquid injection maintain a constant liquid level. The evaporation mass flow rate was measured by a flow meter as the gas-vapor mixture flows through a bypass line at the outlet.

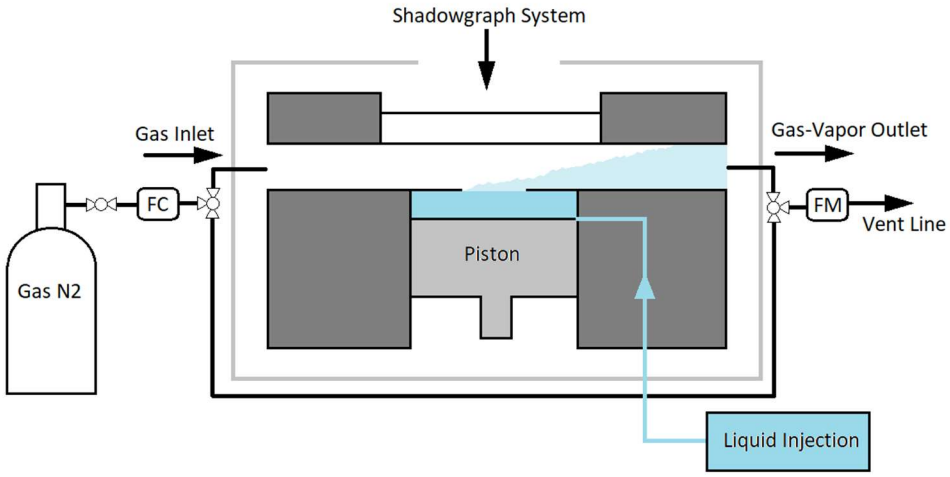

Figure 2.1. Experimental setup for a horizontal liquid layer under shear-stress. Image adapted from source [4].

The test cell consists of a diverging zone and converging zone to create a uniform gas flow in the middle test section. In the center of the middle section is a stainless-steel flat plate with a 10 mm by 10 mm opening where liquid is exposed to the gas flow.

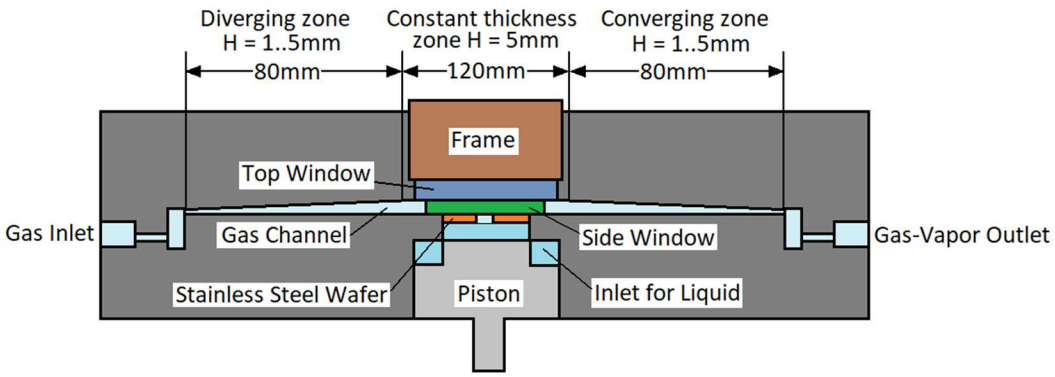

Figure 2.2. Cross section and dimensions of the test cell. Image adapted from source [4].

The evaporation mass flow rate was measured in two ways: by the average liquid flow that was injected to keep the liquid level constant during the test and by a comparison of the mass flow rate at the inlet (dry gas) and outlet (gas-vapor mixture). The results for the experiment at a constant temperature of 20 °C and liquid depth of 3 mm are shown in Figure 2.3.

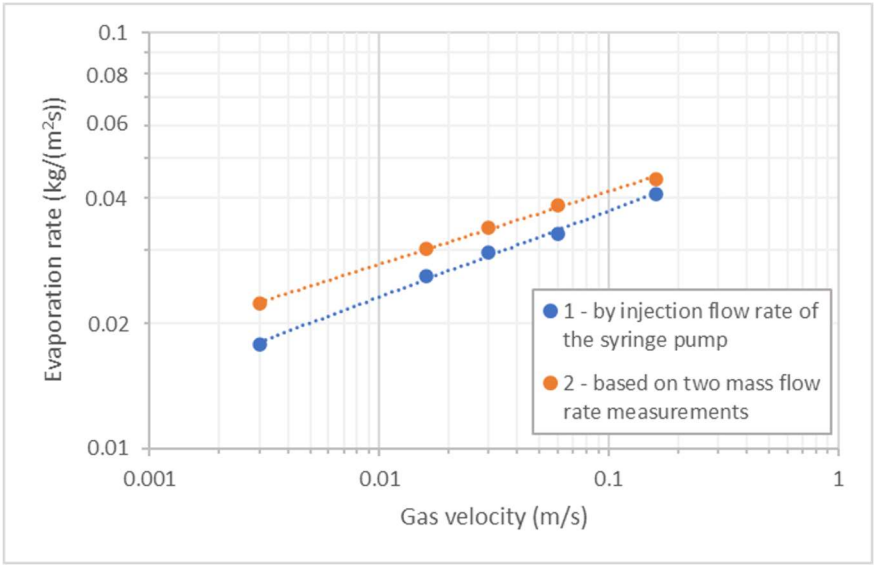

Figure 2.3. Evaporation flow rate comparing two methods of measurement. Plot adapted from source [4].

The average gas velocities ranged from 0.003 m/s to 0.16 m/s, Reynolds number 1.20 – 60 [4]. As shown, the measurements based on the mass flow rate at the inlet and outlet was consistently higher than the measurements of the injected liquid. Lyulin and Kabov concluded this was likely due to an error in the conversion of the volumetric flow rate of the liquid to the mass flow rate [4]. The evaporation flow rate measured by the inlet and outlet flow rate for varying temperatures for liquid depth of 3 mm is shown in Figure 2.4. It is apparent, the average evaporation flow rate increases as the gas velocity or temperature increase. The evaporation flow rate at various gas velocity and temperatures is given by

$$Q_l = 1.5 \times 10^{-4} \cdot T^{1.82} \cdot U_g^{0.147} \tag{2.1}$$

$$Q_l = 1.5 \times 10^{-4} \cdot T^{1.89} \cdot U_g^{0.164} \tag{2.2}$$

$$Q_l = 1.5 \times 10^{-4} \cdot T^{1.86} \cdot U_g^{0.173} \tag{2.3}$$

$$Q_l = 1.5 \times 10^{-4} \cdot T^{1.75} \cdot U_g^{0.161}\,, \tag{2.4}$$

where Q_l is the evaporation flow rate, U_g is the average gas velocity, and T is the temperature [4]. These equations correspond to the liquid depth 1.5 mm, 3 mm, 5 mm, and 8 mm respectively.

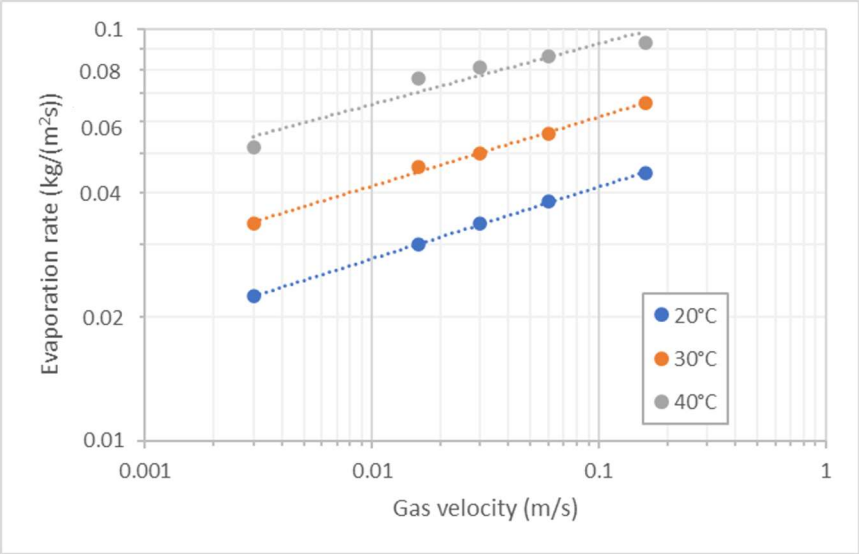

Figure 2.4. Evaporation flow rate varying gas velocity and temperature. Plot adapted from source [4].

There is also a correlation between the liquid depth at different gas velocities and temperatures. As shown in Figure 2.5, there is a local maximum for the average evaporation flow rate at liquid depth 3 mm for temperatures 20 °C and 30 °C. At 40 °C the local maximum is at liquid depth 5 mm.

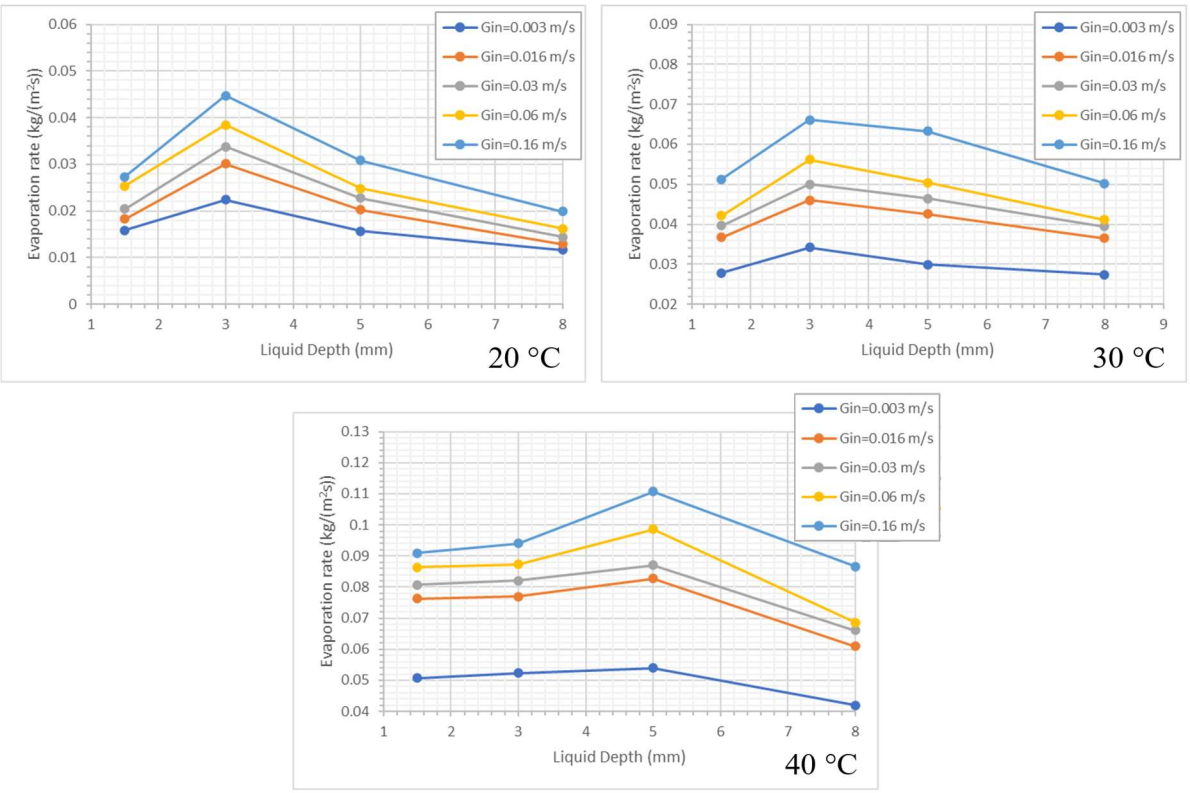

Figure 2.5. Evaporation flow rate for T = 20 °C, 30 °C, 40 °C. Plot adapted from source [4].

Since the evaporation flow rate depends on the gas velocity, temperature, and liquid depth, it follows that the structure of the convective flow in the fluid surface also varies. Varying the liquid depth also changes the temperature gradient and buoyance convection across the liquid layer, thus changing the force balance dictating the convective flow. Study of the shadowgraphs taken for varying liquid depths indicate that the liquid depth affects the formation and development of convective flow within the liquid layer (see Figure 2.6). Analysis of the video also confirms the gas-liquid interface moves in the counter-current direction to the gas flow. Lyulin and Kabov concluded that the evaporation flow rate is proportional to the shear stress of the liquid surface caused by the thermocapillary effect and the maximum evaporation rate happens when a stable and uniform convective flow within the liquid layer is in the direction opposite to the gas flow.

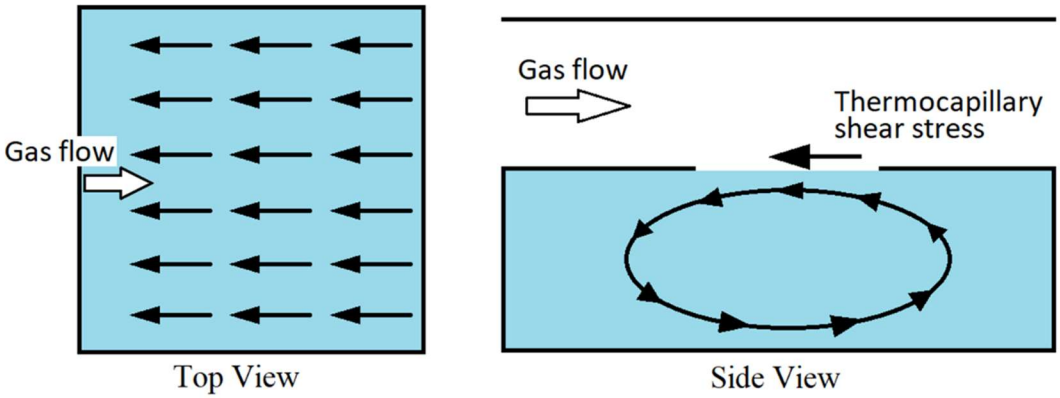

Figure 2.6. Convective flow within the liquid layer. Image adapted from source [4].

Currently, there is a lack of experimental data for evaporation between a gas and liquid inside a fuel tank with non-uniform flow and no known experiments that measure the evaporation of a liquid with floating objects or a barrier on the air-liquid interface.

Chapter 3. FUEL TANK GEOMETRY

The shell of the simulated fuel tank is a cube with a circular inlet and circular outlet of equal size. Each side of the tank (L) is 0.5 meters, and the diameter of the inlet and outlet (d_{inlet} and d_{outlet}) is 0.05 meters. Inside the tank, the simulated fluid is water at a depth of 0.25 meters. Water was chosen for feasibility of future physical experiments to compare to numerical simulations without testing volatile fluids such as Jet A or kerosene.

Two tank configurations were evaluated. Configuration 1, modeled after the setup used in the Lyulin Kabov experiment, the circular inlet and outlet are directly opposite each other with the center points at 0.05 meters above the fluid surface as shown in Figure 3.1. Configuration 2 is modeled after the Boeing 747 fuel tank [2] with both the inlet and outlet located on the top of the fuel tank. The center points of the inlet and outlet are along the axis of symmetry, separated by 0.166 meters as shown in Figure 3.2.

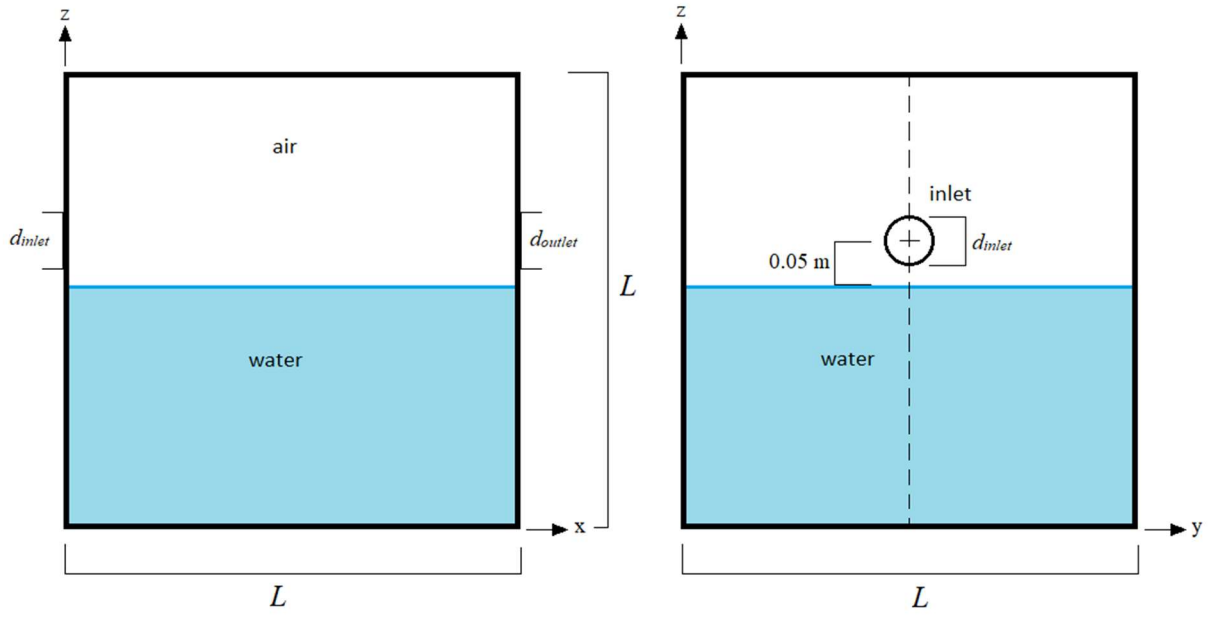

Figure 3.1. Configuration 1 of the fuel tank, x-plane and y-plane side views.

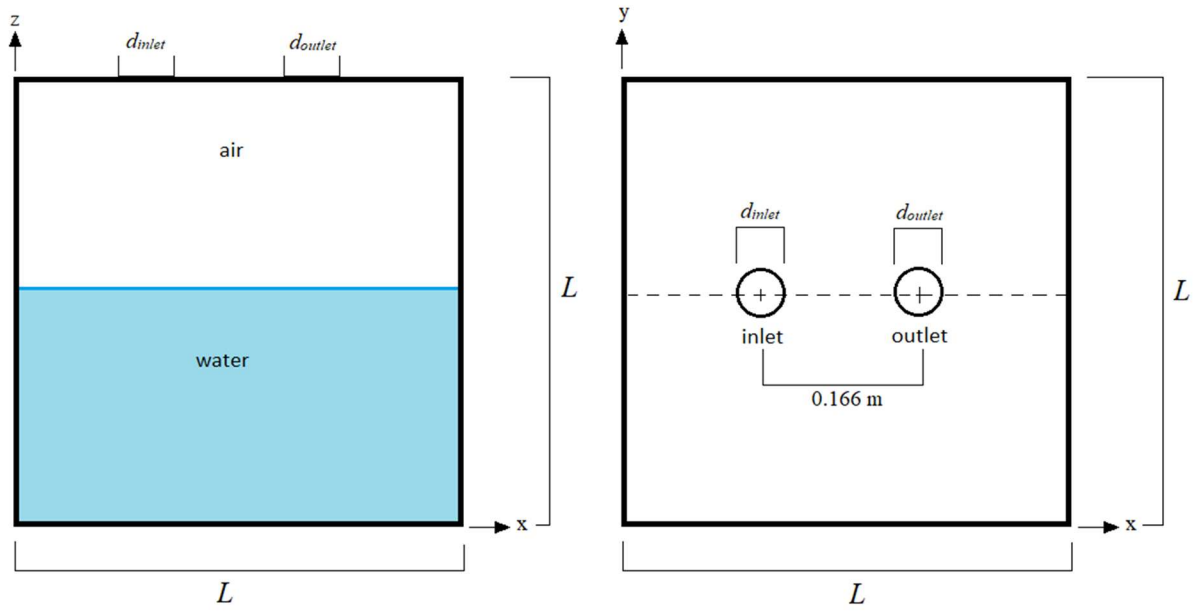

Figure 3.2. Configuration 2 of the fuel tank, side and top views.

3.1 Geometry of the Floating Objects

For simplicity, two shapes of floating objects have been explored: rectangular blocks and inverted cones. The rectangular blocks have a width (w_{rect}) of 0.08 meters and height (h_{rect}) of 0.1 meters. The inverted cones are a right-angle cone with a flat circular base of diameter d_{cone} and height h_{cone}.

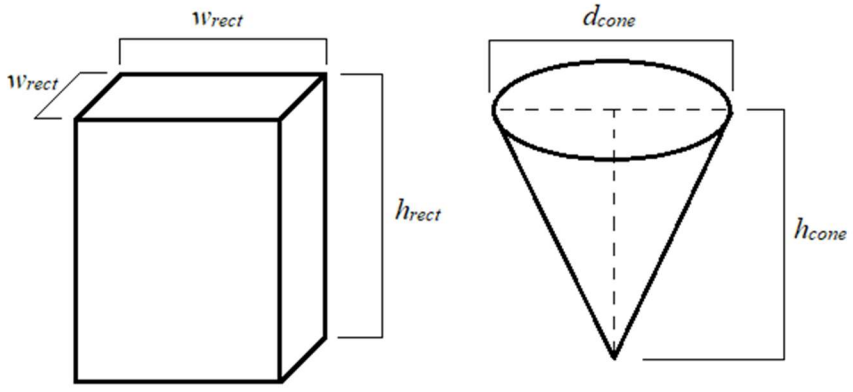

Figure 3.3. Geometry of the rectangular blocks and inverted cones.

The inverted cones are modeled in three sizes each to scale of one another: large, medium, small. Where the diameter of the Large inverted cone was designed to be equal in surface area to the top of the rectangular block. Dimensions for the inverted cones are listed in Table 3.1.

Table 3.1. Dimensions of Inverted Cones

Size	Diameter (m)	Height (m)
Large (100%)	0.0902	0.1
Medium (75%)	0.06765	0.075
Small (50%)	0.0451	0.05

Each cone is weighted at the apex to stay inverted while the water is sloshing around in the fuel tank. Using the buoyancy force F_{buoy} in equilibrium with the weight of the cone, the mass can be calculated by

$$W_{cone} = F_{buoy} = \rho V_{dis} g \ , \tag{3.1}$$

and

$$m_{cone} = \rho \left(\frac{1}{3} \pi r_{dis}^2 h_{dis} \right) , \tag{3.2}$$

where ρ is the density of water, V_{dis} is the displaced volume of water, g is gravity, h_{dis} is the height of the cone submerged, and r_{dis} is the cone radius at the water surface [5].

Using the buoyancy force equation (3.1), the mass of the rectangular floating object is given by

$$m_{rect} = \rho (h_{dis} * {w_{dis}}^2) \ , \tag{3.3}$$

where h_{dis} is the height of the rectangle submerged and w_{dis} is 0.8 meters.

The top surface of the rectangular blocks and Large inverted cones were designed to be at the same height from the fluid surface. Placement of the Medium and Small inverted cones followed

the buoyancy calculating according to the cone size. The distance along the z-axis where the top of the blocks is listed in Table 3.2.

Table 3.2. Location of the top of the floating objects

Shape	**z (meter)**
Rectangular Block	0.275
Large Inverted Cone	0.275
Medium Inverted Cone	0.26875
Small Inverted Cone	0.2525

3.2 Arrangement of the Floating Objects

Simulations with floating objects inside all used Configuration 2 of the fuel tank, where the inlet and outlet are on the top of the tank (refer to Figure 3.2). Inside, the floating objects are arranged in evenly spaced arrays across the fluid surface shown in Figure 3.4. The base arrangement for the rectangular blocks and inverted cones is a 4x4 grid, with the center points in identical locations (see Figure 3.4a and b). The first array uses the same base 4x4 grid of Large inverted cones with Medium inverted cones equally spaced between (see Figure 3.4c). The second array adds Small inverted cones to the first array (see Figure 3.4d).

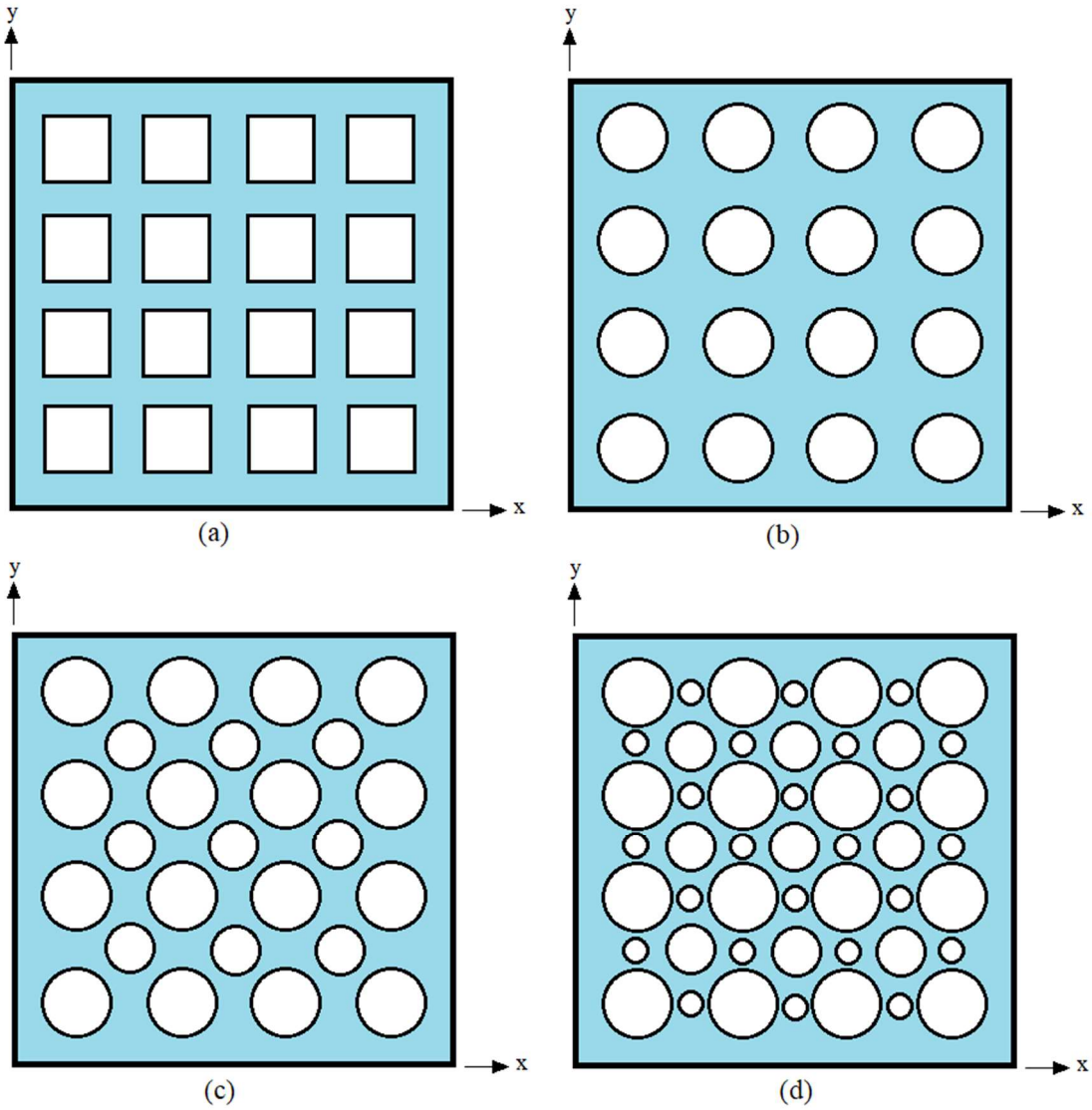

Figure 3.4. Arrangement of floating objects: *(a)* 16 Rectangular blocks; *(b)* 16 Large inverted cones; *(c)* 16 Large and 9 Medium inverted cones; *(d)* 16 Large, 9 Medium, and 24 Small inverted cones.

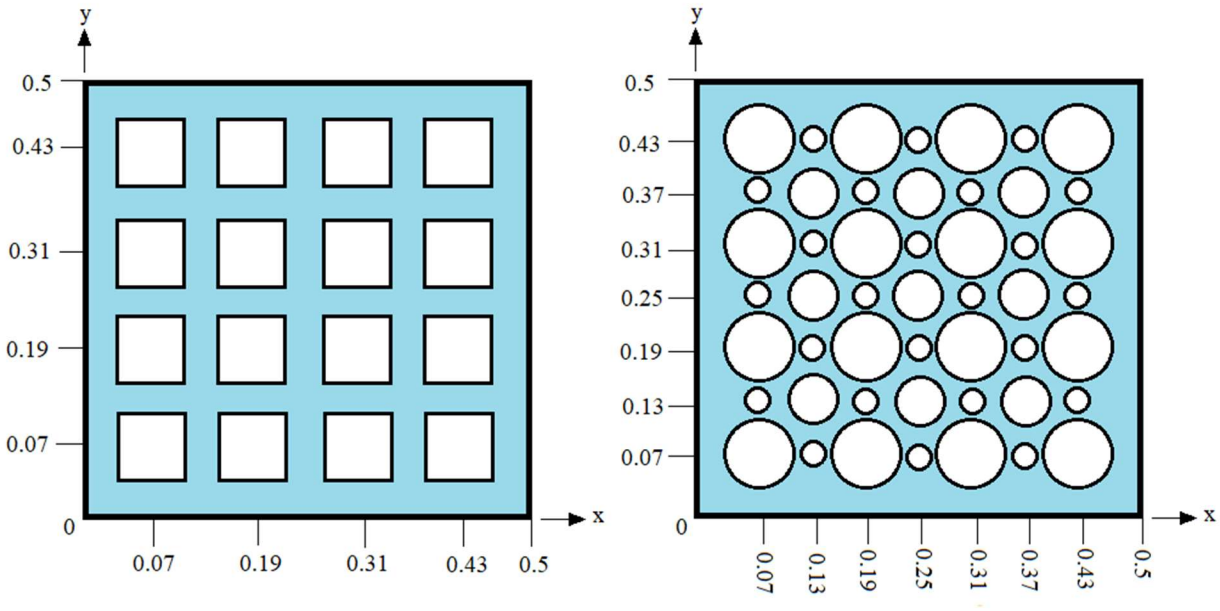

Figure 3.5. Location of floating objects inside the fuel tank (in meters).

Chapter 4. CFD SIMULATION

Computational Fluid Dynamics (CFD) is the use of computers to make a numerical simulation of fluid flows. This is useful for initial validation prior to performing experiments. All CFD flow problems can be modeled using the Navier-Stokes equations to resolve the flow field. Solving the flow field exactly as given by the Navier-Stokes equations is known as direct numerical simulation (DNS). This resolves all turbulent length scales at a computational cost proportional to the Reynolds number, Re^3, for homogenous turbulence [6].

A DNS for multiphase turbulent flows in a fuel tank requires a large amount of computing power that is not feasible at the university level. Various methods exist to model the turbulence using various assumptions to reduce the computing time. One commonly used model is the Reynolds Averaged Simulation (RAS), also known as Reynolds-averaged Navier-Stokes (RANS).

All simulations in this thesis were run on two high-performance computing (HPC) resources available to students at the University of Washington. Cerberus-UWAA is a 19-node cluster funded by the Student Technology Fund (STF) and owned by the Aeronautics and Astronautics department. Cerberus-UWAA was decommissioned in 2018. Hayak is a shared supercomputing cluster partially funded by the STF and operated by the University of Washington.

4.1 GOVERNING EQUATIONS

The Navier-Stokes equations used to describe the motion of Newtonian fluids are given by

$$\frac{\partial \rho}{\partial t} + \nabla \cdot (\rho \boldsymbol{u}) = 0 \tag{4.1}$$

$$\nabla \cdot \boldsymbol{u} = 0 \tag{4.2}$$

$$\rho \frac{\partial \boldsymbol{u}}{\partial t} + \rho(\boldsymbol{u} \cdot \nabla)\boldsymbol{u} = -\nabla p + \nabla \cdot \bar{\tau} + \rho \boldsymbol{f}_e \tag{4.3}$$

$$\mathrm{Re} = \frac{\rho U L}{\mu}, \tag{4.4}$$

where ρ is the density, $\boldsymbol{u}$ is the velocity vector, p is the pressure, τ is the viscous shear stress tensor, and $\boldsymbol{f}_e$ is the external force per unit mass [5].

4.2 OpenFOAM

OpenFOAM is an open-source CFD software, created by OpenCFD Ltd., with built-in solvers to model a wide range of fluid dynamic problems. To model the fuel tank with floating objects, the solver interDyMFoam was chosen. This solver is useful for "2 incompressible, isothermal immiscible fluids using a VOF (volume of fluid) phase-fraction based interface capturing approach, with optional mesh motion and mesh topology changes including adaptive re-meshing" [7]. Also, it calculates 6-degree of freedom body forces acting on objects to determine the mesh motion. OpenFOAM version 2.4.0 was used to calculate all simulations in this thesis.

4.2.1 *Reynolds Averaged Simulation*

The Reynolds Average Simulation (RAS) equations are defined in OpenFOAM as

$$\boldsymbol{u} = \overline{\boldsymbol{u}} + \boldsymbol{u}' \tag{4.5}$$

$$\overline{\boldsymbol{u}'} = 0 \tag{4.6}$$

$$\frac{\partial}{\partial t}(\rho) + \nabla \cdot (\rho \overline{\boldsymbol{u}}) = 0 \tag{4.7}$$

$$\frac{\partial}{\partial t}(\rho \overline{\boldsymbol{u}}) + \nabla \cdot (\rho \overline{\boldsymbol{u}} \otimes \overline{\boldsymbol{u}}) = \boldsymbol{g} + \nabla \cdot \overline{(\tau)} - \nabla \cdot (\rho \boldsymbol{R}), \tag{4.8}$$

where t is the time, τ is the averaged stress tensor, p is the pressure, and ρ is the density [8]. The averaged stress tensor τ is given by

$$\bar{\tau} = -\left(p + \frac{2}{3}\mu \nabla \cdot \overline{\boldsymbol{u}}\right)\boldsymbol{I} + \mu(\nabla \overline{\boldsymbol{u}} + (\nabla \overline{\boldsymbol{u}})^T). \tag{4.9}$$

Then using the identity

$$\nabla \cdot \overline{\boldsymbol{u}} = \mathrm{tr}(\nabla \overline{\boldsymbol{u}}) = \mathrm{tr}((\nabla \overline{\boldsymbol{u}})^T) \,, \tag{4.10}$$

the averaged stress tensor becomes

$$\bar{\tau} = -p\boldsymbol{I} + \mu \left[\nabla \overline{\boldsymbol{u}} + (\nabla \overline{\boldsymbol{u}})^T - \frac{2}{3}\mathrm{tr}((\nabla \overline{\boldsymbol{u}})^T)\boldsymbol{I}\right] \tag{4.11}$$

or

$$\bar{\tau} = -p\boldsymbol{I} + \mu[\nabla \overline{\boldsymbol{u}} + \mathrm{dev2}((\nabla \overline{\boldsymbol{u}})^T)] \,, \tag{4.12}$$

where dev2 is defined as

$$\mathrm{dev2}(\phi) = \phi - \frac{2}{3}\mathrm{tr}(\phi)\boldsymbol{I} \,. \tag{4.13}$$

The Reynold's stress tensor $\boldsymbol{R}$ is defined as

$$\boldsymbol{R} = \overline{\boldsymbol{u}' \otimes \boldsymbol{u}'} \,. \tag{4.14}$$

Divided into isotropic and deviatoric anisotropic contributions, the Reynolds stress tensor becomes

$$\boldsymbol{R} = \frac{2}{3}k\boldsymbol{I} + \overline{\boldsymbol{u}' \otimes \boldsymbol{u}'} - \frac{2}{3}k\boldsymbol{I} \,, \tag{4.15}$$

where the turbulent kinetic energy k is

$$k = \frac{1}{2}\overline{\boldsymbol{u}' \cdot \boldsymbol{u}'} = \frac{1}{2}\mathrm{tr}(\boldsymbol{R}) \,. \tag{4.16}$$

Applied back to Equation (4.8), the RAS momentum equation becomes

$$\frac{\partial}{\partial t}(\rho \overline{\boldsymbol{u}}) + \nabla \cdot (\rho \overline{\boldsymbol{u}} \otimes \overline{\boldsymbol{u}}) = \boldsymbol{g} - \nabla \bar{p}' + \nabla \cdot (\mu \nabla \overline{\boldsymbol{u}})$$

$$+\nabla \cdot [\mu \mathrm{dev2}((\nabla \overline{\boldsymbol{u}})^T)] - \nabla \cdot (\rho \boldsymbol{R}_{dev}) \,. \tag{4.17}$$

$$\boldsymbol{R}_{dev} = \overline{\boldsymbol{u}' \otimes \boldsymbol{u}'} - \frac{2}{3}k\boldsymbol{I} \tag{4.18}$$

$$p' = \bar{p} + \frac{2}{3}\rho k \,. \tag{4.19}$$

4.2.2 *k-omega SST model*

The k-ω SST model is a variant of the standard two equation k-ω turbulence model that is combined with the shear stress transport (SST). It can capture flow separation and stabilize flow visualization of enclosed environments. The turbulence specific dissipation rate equation and turbulence kinetic energy for the k-ω SST model are given by

$$\frac{D}{Dt}(\rho\omega) = \nabla\cdot(\rho D_{\omega}\nabla\omega) + \frac{\rho\gamma G}{\upsilon} - \frac{2}{3}\rho\gamma\omega(\nabla\cdot\boldsymbol{u}) - \rho\beta\omega^2 - \rho(F_1 - 1)CD_{k\omega} + S_{\omega} \tag{4.20}$$

$$\frac{D}{Dt}(\rho k) = \nabla\cdot(\rho D_k\nabla k) + \rho G - \frac{2}{3}\rho k(\nabla\cdot\boldsymbol{u}) - \rho\beta^{*}\omega k + S_k\,, \tag{4.21}$$

where k is the turbulence kinetic energy and ω is the turbulence specific dissipation rate [9]. The turbulence viscosity is given by

$$\upsilon_t = a_1\frac{k}{max(a_1\omega, b_1F_{23}S)}\,, \tag{4.22}$$

where the default constants are listed in

Table 4.3. OpenFOAM coefficients for k-ω SST model [9]

Coefficient	Value
a_{k1}	0.85
a_{k2}	1.0
$a_{\omega1}$	0.5
$a_{\omega2}$	0.856
β_1	0.075
β_2	0.0828
γ_1	5/9
γ_2	0.44
β^*	0.09
a_1	0.31
b_1	1.0
c_1	10.0

4.2.3 *Volume of Fluid*

Volume of fluid (VOF) is used to capture the interface between air and liquid in the tank by tracking the volume fraction of fluid (α) in each cell. In this case, air is the primary phase and liquid is the secondary phase

$$\alpha = \begin{cases} 0 & \text{air} \\ 0 < \alpha < 1 & \text{interface} \\ 1 & \text{liquid} \end{cases},$$

where the interface are the cells that capture the liquid surface. The value of α at the interface can be described by

$$\frac{\partial \alpha}{\partial t} + \boldsymbol{u} \cdot \nabla \alpha = 0 \tag{4.23}$$

OpenFOAM uses a modified version that includes a compression term to sharpen the interface

$$\frac{\partial \alpha}{\partial t} + \boldsymbol{u} \cdot \nabla \alpha + \nabla \cdot [\boldsymbol{u}_r \alpha (1 - \alpha)] = 0 \tag{4.24}$$

where $\boldsymbol{u}_r$ is the relative velocity between the two phases [7].

4.2.4 *Boundary Conditions*

Boundary conditions are used in CFD to define how the fluid interacts with specific patches of the geometry. In OpenFOAM, patches are organized into base types which each have a certain set of boundary conditions that can be applied. The base type “patch” is a generic type that contains all boundary condition options, this was used for the inlet and outlet. For the walls of the fuel tank and surfaces of the floating objects, the base type “wall” was used. Defining a wall patch is required for turbulence modeling in OpenFOAM.

The inlet of the fuel tank was modeled to blow air in at a constant and uniform value as an inlet fan would. The “fixedValue” boundary condition in OpenFOAM was used to define a constant and uniform velocity vector at the inlet. The derived “fixedFluxPressure” boundary

condition was applied or the pressure. This allows for the effects of gravity and surface tension in the solution and adjusts the pressure gradient accordingly, so the flux matches the velocity boundary condition.

The outlet of the fuel tank was modeled to equalize the pressure inside the fuel tank as air is blown in from the inlet. To achieve this the combination of boundary conditions used were: “totalPressure”, “pressureInletOutletVelocity”, and “inletOutlet”. The “totalPressure” boundary condition is a fixed value calculated from the specific total pressure and the local velocity. The velocity of the outlet was given the boundary condition “pressureInletOutletVelocity”. This applies a fixed value in the tangential direction and a zero gradient on all other components. The “inletOutlet” boundary condition applies the zero gradient condition when flow is outwards and a fixed value when flow is inwards.

A no-slip boundary condition was used for the physical walls of the fuel tank model and the surfaces of the floating objects. The “noSlip” condition is a Dirichlet condition that defines the velocity to be zero at the solid surface. The boundary condition “zeroGradient” was used for the phase and “fixedFluxPressure” for the pressure and temperature at the walls. The “zeroGradient” condition defines the normal gradient of a field value to always be zero.

4.3 SALOME

Salome is an open-source CAD software created in September 2000 by multiple partners under the leadership of OPEN CASCADE, an EADS Matra Datavision company at the time. The goal was to “provide a working environment for the simulation and analysis of phenomena to be taken into account for waste storage and disposal studies” [10]. Originally made for Linux systems, it has since expanded to Windows operating systems. Salome version 7.5.1 for Windows was used to create meshes for all simulation in this thesis.

4.3.1 *Geometry*

The geometry of the fuel tank and floating objects were created using the geometry module in Salome. The floating objects were placed in the fuel tank at the height corresponding to the depth of water as calculated using the buoyancy force, Equation (3.2). An example of the geometry for the fuel tank with inverted cones is shown in Figure 4.1.

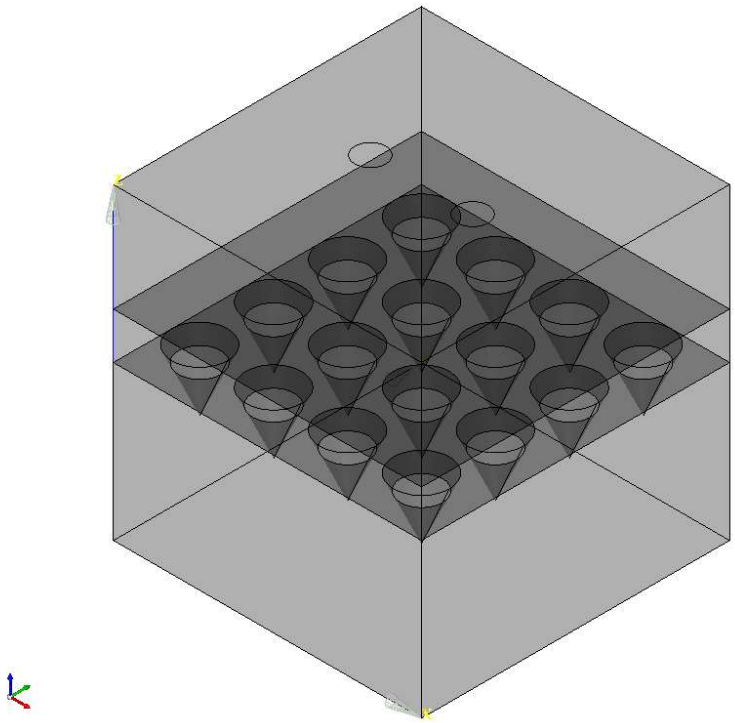

Figure 4.1. Geometry of a fuel tank with floating objects inside.

4.3.2 *Mesh*

For all simulations, the geometry has been split into tetrahedral elements using Netgen 1D-2D-3D in the SALOME mesh module. Tetrahedral elements were chosen to avoid singularities that occur when meshing pointed objects like a cone. A sample mesh of the fuel tank with inverted cones is shown in Figure 4.2.

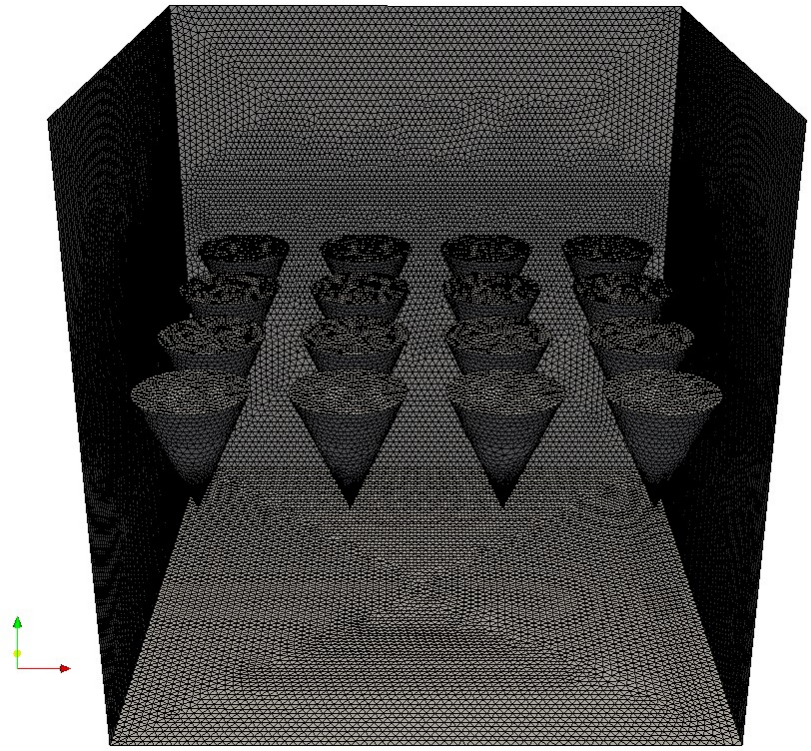

Figure 4.2. Mesh of a fuel tank with floating objects inside for inlet speed Re = 1700.

As shown, the mesh is denser around the floating objects. This was intentionally done to capture the turbulence of the fluid surface as air passes over it. The maximum and minimum cell sizes of the mesh were chosen using the non-dimensional distance y^+ as a guide. For the k-ω SST turbulence model, a y^+ value close to 1 is ideal for mesh cells near the wall. The wall spacing can be determined by

$$\mathrm{Re}_x = \frac{\rho U_\infty L}{\mu} \tag{4.25}$$

$$C_f = \frac{0.026}{\mathrm{Re}_x{}^{1/7}} \tag{4.26}$$

$$\tau_{wall} = \frac{C_f \rho U_\infty{}^2}{2} \tag{4.27}$$

$$U_{fric} = \sqrt{\frac{\tau_{wall}}{\rho}} \tag{4.28}$$

$$\Delta s = \frac{y^+ \mu}{U_{fric}}, \tag{4.29}$$

where U_∞ is the freestream velocity, ρ is density, μ is the dynamic viscosity, L is the reference length, and Δs is the wall spacing [11].

4.4 PARAVIEW

ParaView is an open-source post-processing program that is included in OpenFOAM 2.4.0. In 2000, ParaView started as a collaborative effort between Kitware Inc. and Los Alamos National Laboratory. With initial funding from the US Department of Energy ASCI Views program, the first public release was announced in October 2002. ParaView version 4.2.0 64-bit for Windows was used to post-process all calculations. This version was created by Kitware, Sandia National Laboratories, Los Alamos National Laboratory, Advanced Simulation and Computing, and Army Research Laboratory [12].

The backbone of ParaView is the Visualization Toolkit (VTK) used as the data processing and rending engine. The raw data results from calculating a simulation in OpenFOAM is not directly compatible and the foamToVTK tool must be used to process the results in ParaView.

Chapter 5. CALCULATING MASS FLOW RATE

Although the OpenFOAM solver tracks mass through VOF and is capable of calculating evaporation, the computational cost was too high to run on the available HPC at the time. Instead, the mass flow rate is extracted using the turbulent kinetic energy. The smallest eddies along the water surface are responsible for mixing and entrainment. The characteristic time of the small eddy is given by

$$\tau_\lambda = \frac{\lambda}{v_\lambda}, \tag{5.1}$$

where v_λ is the eddy rotational velocity and λ is the diameter. The diffusivity coefficient of the inlet jet is

$$\mathcal{D}_T = \frac{\lambda^2}{\tau_\lambda} = \lambda v_\lambda , \tag{5.2}$$

where the rotational velocity is the velocity fluctuation *u'*

$$v_\lambda = \sqrt{u'^2} = u' . \tag{5.3}$$

The equivalent entrainment velocity for the diffusive flux is defined as

$$v_e = \sqrt{\frac{\mathcal{D}_T}{\tau_\lambda}} . \tag{5.4}$$

Then by applying (5.2) and the definition of *k* (4.16), the equivalent entrainment velocity becomes

$$v_e = v_\lambda = \sqrt{2k} . \tag{5.5}$$

The volume flow rate and mass flow rate of water are given by

$$\dot{V}_{water} = v_e A_s \tag{5.6}$$

$$\dot{m}_{water} = \rho_{water} \dot{V}_{water} , \tag{5.7}$$

where A_s is the exposed surface area and ρ_{water} is the density of water vapor, 0.804 kg/m^3 at standard temperature and pressure (see Appendix A). The volume concentration of water vapor is given by

$$C_{water} = \frac{\dot{V}_{water}}{\dot{V}_{jet}+\dot{V}_{water}}, \tag{5.8}$$

where V_{jet} is the volume flow rate. It is given by

$$\dot{V}_{jet} = u_{inlet}\pi {r_{inlet}}^2, \tag{5.9}$$

where u_{inlet} is the inlet velocity and r_{inlet} is the radius of the circular inlet, 0.025m. The vortex filling time τ is given by

$$\tau = \frac{Vol^{2/3}}{\left(\frac{T}{\rho}\right)^{1/2}}, \tag{5.10}$$

$$T = \rho u_{inlet}^2 A_{inlet}, \tag{5.11}$$

where Vol is the volume of the fuel tank filled with air, T is the thrust of the inlet jet and A_{inlet} is the surface area of the inlet.

Chapter 6. RESULTS

The simulations held constant both the depth of fluid and the placement of floating objects, while varying the inlet speed. Inlet speeds ranging from 0.003 m/s to 0.1 m/s (approximately Re = 10 – 340) follow the gas speeds used in the horizontal liquid layer experiment [4] and higher inlet speeds increased by an increment of 0.2 m/s. All results are an average of 5 values: the data at the timestep of interest, two data sets taken at 0.1 s and 0.2 s before, and two data sets taken at 0.1 s and 0.2 s after. The maximum timestep each simulation was run for and the maximum timestep normalized by the vortex filling time at each inlet speed is listed in Table 6.4.

Table 6.4. Timestep for each inlet speed

Inlet speed (m/s)	**Re**	**t (s)**	**t/τ**
0.003	10	334	0.281922
0.01	30	100	0.281360
0.05	170	20	0.281360
0.1	340	10	0.281360
0.3	1000	10	0.844078
0.5	1700	10	1.406797
0.7	2400	10	1.969516

All volume flow rates measured were averaged across the horizontal plane at varying heights above the water surface. The distance above the water surface (dz) where the volume flow rates were measured are shown in Figure 6.1. Note that dz/L = 0.05 corresponds to the top of the largest floating objects used.

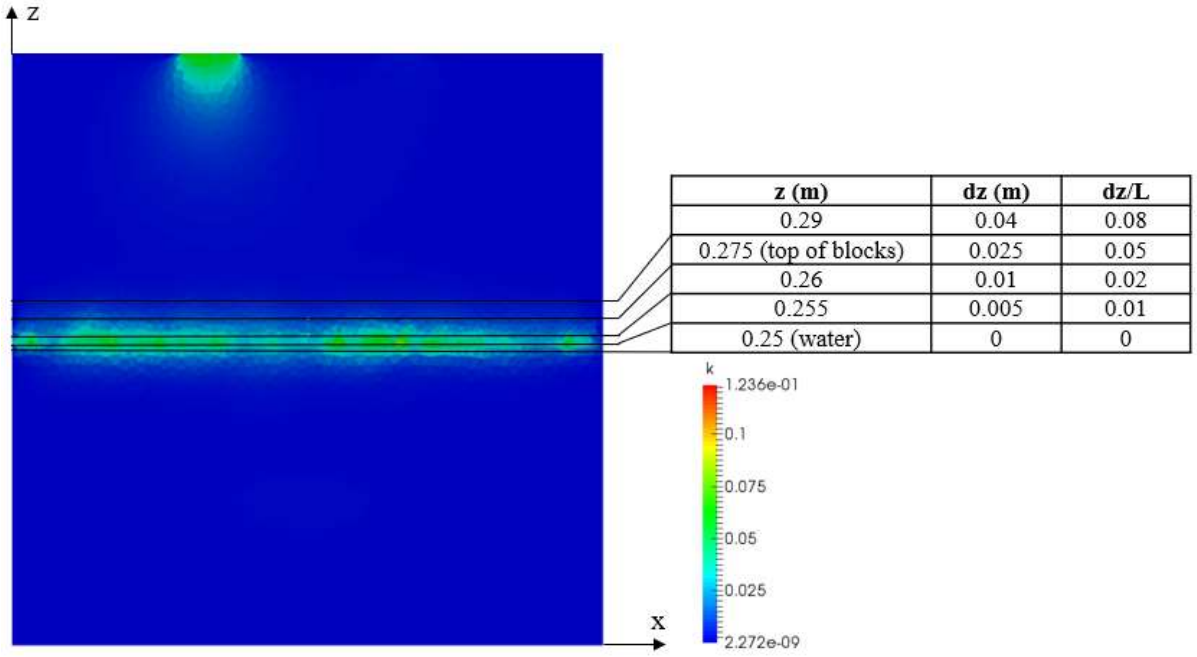

z (m)	dz (m)	dz/L
0.29	0.04	0.08
0.275 (top of blocks)	0.025	0.05
0.26	0.01	0.02
0.255	0.005	0.01
0.25 (water)	0	0

Figure 6.1. Distance above the water surface where the average volume flow rate is measured, shown in Configuration 2 fuel tank.

6.1 Steady State of Transient Simulations

The transient simulations exceeded the resource constraints of the high-performance computers. For inlet speeds Re = 10 – 340, the data cutoff was at the flow transit mixing time corresponding to twice the length of the fuel tank divided by the inlet nozzle speed. For inlet speeds Re = 1000 and greater, the data cutoff was at 10 seconds. The cutoff was due to resources needed to reach steady state with transient simulations exceeding the constraints of the high-performance computers.

The change in volume flow rate over time normalized by the vortex filling time for the Configuration 1 fuel tank without objects is shown in Figure 6.2 to Figure 6.4. For inlet speeds less than Re = 340, each simulation appears to reach steady state by the maximum timestep at which data was taken and the difference between any timestamp ranges 0.041 – 0.880%. For inlet

speeds greater than Re = 340, the volume flow rate appears to approach steady state at the final timestamp for all heights above the water surface. The difference at the final timestamps ranges 0.102 – 1.020%. At inlet speed Re = 340, the volume flow rate appears to reach steady state at dz/L = 0.05 above the water surface but is still changing close to the water by the 10 second cutoff. The difference between the 3rd and 4th timestamp is 1.018%, 0.606%, and 0.183% at dz/L = 0.01, 0.02, and 0.05 above the water surface respectively.

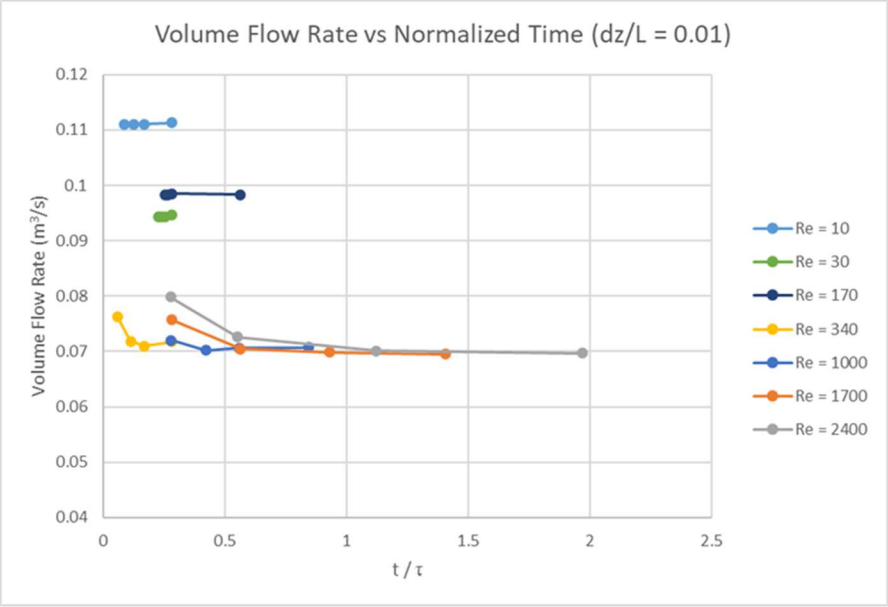

Figure 6.2. Volume flow rate over time for various inlet speeds in Configuration 1 fuel tank without objects, at dz/L = 0.01.

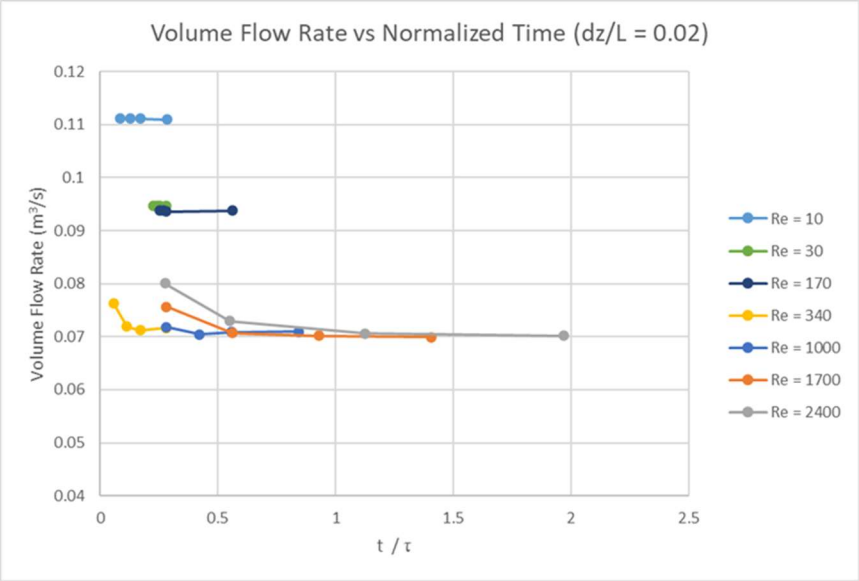

Figure 6.3. Volume flow rate over time for various inlet speeds in Configuration 1 fuel tank without objects, at dz/L = 0.02.

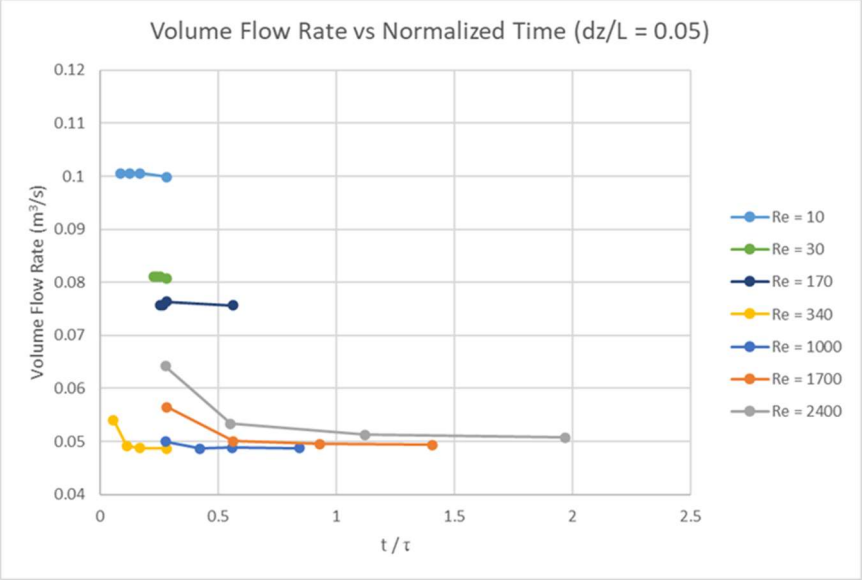

Figure 6.4. Volume flow rate over time for various inlet speeds in Configuration 1 fuel tank without objects, at dz/L = 0.05.

The volume flow rate over time for various inlet speeds taken at various heights above the water surface in the Configuration 2 fuel tank without objects are shown in Figure 6.5 to Figure 6.7. Note that the time is not normalized. For all heights above the water surface, the volume flow rate drops as time increases and appears to approach steady state. The difference in the final two timestamps at dz/L = 0.01 ranged 0.303 – 0.709%. And at dz/L = 0.02, the largest difference was 0.567%. The volume flow rate at dz/L = 0.05 (Figure 6.7) shows strong indications that it reaches steady state by the cut off with the difference ranging 0.016 – 0.430%. Although convergence was not achieved for inlet velocities Re ≥ 340 for either fuel tank configuration, as indicated by the volume flow rate at dz/L = 0.01 and 0.02, the change in volume flow rate was close to 1% and data obtained at 10 seconds will be treated as steady state for these inlet speeds.

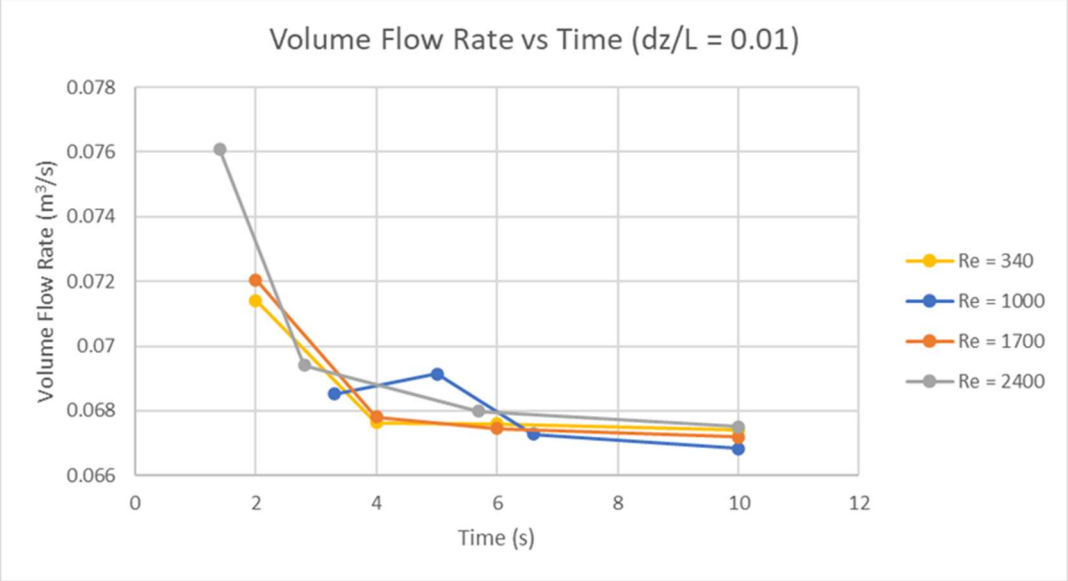

Figure 6.5. Volume flow rate over time for various inlet speeds in Configuration 2 fuel tank without objects, at dz/L = 0.01.

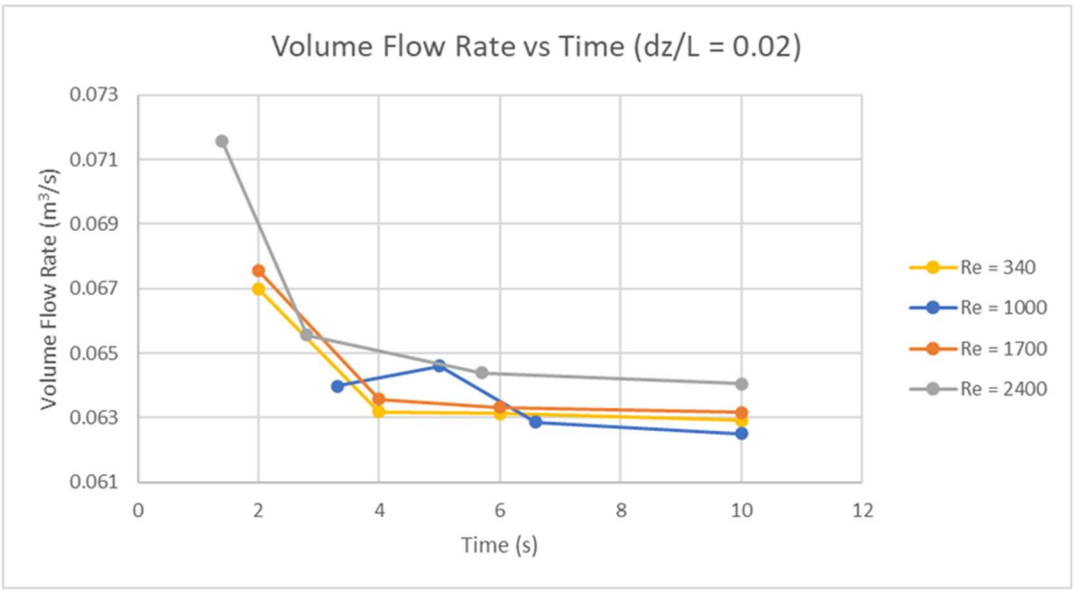

Figure 6.6. Volume flow rate over time for various inlet speeds in Configuration 2 fuel tank without objects, at dz/L = 0.02.

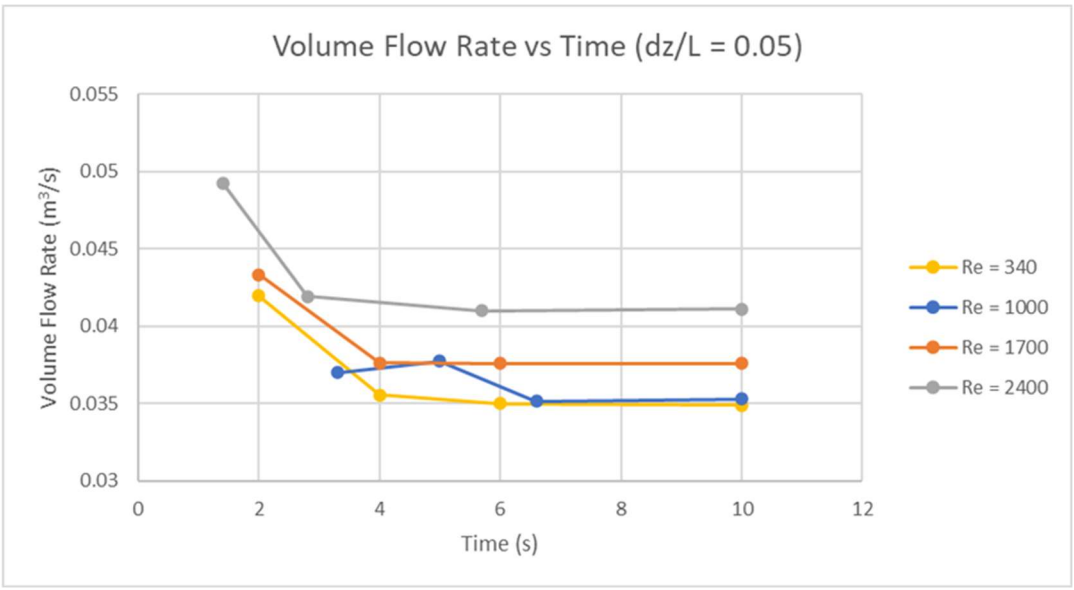

Figure 6.7. Volume flow rate over time for various inlet speeds in Configuration 2 fuel tank without objects, at dz/L = 0.05.

6.2 Average Turbulent Kinetic Energy

The turbulent kinetic energy *k* on a y-plane slice through the center of the fuel tank for Configuration 1 is shown in Figure 6.8 to Figure 6.14. The inlet and outlet are visible on the left and right edges. For all inlet speeds except Re = 170 and 340, the maximum average turbulent kinetic energy across the slice is at z = 0.26 m. This is 0.01 m above the water surface and 0.015 m below the edge of the inlet and outlet. The maximum average turbulent kinetic energy for inlet speed Re = 170 is at 0.25 m, on the water surface. And the maximum for inlet speed Re = 340 is at 0.255 m. For this reason, the volume flow rate for Configuration 1 was calculated at 0.255 m, 0.26 m, 0.275 m, and 0.29 m which corresponds to the two maximums observed, the lower edge of the inlet and outlet, and a point of interest respectively.

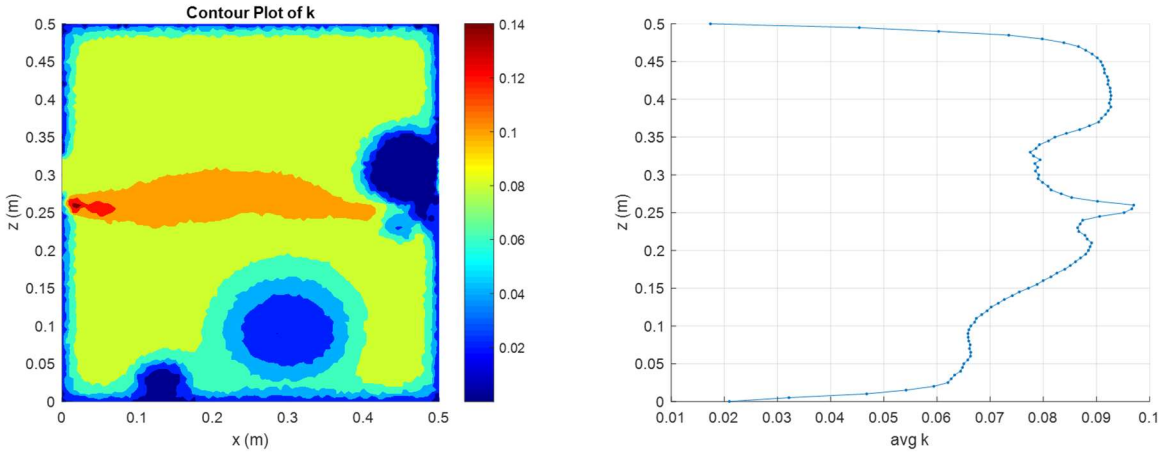

Figure 6.8. Contour *k* plot of a slice and average *k* along the z-axis for Configuration 1 fuel tank without objects, at Re = 10.

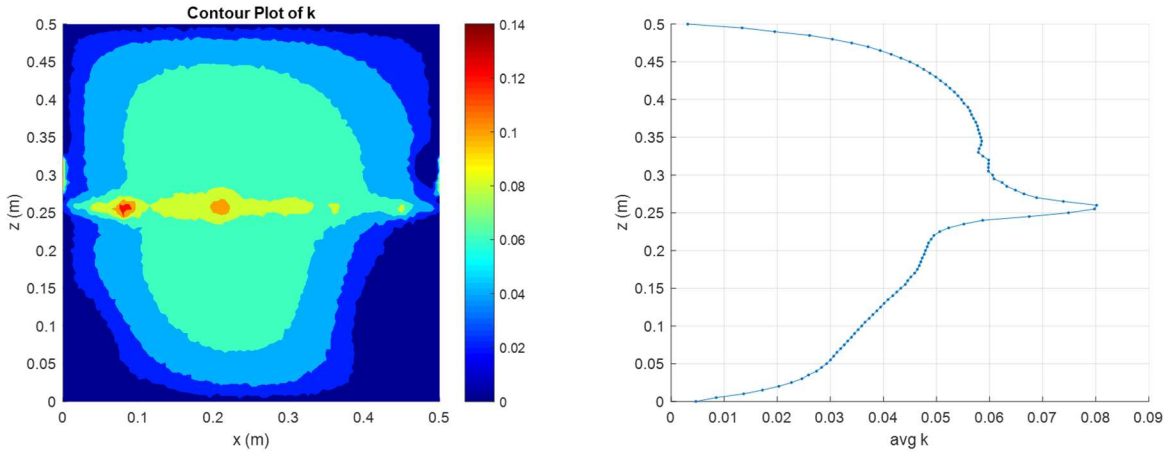

Figure 6.9. Contour *k* plot of a slice and average *k* along the z-axis for Configuration 1 fuel tank without objects, at Re = 30.

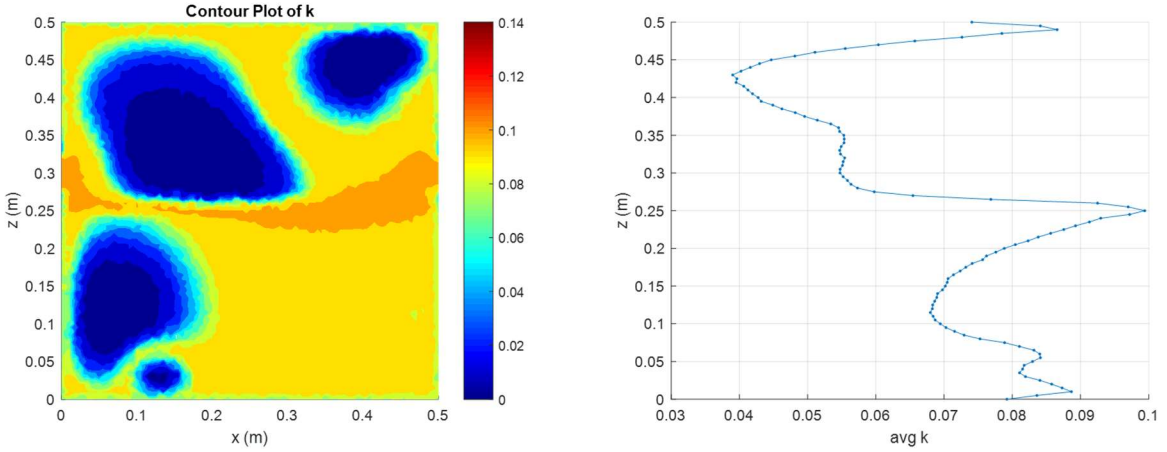

Figure 6.10. Contour *k* plot of a slice and average *k* along the z-axis for Configuration 1 fuel tank without objects, at Re = 170.

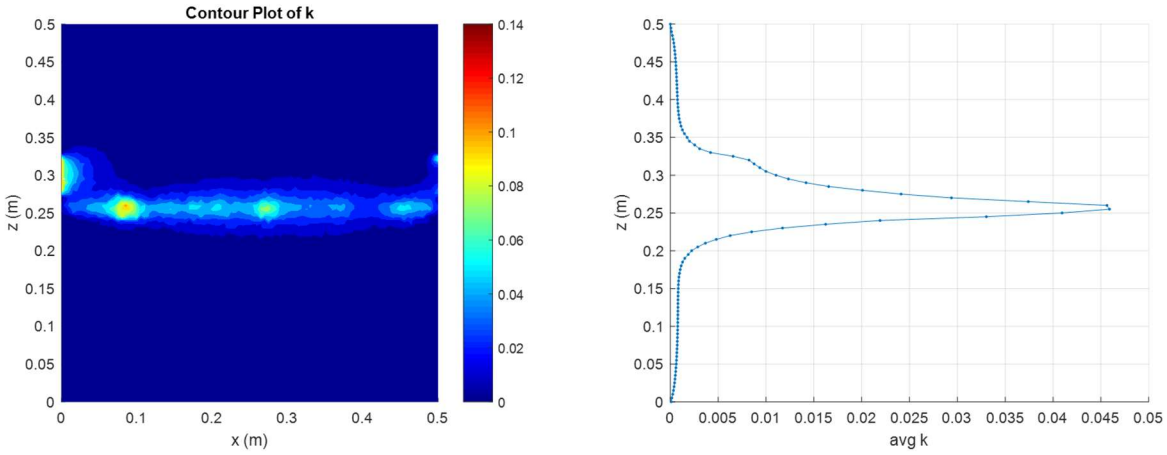

Figure 6.11. Contour *k* plot of a slice and average *k* along the z-axis for Configuration 1 fuel tank without objects, at Re = 340.

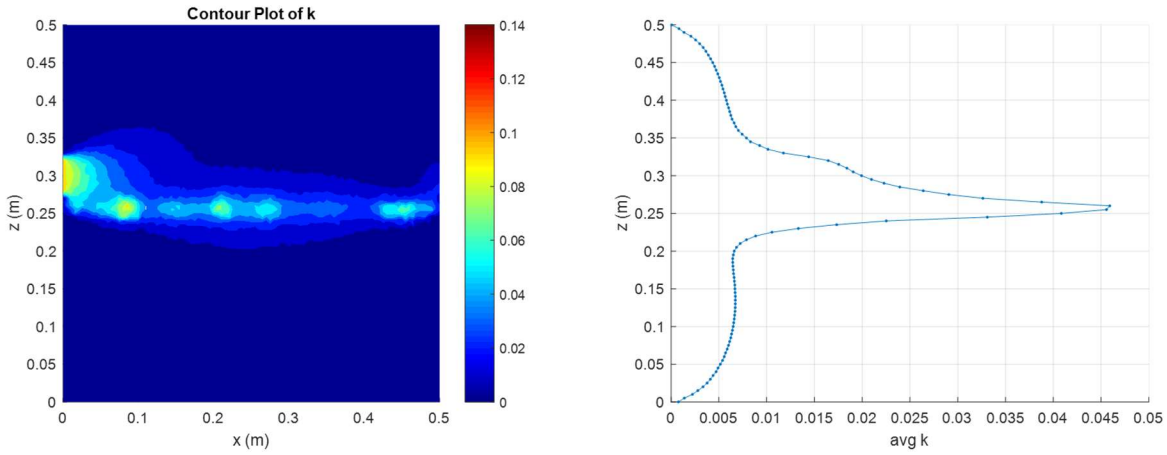

Figure 6.12. Contour *k* plot of a slice and average *k* along the z-axis for Configuration 1 fuel tank without objects, at Re = 1000.

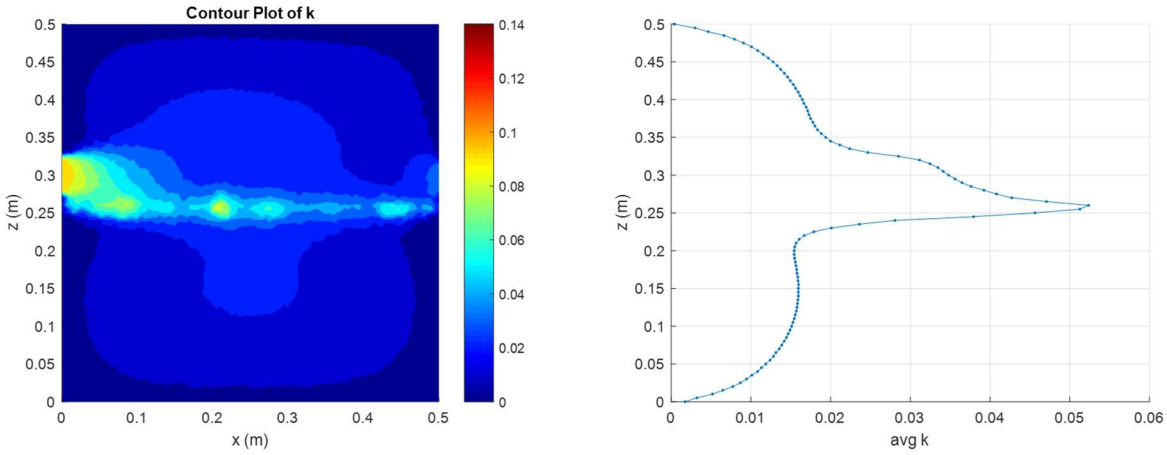

Figure 6.13. Contour *k* plot of a slice and average *k* along the z-axis for Configuration 1 fuel tank without objects, at Re = 1700.

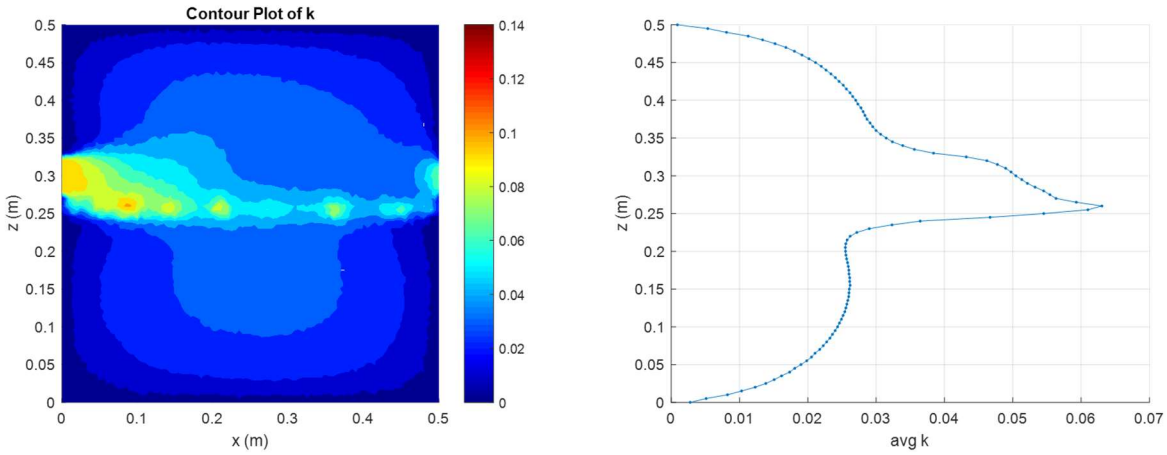

Figure 6.14. Contour *k* plot of a slice and average *k* along the z-axis for Configuration 1 fuel tank without objects, at Re = 2400.

For Configuration 2, the inlet is visible to the left of the center point on top edge and the outlet is faintly visible to the right (see Figure 6.15 to Figure 6.18). This is due to the outlet conditions to function as a pressure release to keep the pressure inside the fuel tank constant. At higher speeds, *k* is visible around the outlet as pressure increases as the inlet speed increases. The maximum average *k* along the z-axis is at $z = 0.255$ m for every inlet speed and decreases to a local minimum

around z = 0.29 m. Based on this the volume flow rate for Configuration 2 was also calculated at four locations: 0.255 m, 0.26 m, 0.275 m, and 0.29 m. The maximum for Configuration 2, a maximum of Configuration 1, the height of the top of the floating objects, and the local minimum for Configuration 2 respectively.

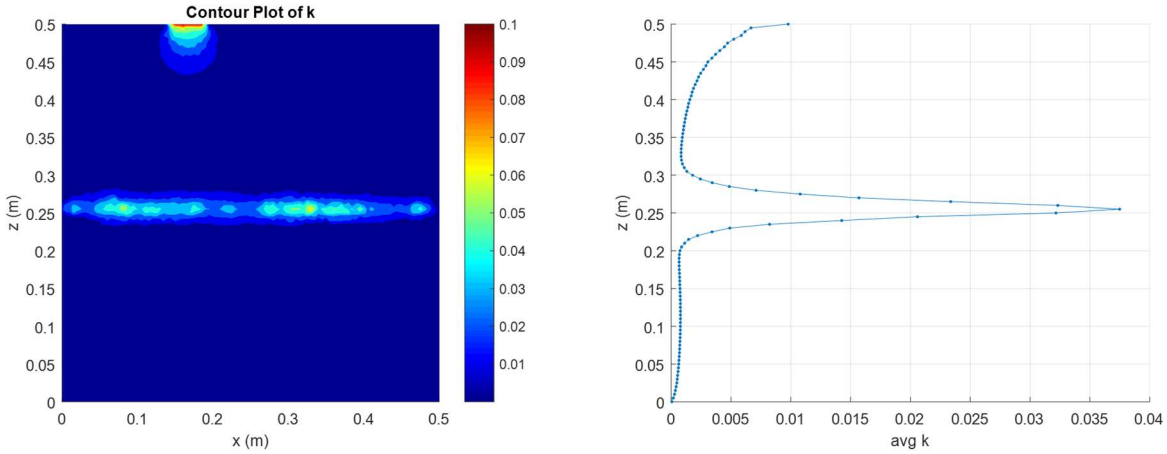

Figure 6.15. Contour *k* plot of a slice and average *k* along the z-axis for Configuration 2 fuel tank without objects, at Re = 340.

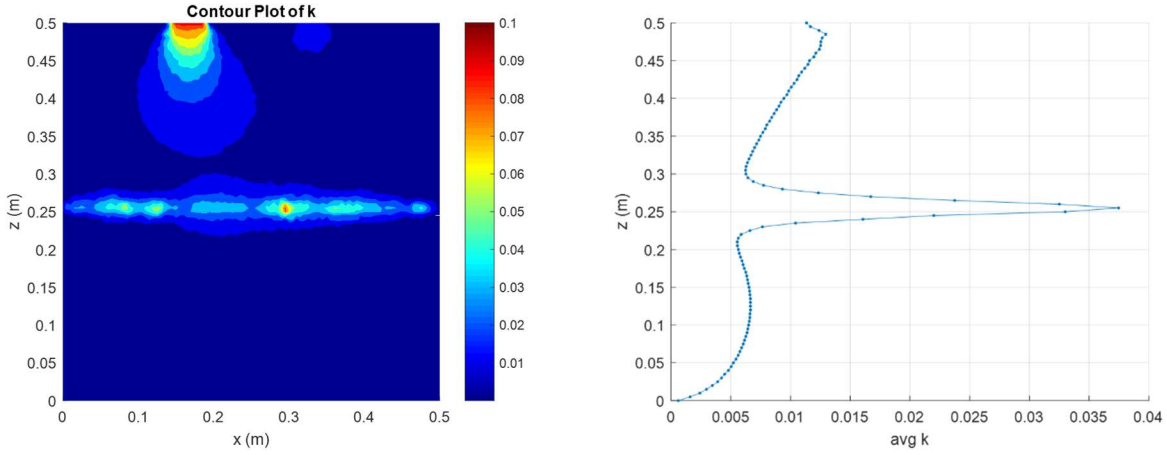

Figure 6.16. Contour *k* plot of a slice and average *k* along the z-axis for Configuration 2 fuel tank without objects, at Re = 1000.

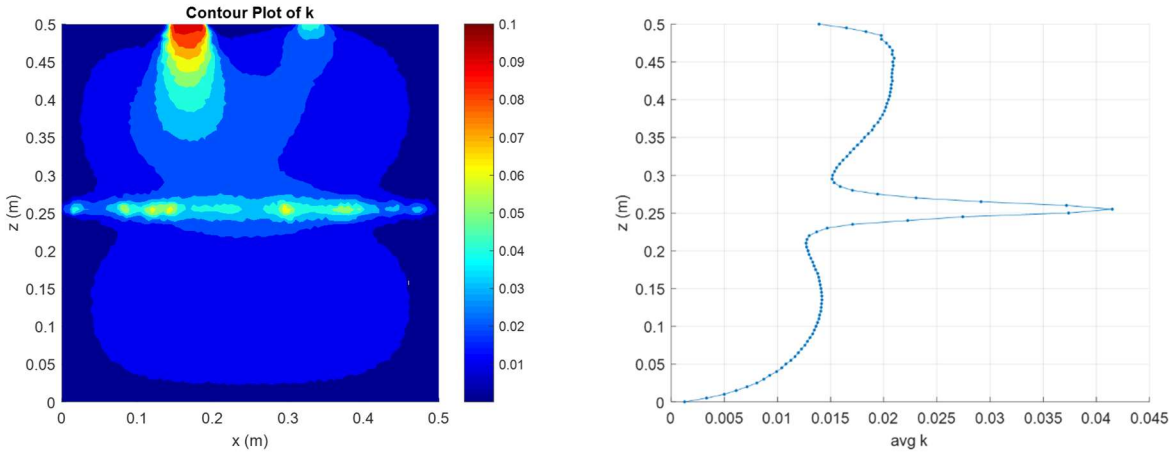

Figure 6.17. Contour *k* plot of a slice and average *k* along the z-axis for Configuration 2 fuel tank without objects, at Re = 1700.

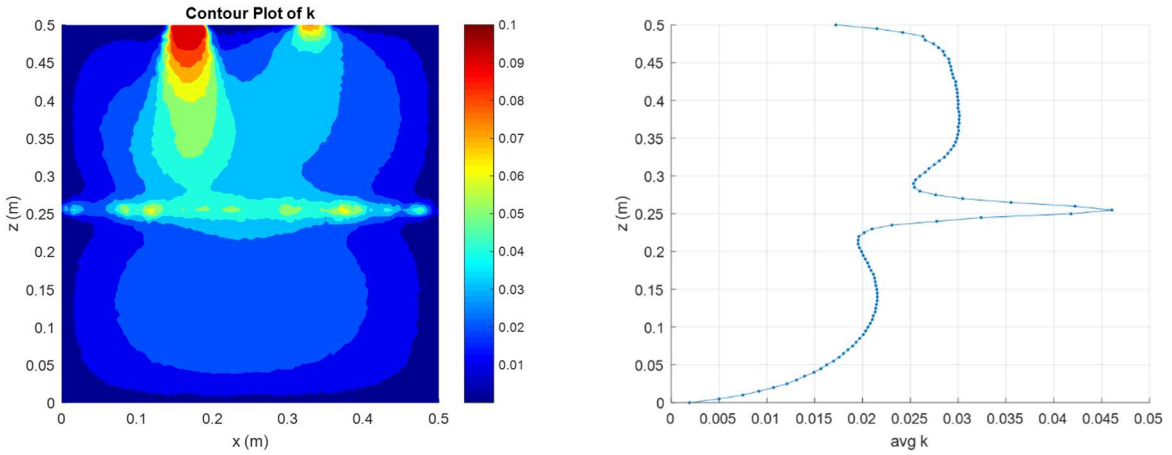

Figure 6.18. Contour *k* plot of a slice and average *k* along the z-axis for Configuration 2 fuel tank without objects, at Re = 2400.

6.3 CONFIGURATION 1, TANK WITHOUT OBJECTS

Configuration 1 of the fuel tank without objects is shown in Figure 6.19. This simulation was run at inlet speeds Re = 10 – 2400 and the results are taken at the maximum timesteps listed in Table 6.4.

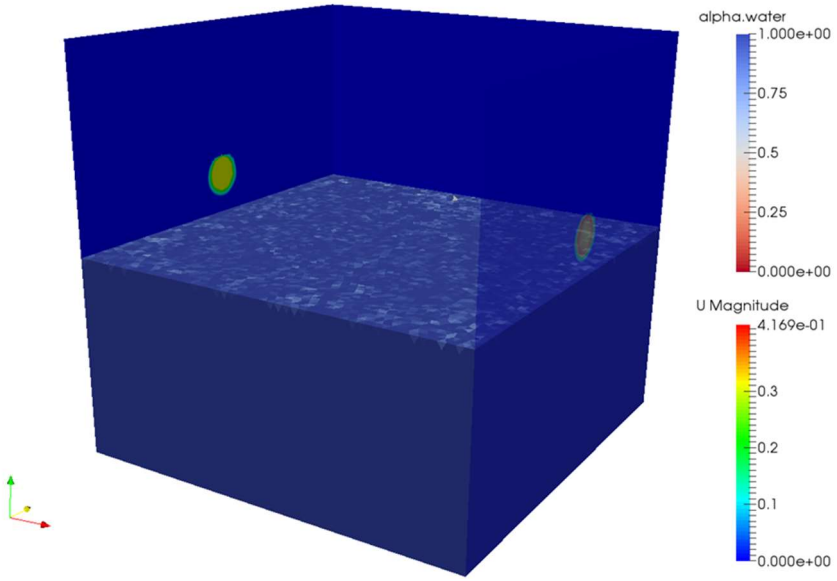

Figure 6.19. Configuration 1 fuel tank, with inlet and outlet on the side walls close to the fluid surface.

6.3.1 *Volume Flow Rate and Mass Flow Rate*

The volume flow rate and mass flow rate for the fuel tank without objects are shown in Figure 6.20 and Figure 6.21 respectively. The volume flow rate sharply decreases from Re = 10 to 340 and continues to gradually decrease from Re = 340 to 2400 at dz/L = 0.01 and 0.02. At dz/L = 0.05 and 0.08 above the water surface, the volume flow rate gradually increases. The volume flow rate for Re = 340 to 2400 can be modeled by the power equations (dotted lines in Figure 6.22) at dz/L = 0.01, 0.02, 0.05, and 0.08 respectively:

$$\dot{V}_{water} = 0.0791\mathrm{Re}^{-0.017} \quad (6.1)$$

$$\dot{V}_{water} = 0.0768\mathrm{Re}^{-0.012} \quad (6.2)$$

$$\dot{V}_{water} = 0.0434\mathrm{Re}^{0.0183} \quad (6.3)$$

$$\dot{V}_{water} = 0.0194\mathrm{Re}^{0.0787}\,, \quad (6.4)$$

where Re is the Reynolds number of the inlet. The volume flow rate of water vapor normalized by the volume flow rate of the inlet is shown in Figure 6.23. As the inlet speed increases, the normalized volume flow rate decreases.

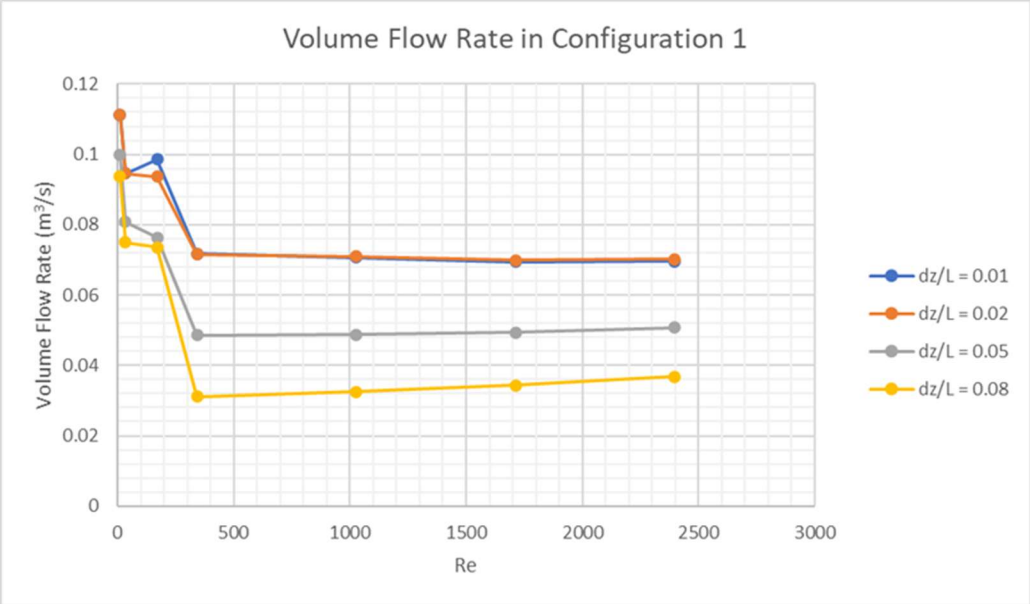

Figure 6.20. Volume flow rate for Configuration 1 fuel tank.

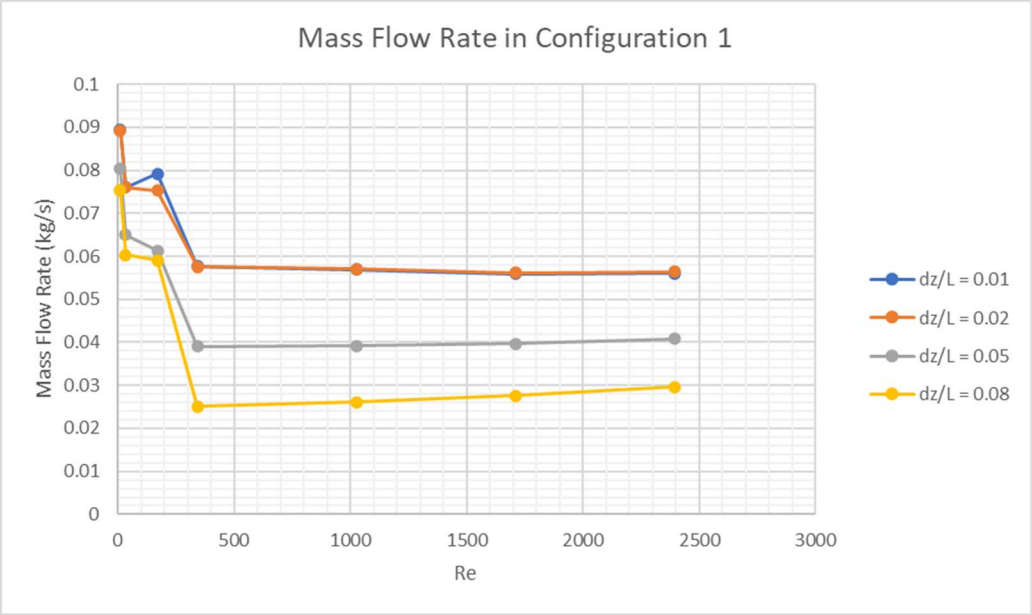

Figure 6.21. Mass flow rate for Configuration 1 fuel tank.

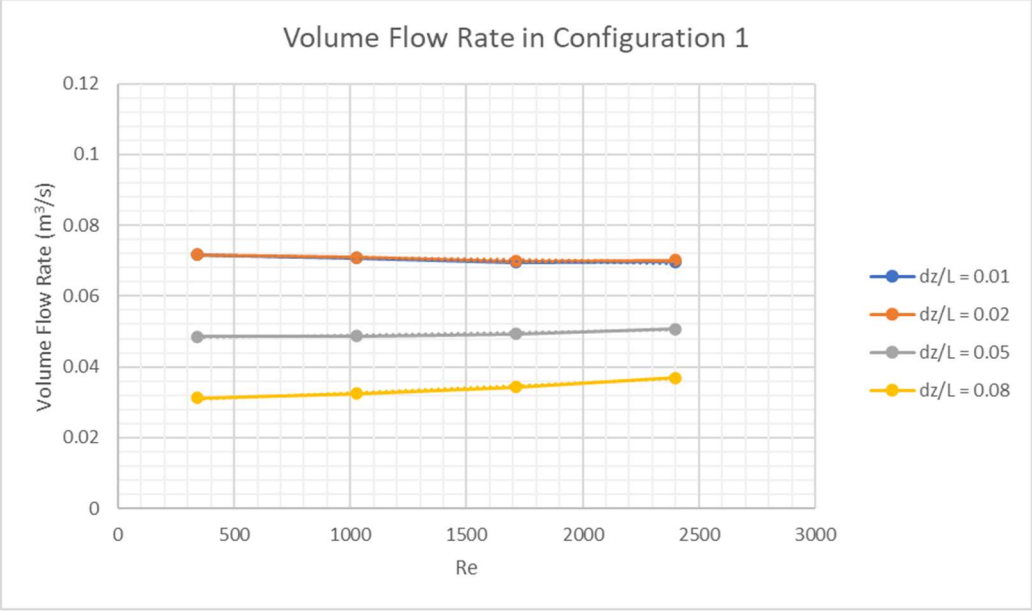

Figure 6.22. Trendlines for volume flow rate at Re = 340 – 2400, Configuration 1 fuel tank.

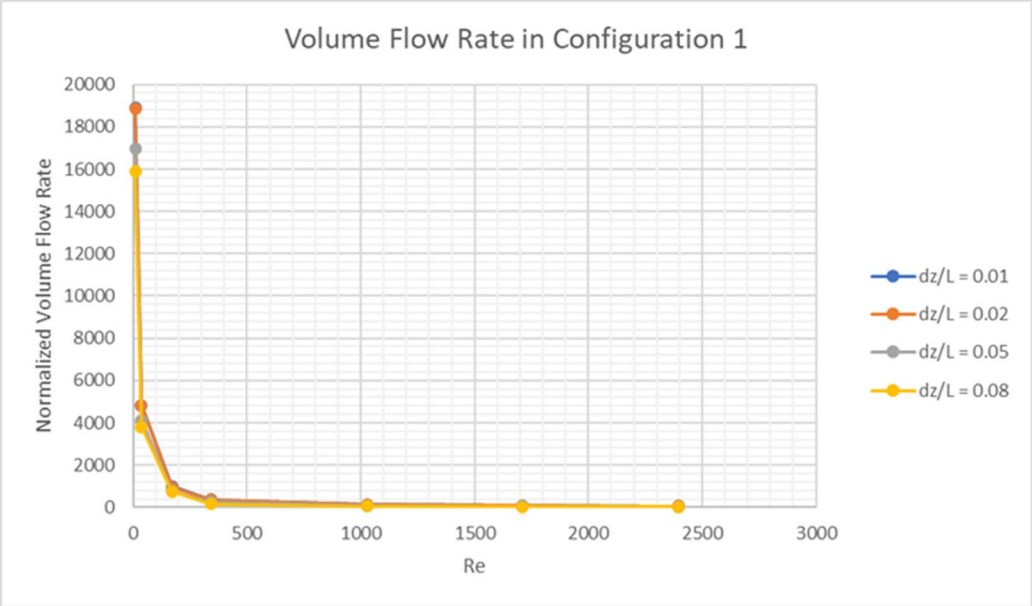

Figure 6.23. Normalized volume flow rate for Configuration 1 fuel tank.

For inlet speeds Re = 10 to 340 (0.003 m/s to 0.1 m/s) the volume flow rate decreases with a slight increase at Re = 170 (0.05 m/s). This decrease does not match trend observed by Lyulin and Kabov where the evaporation rate increased as the inlet gas velocity increases between 0.003 m/s and 0.16 m/s [4]. This discrepancy is most likely due to the walls of the enclosed fuel tank creating a non-uniform flow over the water surface and a round inlet jet with a finite spreading angle.

A visual study of the velocity indicates that the flow pattern changes at Re = 170 (Figure 6.26). The velocity magnitude of a slice through the center of the fuel tank along the y-axis shows a change in the flow pattern as the inlet speed increases (see Figure 6.24 to Figure 6.30). Note that the tetrahedral cell data shown is not interpolated, and the inlet is to the left and the outlet is to the right. The non-zero velocity on the air-water interface and in the water is due to the simulation capturing movement in the water surface as air moves over it.

As shown, the highest velocity is along the water surface and near the outlet for inlet speeds Re = 10 and 30. This is due to the effect of buoyancy. For low inlet speeds the Richardson number

is large (listed in Table 6.5), meaning that the trajectory of the inlet jet is dominated buoyancy and sinks closer to the water surface due to the difference in air and water vapor density. The Richardson number is a dimensionless number that is estimated by

$$\mathrm{Ri} = g' \frac{L}{U^2} \tag{6.5}$$

$$g' = g \frac{\rho_{air} - \rho_{vapor}}{\rho_{air}}, \tag{6.6}$$

where L is the inlet diameter 0.05 m, U is the inlet speed, g is gravity, ρ_{air} is the density of air 1.225 kg/m^3, and ρ_{vapor} is the density of water vapor 0.804 kg/m^3 [13].

Table 6.5. Estimated Richardson number for each inlet speed

Re	**Ri**
10	18700
30	1700
170	70
340	20
1000	1.9
1700	0.7
2400	0.3

At inlet speed Re = 170 there appears to be a stationary vortex forming about one-third of the distance from the inlet. Then from inlet speeds Re = 340 – 2400, the velocity profiles look similar as the flow pattern inside the tank stabilizes and buoyancy is not the dominate effect on the trajectory of the inlet jet.

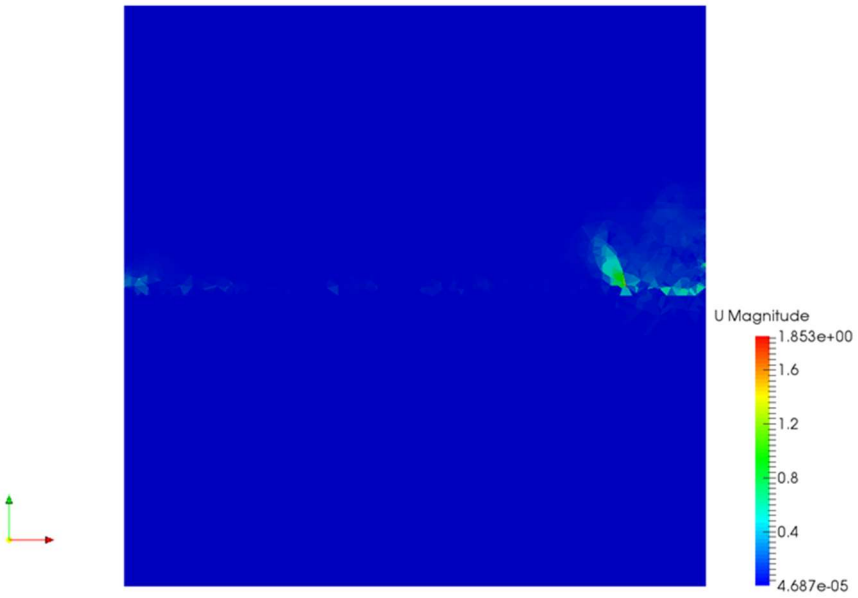

Figure 6.24. Velocity profile of a slice in the center, at Re = 10.

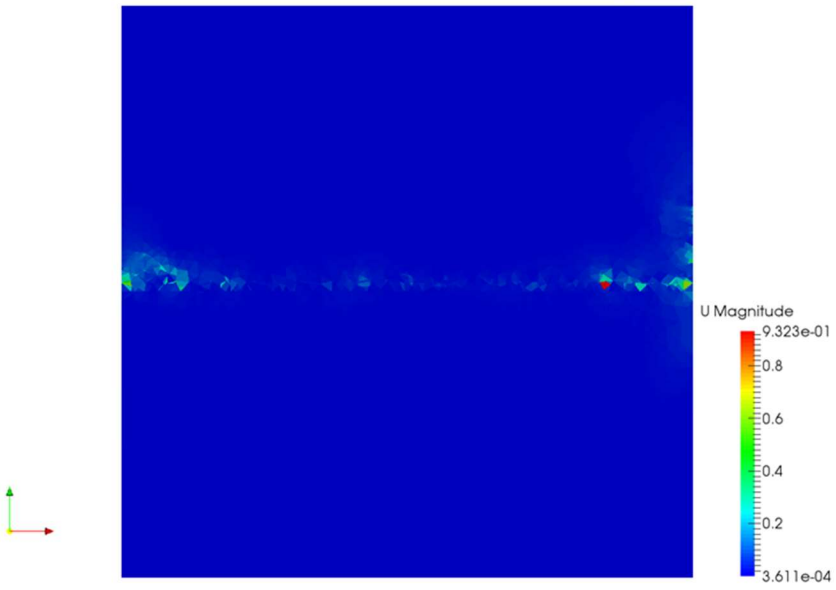

Figure 6.25. Velocity profile of a slice in the center, at Re = 30.

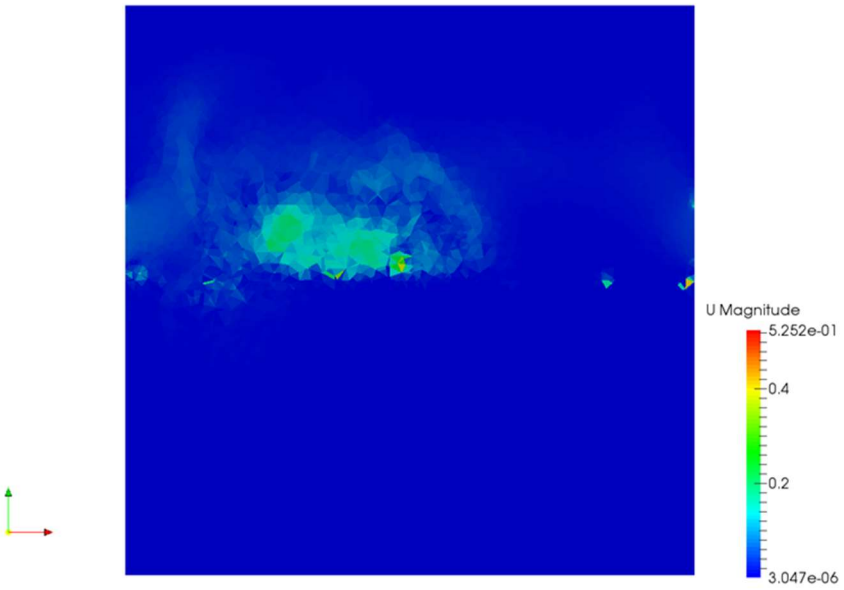

Figure 6.26. Velocity profile of a slice in the center, at Re = 170.

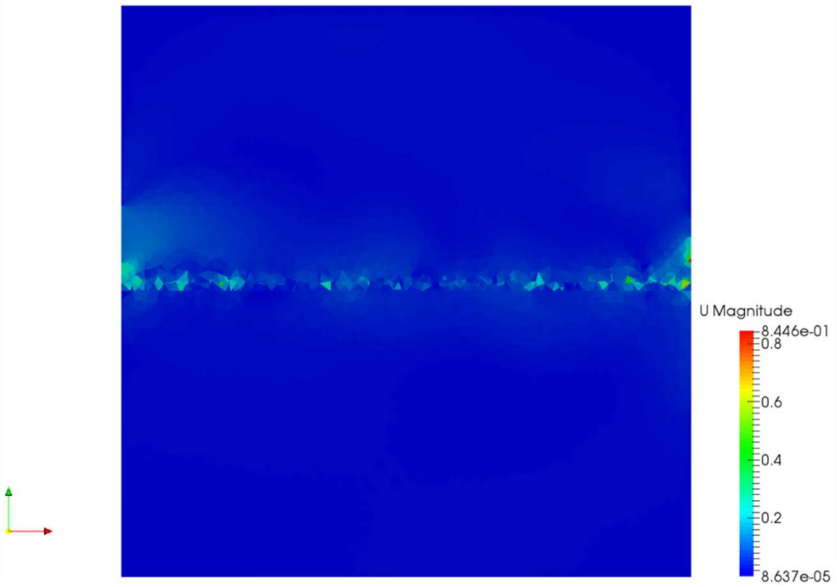

Figure 6.27. Velocity profile of a slice in the center, at Re = 340.

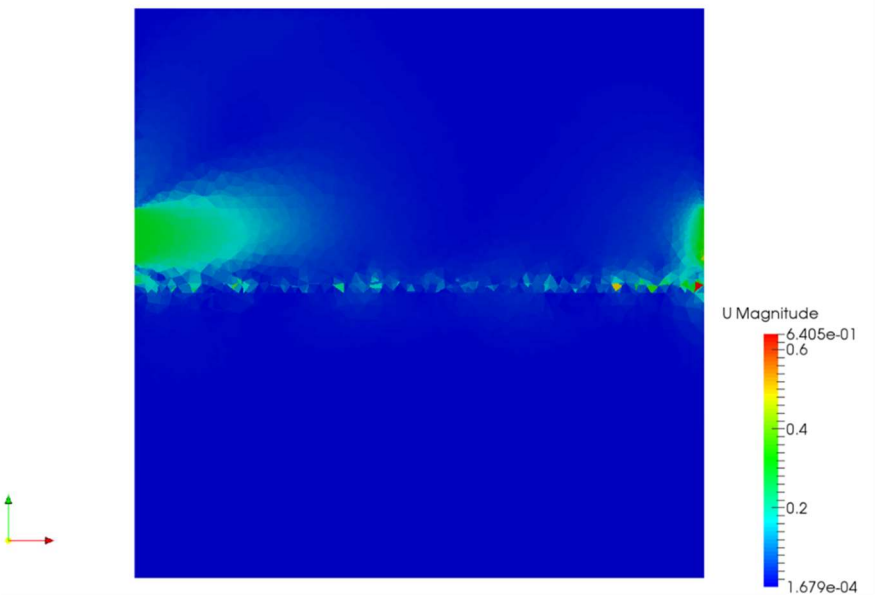

Figure 6.28. Velocity profile of a slice in the center, at Re = 1000.

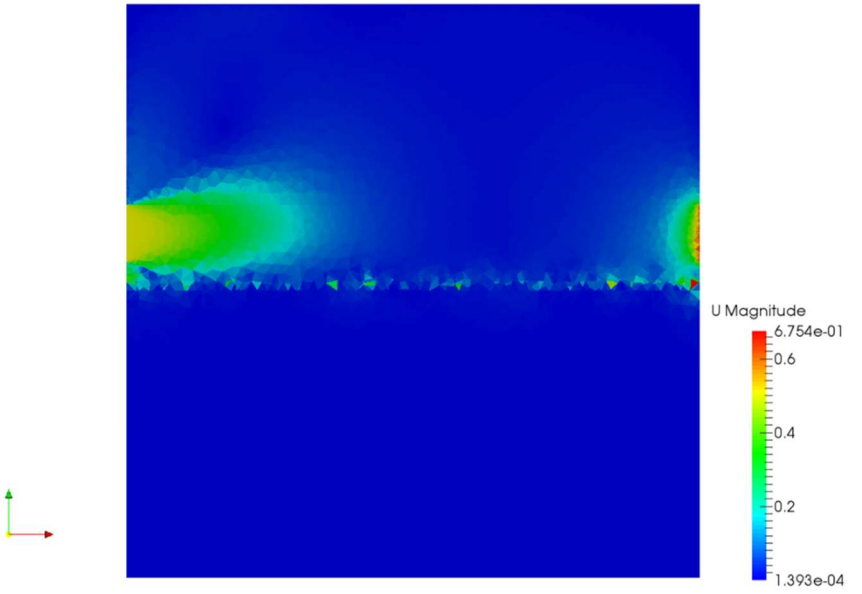

Figure 6.29. Velocity profile of a slice in the center, at Re = 1700.

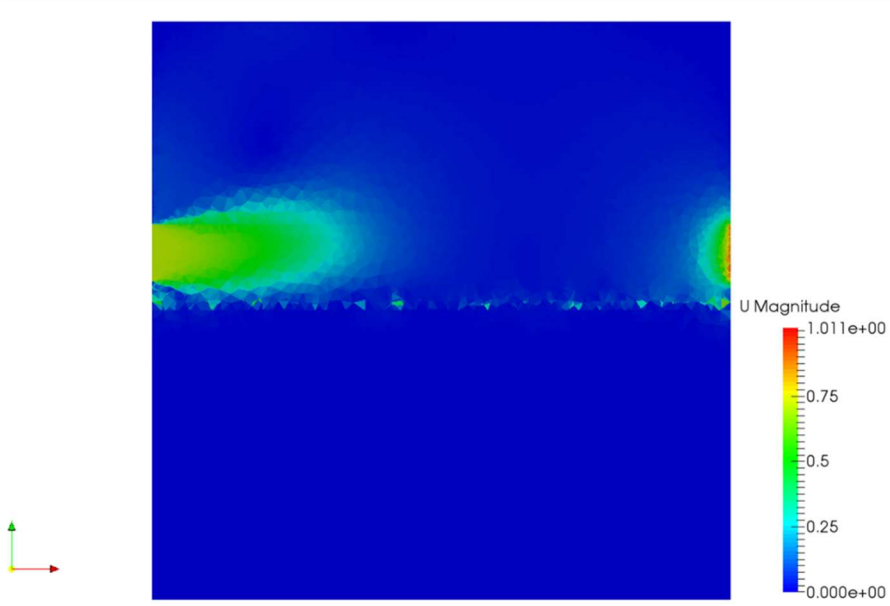

Figure 6.30. Velocity profile of a slice in the center, at Re = 2400.

The velocity vectors for the center slice of the fuel tank clearly show the change in the flow field, see Figure 6.31 to Figure 6.37. For the inlet speeds below Re = 170, the air is circulating counterclockwise throughout the upper half of the fuel tank. At Re = 340, the flow begins to develop a straight path along the water surface from the inlet to the outlet with the counterclockwise vortex feeding into it. As the inlet speed increases, the vortex moves to the upper left corner as the inlet jet begins to spread upward. This is due to the water surface acting as a flat plate impinging on the spreading angle of the inlet jet causing the inlet flow to redirect away from the water surface. The transition between these two flow patterns occurs around Re = 170, as shown in Figure 6.33.

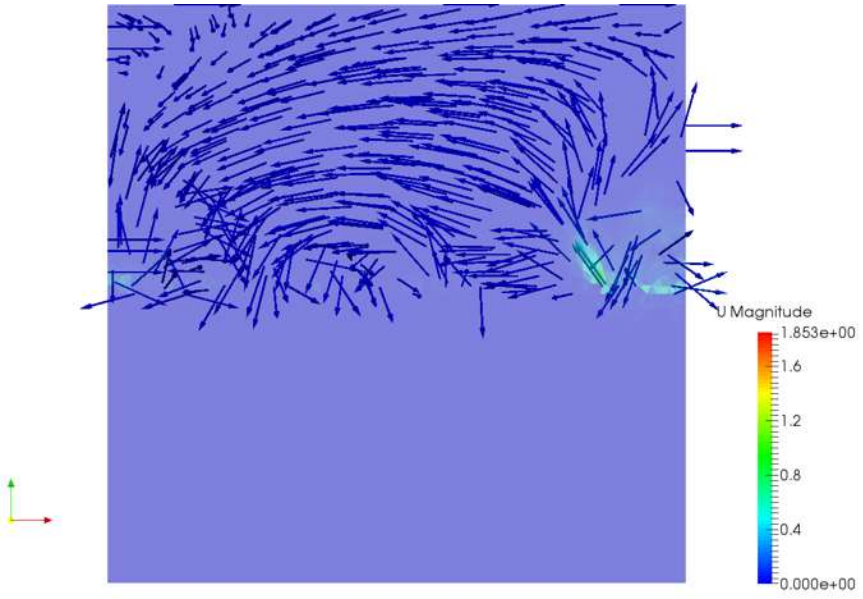

Figure 6.31. Velocity vectors of a slice through the center, at Re = 10.

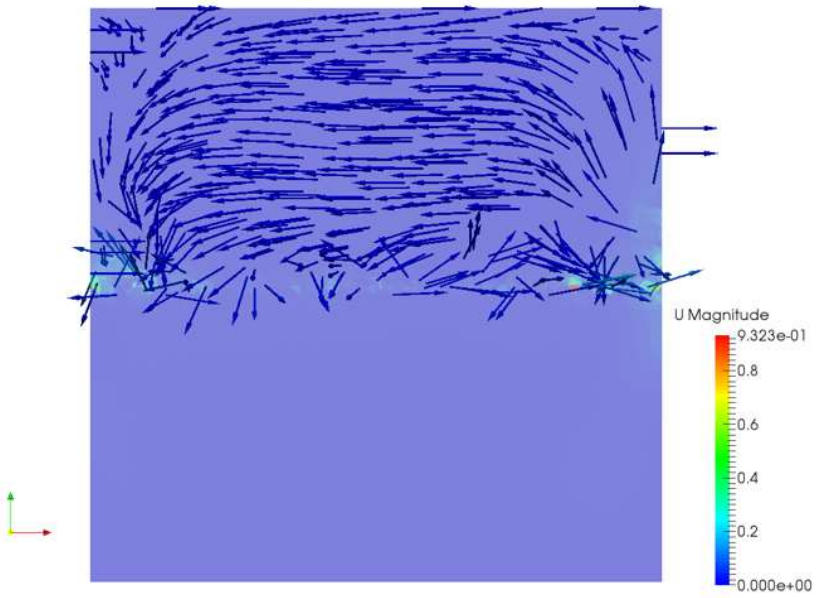

Figure 6.32. Velocity vectors of a slice through the center, at Re = 30.

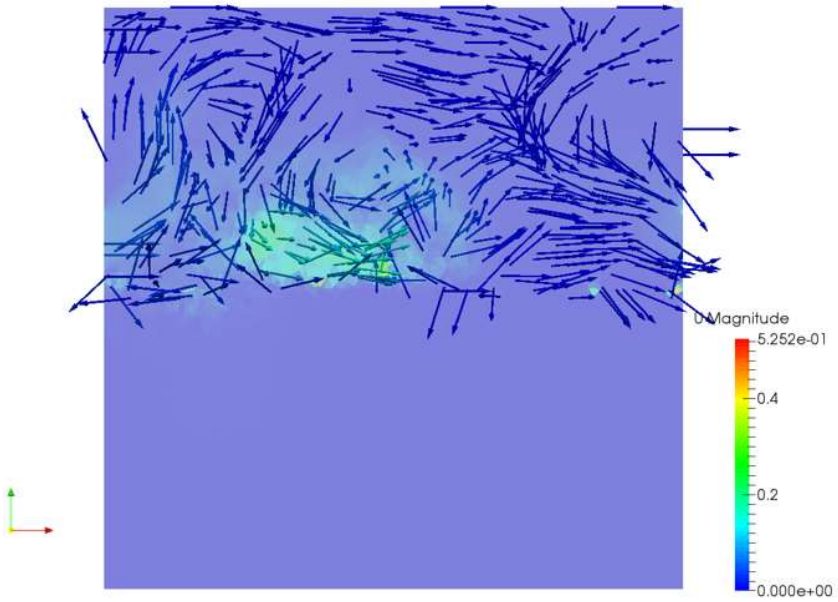

Figure 6.33. Velocity vectors of a slice through the center, at Re = 170.

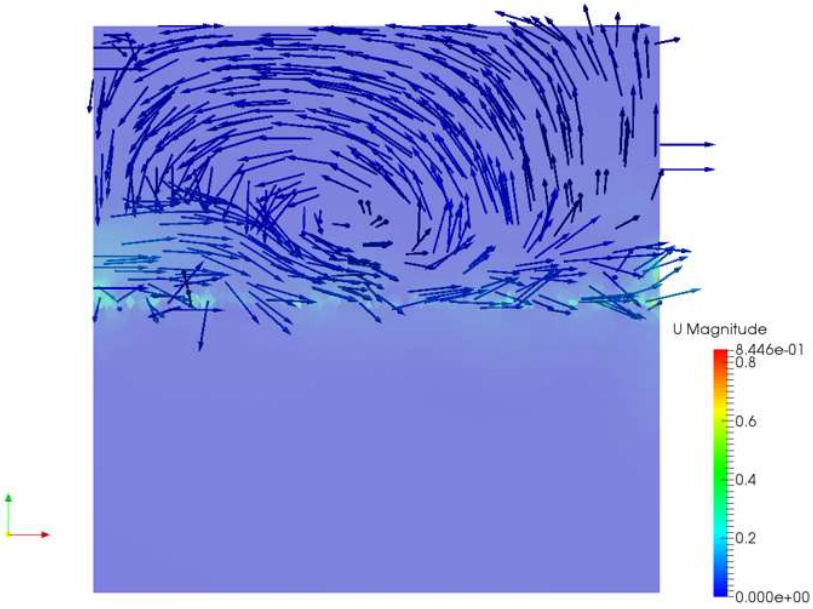

Figure 6.34. Velocity vectors of a slice through the center, at Re = 340.

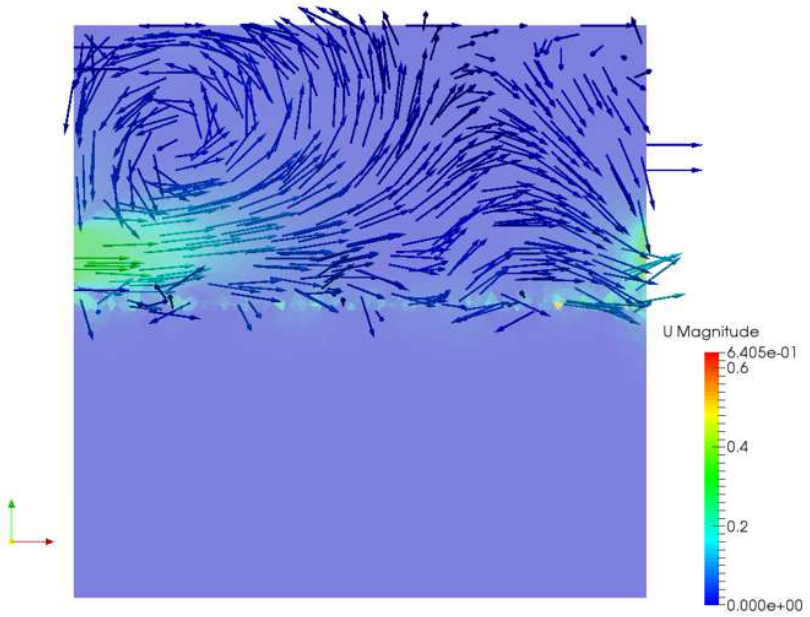

Figure 6.35. Velocity vectors of a slice through the center, at Re = 1000.

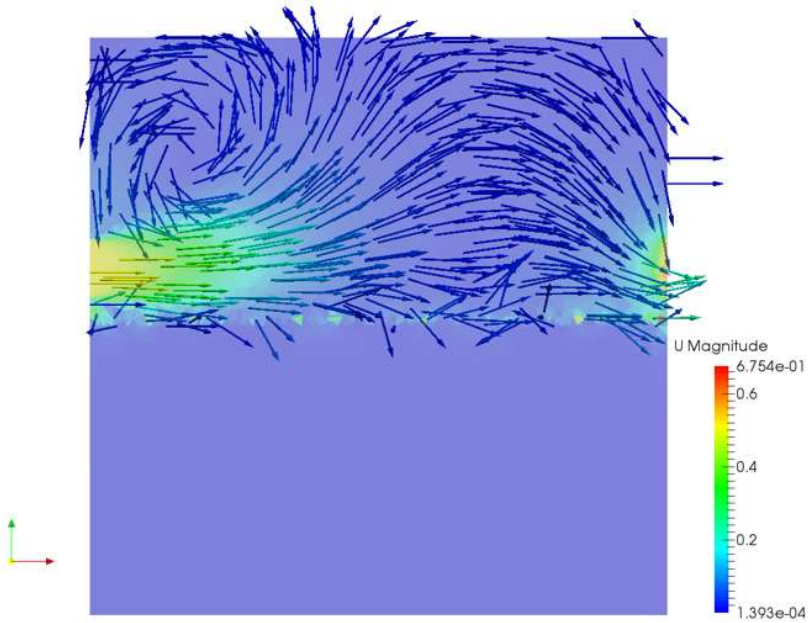

Figure 6.36. Velocity vectors of a slice through the center, at Re = 1700.

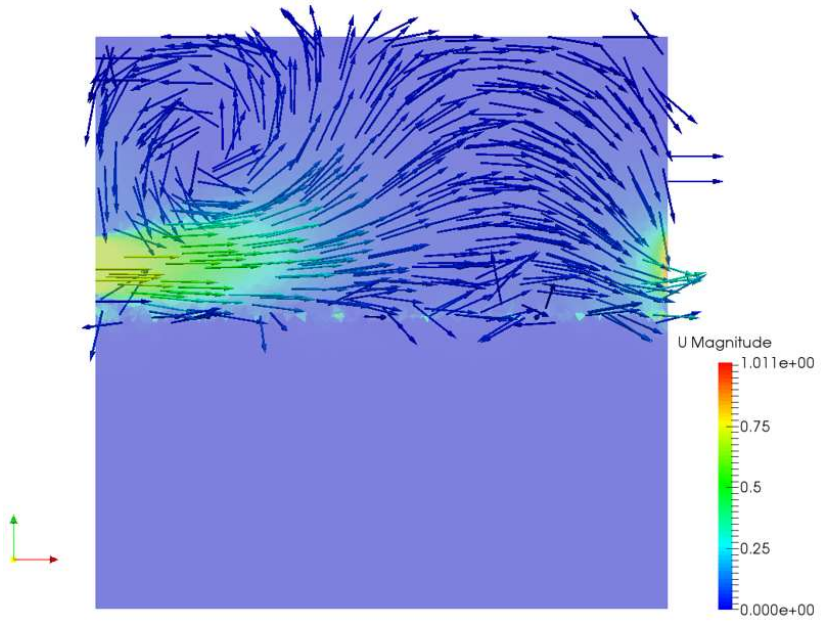

Figure 6.37. Velocity vectors of a slice through the center, at Re = 2400.

Further analysis of the streamlines clearly shows the transition in flow patterns at Re = 170 (Figure 6.38 to Figure 6.44). The streamlines of the flow field are tracked at two points: close to the wall at the center of the inlet with coordinates (0.01, 0.25, 0.3) and the center point between the inlet and outlet with coordinates (0.25, 0.25, 0.3). As shown in Figure 6.38, Figure 6.39, and Figure 6.40, the flow stays close to the water surface forming small eddies. Since mixing and entrainment is caused by small eddies, it is reasonable that the volume flow rate at these inlet speeds is greater than the volume flow rate at Re = 340 – 2400.

As the inlet speed increases to Re ≥ 340, the flow begins to roll up near the inlet to form a large vortex and more flow is directed straight to the outlet. Combined with the inlet jet spreading angle rising upward, less air flow is driven downward causing less mixing to occur near the water surface thus the volume flow rate at dz/L = 0.01 and 0.02 decreases as the inlet speed increases. At dz/L = 0.05 and 0.08 the volume flow rate increases as the inlet speed increases (see Figure 6.45), as expected. These heights correspond to the bottom edge of the inlet jet and near the middle

of the inlet jet. Streamlines that go directly from the inlet to the outlet can be seen dipping slightly in the center of the fuel tank to cause mixing.

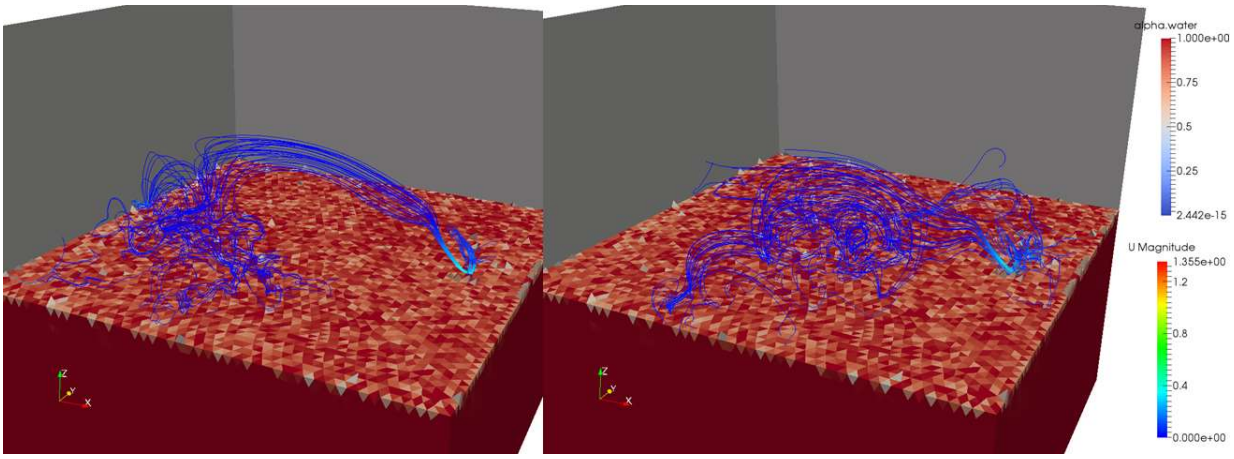

Figure 6.38. Streamlines at the inlet and center of the tank, at Re = 10.

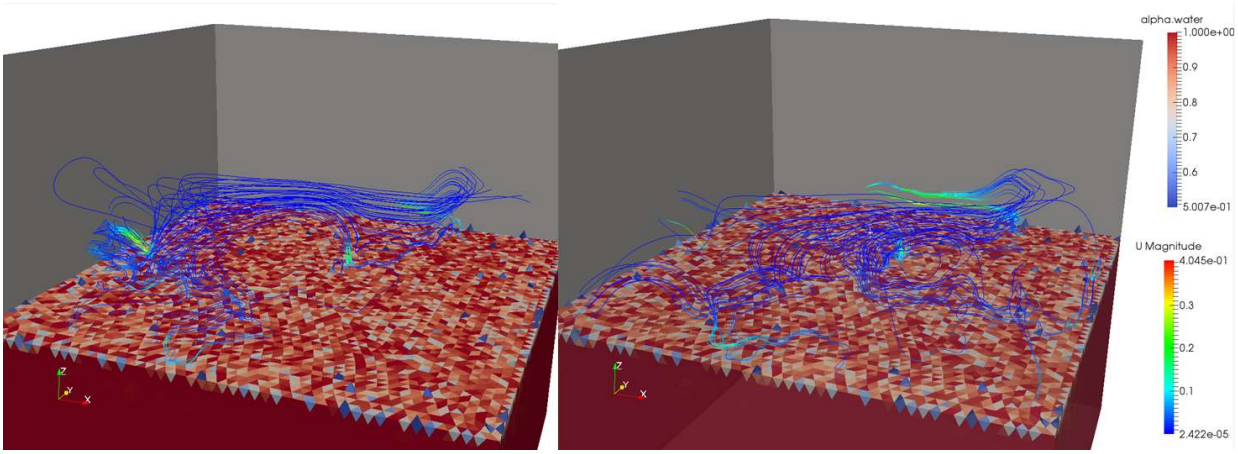

Figure 6.39. Streamlines at the inlet and center of the tank, at Re = 30.

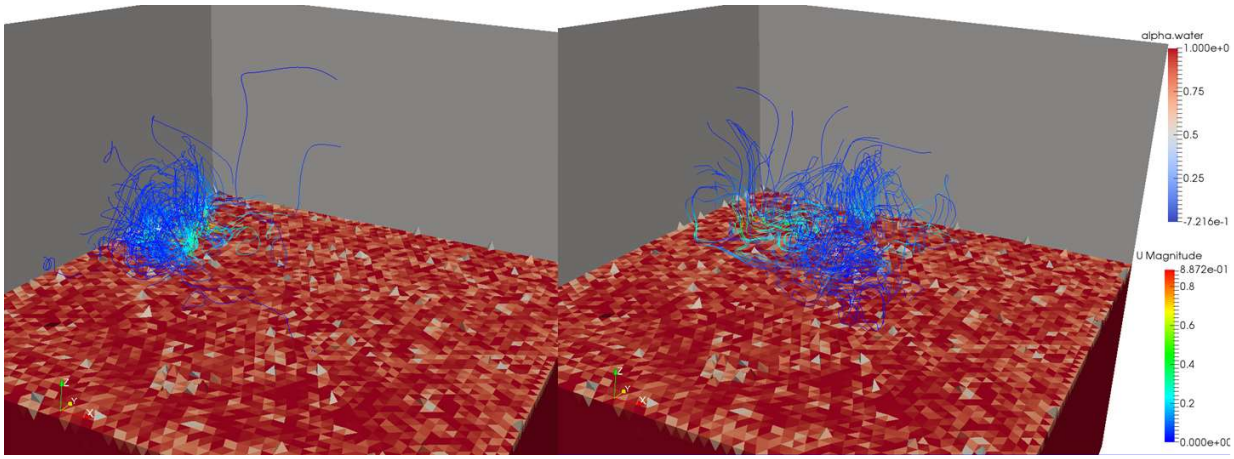

Figure 6.40. Streamlines at the inlet and center of the tank, at Re = 170.

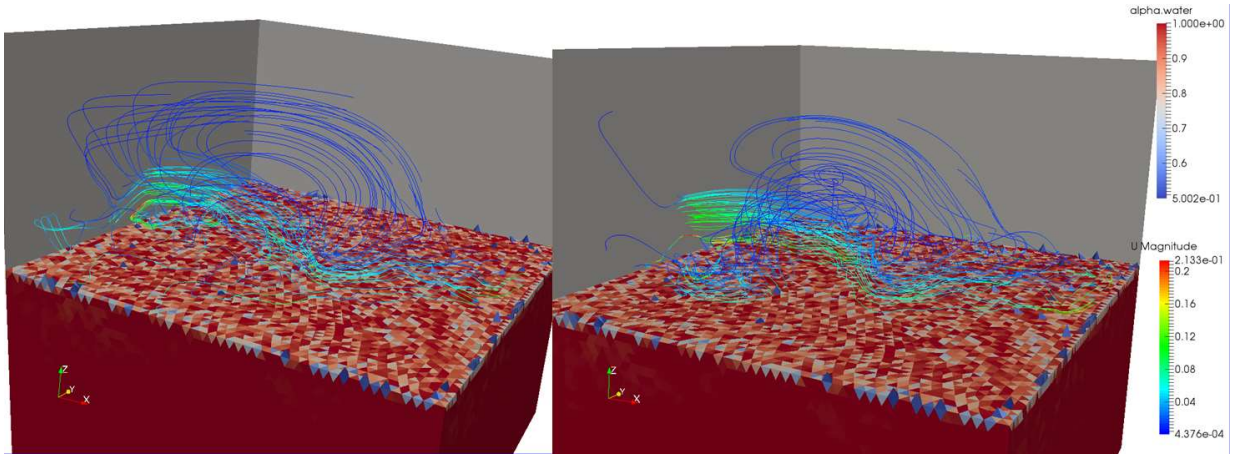

Figure 6.41. Streamlines at the inlet and center of the tank, at Re = 340.

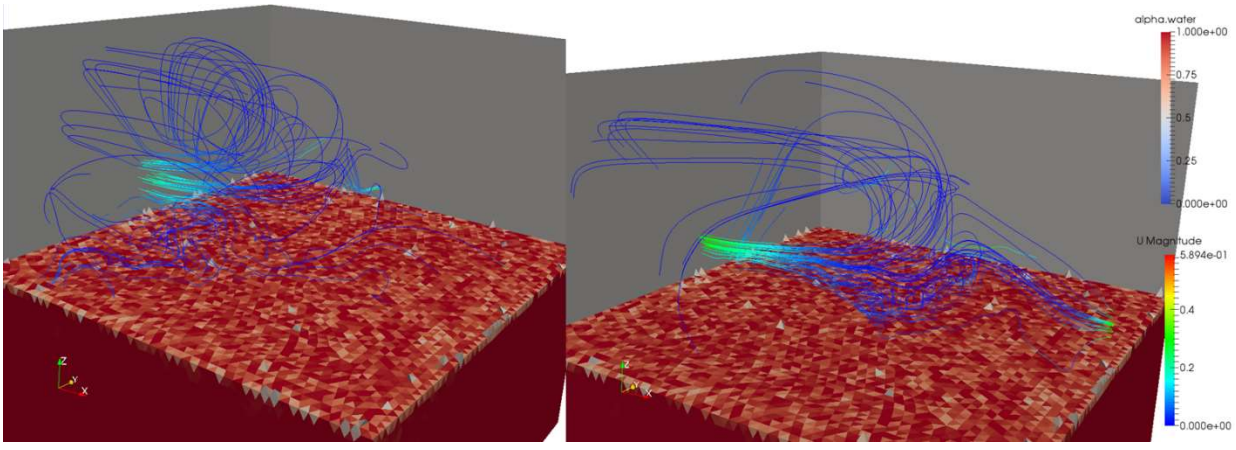

Figure 6.42. Streamlines at the inlet and center of the tank, at Re = 1000.

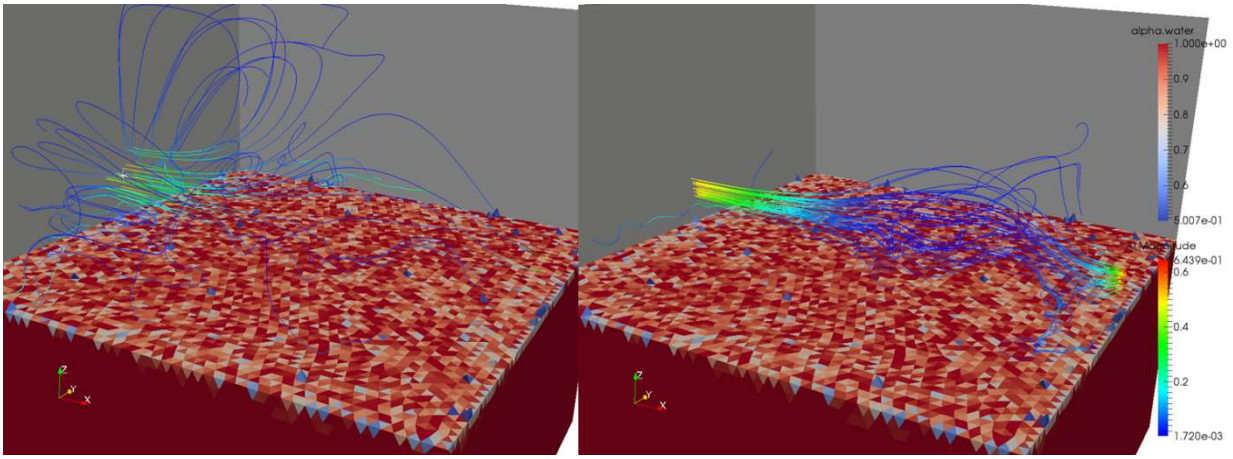

Figure 6.43. Streamlines at the inlet and center of the tank, at Re = 1700.

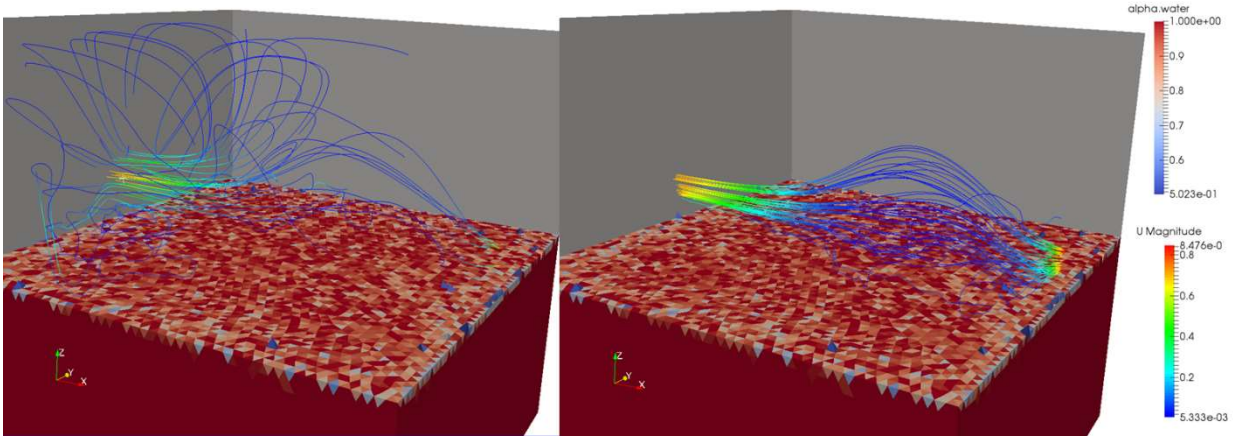

Figure 6.44. Streamlines at the inlet and center of the tank, at Re = 2400.

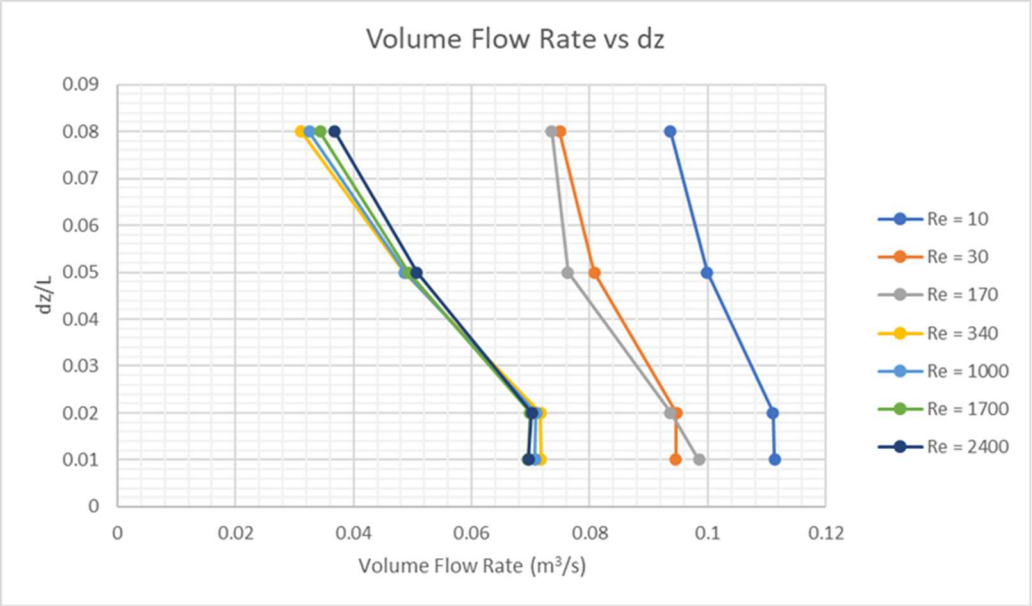

Figure 6.45. Volume flow rate vs distance above the water surface for Configuration 1 fuel tank.

Convective flow of the liquid layer in the direction opposite of the air flow has been shown to increase the evaporation in experimental results [4]. The velocity vectors for the liquid layer, shown in Figure 6.46 to Figure 6.52, indicates that there is clockwise convective flow in the liquid layer for all inlet speeds except Re = 170. The clockwise convective flow is moving in the direction of the air flow and therefore is not a contributing factor to the volume flow rate. Interestingly, the center of the convective flow moves to the right and closer to the water surface for inlet speeds Re = 340 and greater.

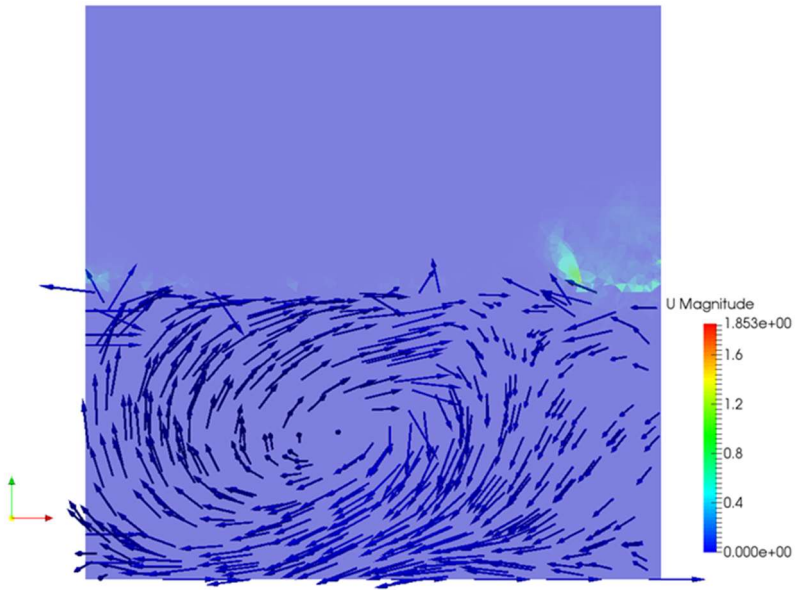

Figure 6.46. Convective flow in the liquid layer, at Re = 10.

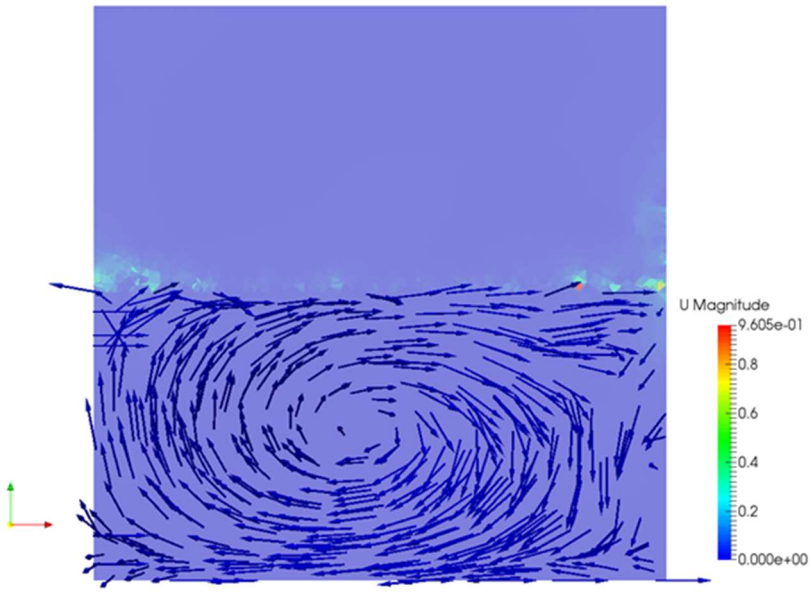

Figure 6.47. Convective flow in the liquid layer, at Re = 30.

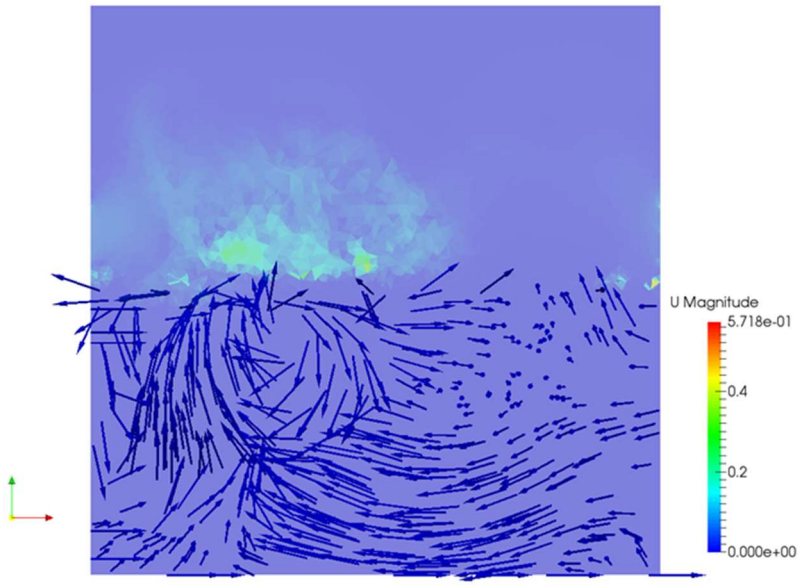

Figure 6.48. Convective flow in the liquid layer, at Re = 170.

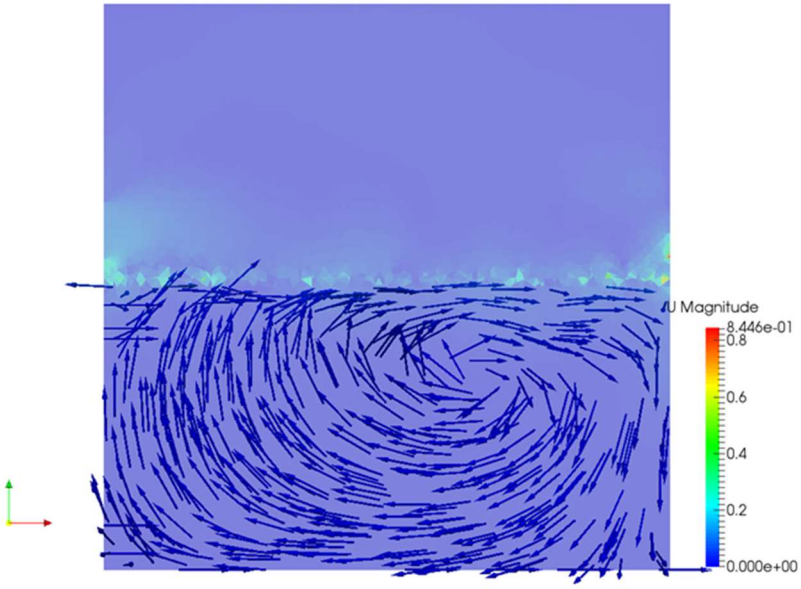

Figure 6.49. Convective flow in the liquid layer, at Re = 340.

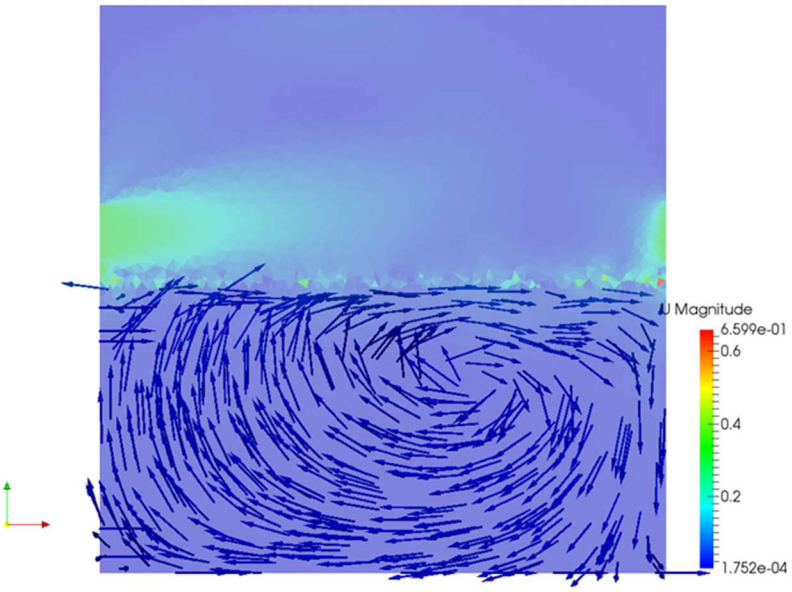

Figure 6.50. Convective flow in the liquid layer, at Re = 1000.

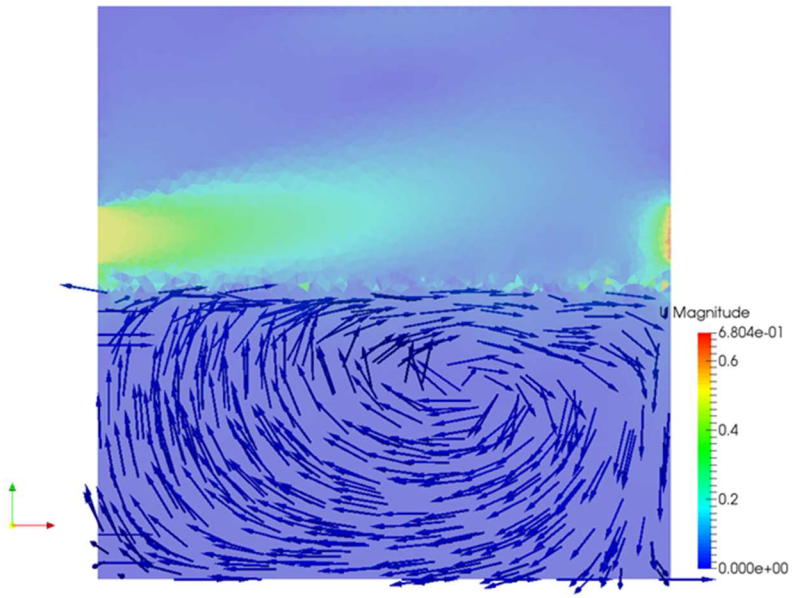

Figure 6.51. Convective flow in the liquid layer, at Re = 1700.

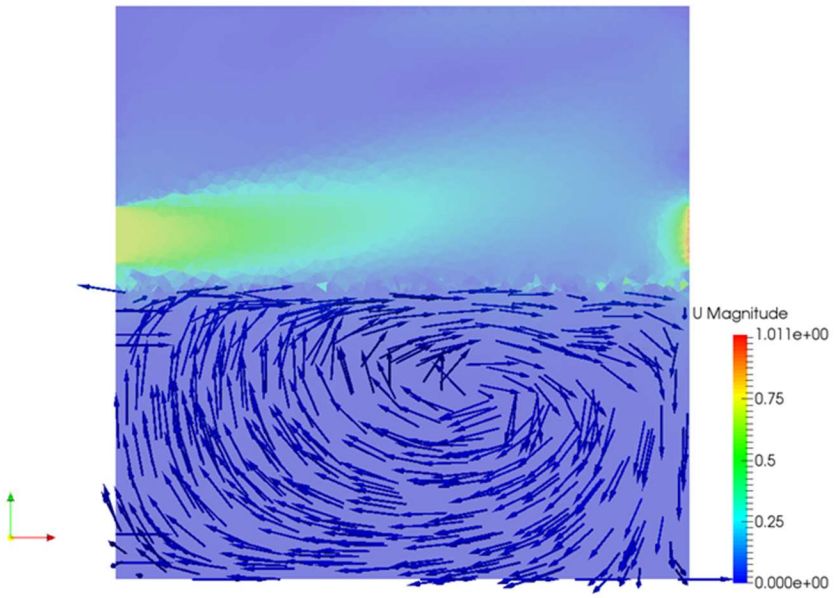

Figure 6.52. Convective flow in the liquid layer, at Re = 2400.

6.3.2 *Volume Concentration of Water Vapor*

The volume concentration of water vapor, shown in Figure 6.53, decreases as the inlet speed and the distance from the water surface increases. This is expected because the volume flow rate of the jet increases at a faster rate than the volume flow rate of vapor. Also, the concentration of water vapor decreases farther from the water surface as it mixes with dry air, shown in Figure 6.54. The trendlines for vapor concentration at dz/L = 0.01, 0.02, 0.05, and 0.08 are respectively given by

$$C_{water} = -8e^{-6}\mathrm{Re} + 1.0001 \tag{6.7}$$

$$C_{water} = -8e^{-6}\mathrm{Re} + 1.0001 \tag{6.8}$$

$$C_{water} = -1e^{-5}\mathrm{Re} + 1.0001 \tag{6.9}$$

$$C_{water} = -2e^{-5}\mathrm{Re} + 0.9999\ , \tag{6.10}$$

where Re is the Reynolds number of the inlet.

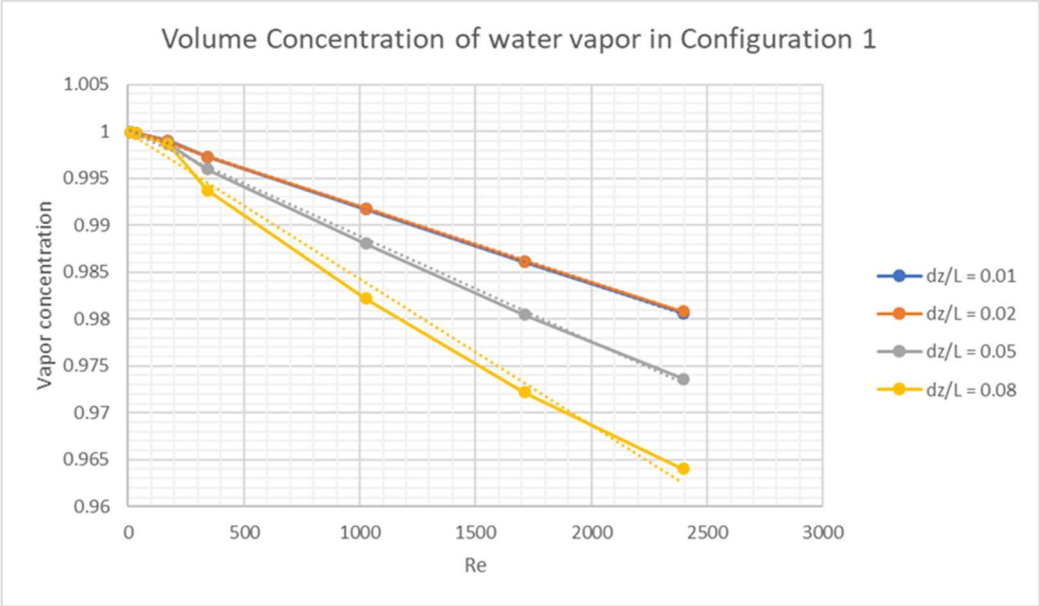

Figure 6.53. Volume concentration of water vapor for Configuration 1 fuel tank with trendlines (dotted line).

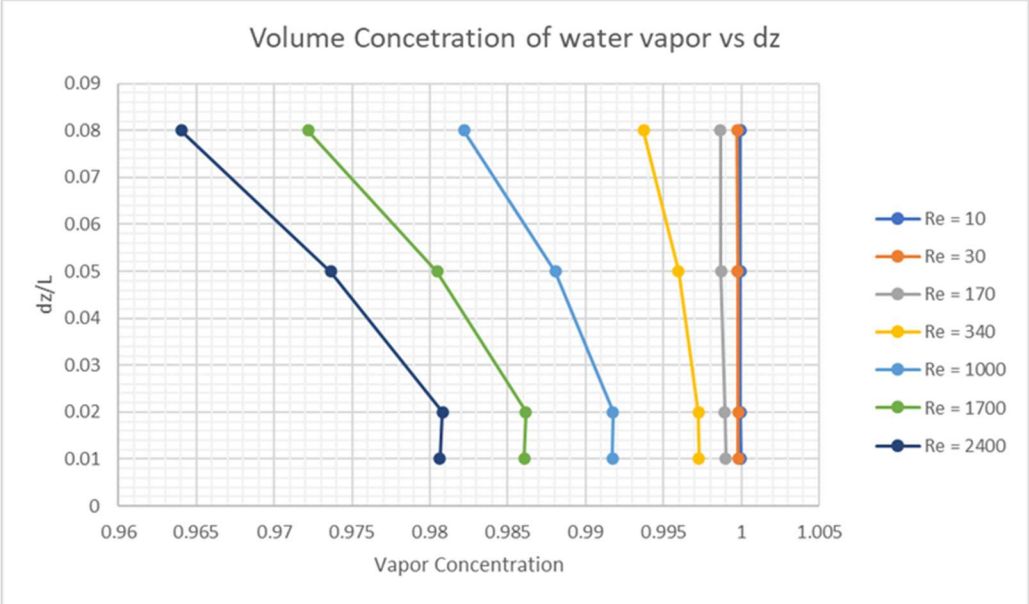

Figure 6.54. Volume concentration of water vapor vs distance above the water surface for Configuration 1 fuel tank.

By increasing the inlet speed, the volume concentration of water vapor close to the water surface decreased about 2 – 2.5% at Re = 2400 when compared to Re = 10. The lower flammability limit of kerosene (Jet A-1) is 0.6% and the upper flammability limit is 4.6% by volume [14]. Flight TWA 800 required 1.4% evaporation of the fuel in the central fuel tank to reach the lower flammability limit [3]. That corresponds to a fuel vapor concentration of 0.0053% to reach the lower flammability limit. Assuming the volume flow rate and vapor concentration is about the same for kerosene, then a 2% reduction of the volume concentration of vapor at the highest inlet speed would be significant.

6.4 Configuration 2, Tank Without Objects and With Floating Objects

Simulations with Configuration 2 of the fuel tank were run at inlet speeds Re = 340 – 2400. The geometry of the fuel tank configurations are shown in Figure 6.55 to Figure 6.59. The naming convention used in this thesis for the various floating object arrays is the total number followed by the shape of the floating objects inside.

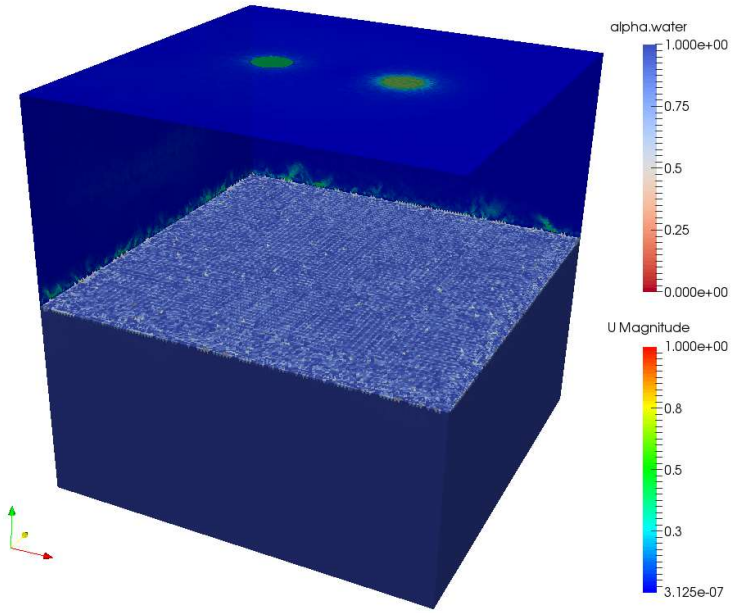

Figure 6.55. Configuration 2 fuel tank – Without Objects.

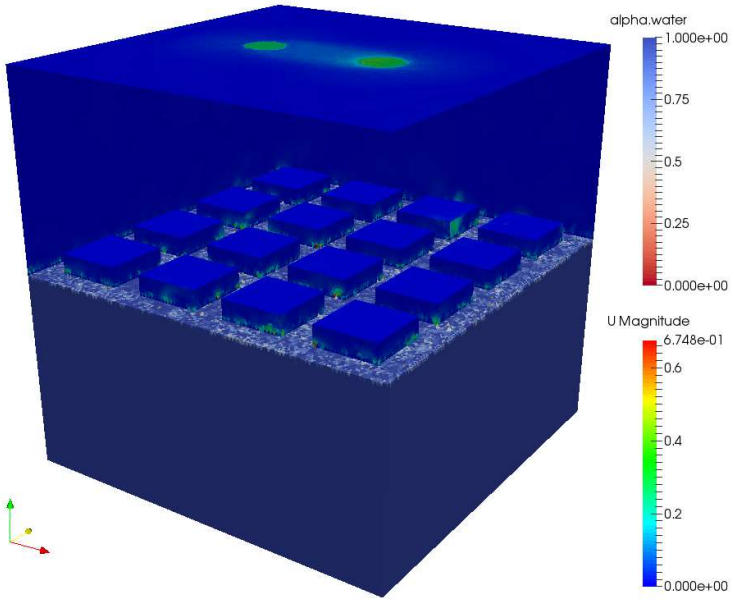

Figure 6.56. Configuration 2 fuel tank with rectangular floating objects – 16 Rectangles.

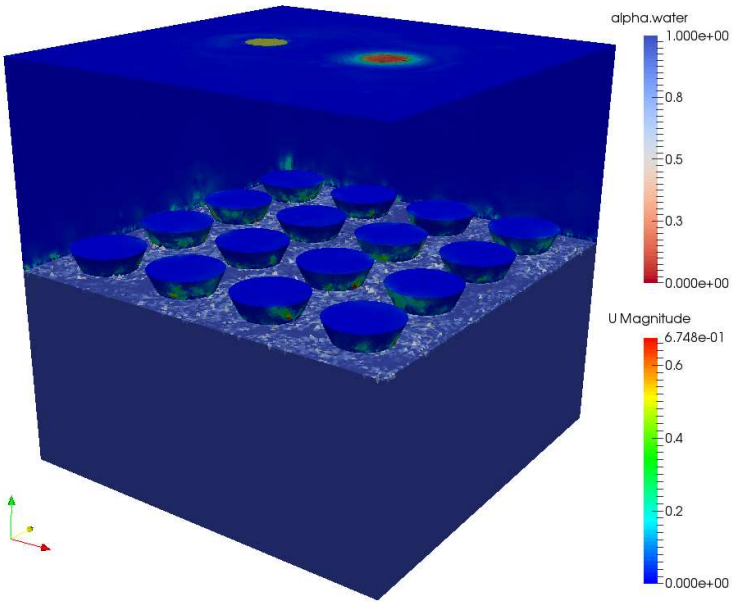

Figure 6.57. Configuration 2 fuel tank with Large inverted cones – 16 Cones.

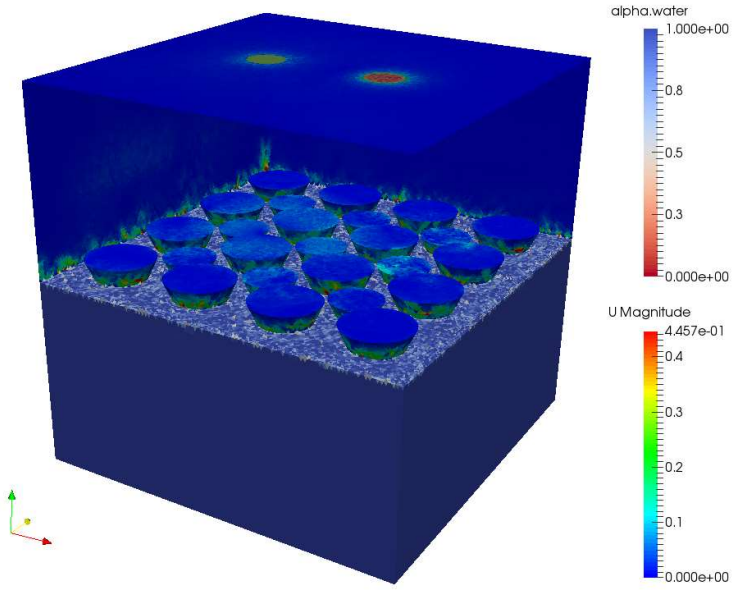

Figure 6.58. Configuration 2 fuel tank with Medium and Large inverted cones – 25 Cones.

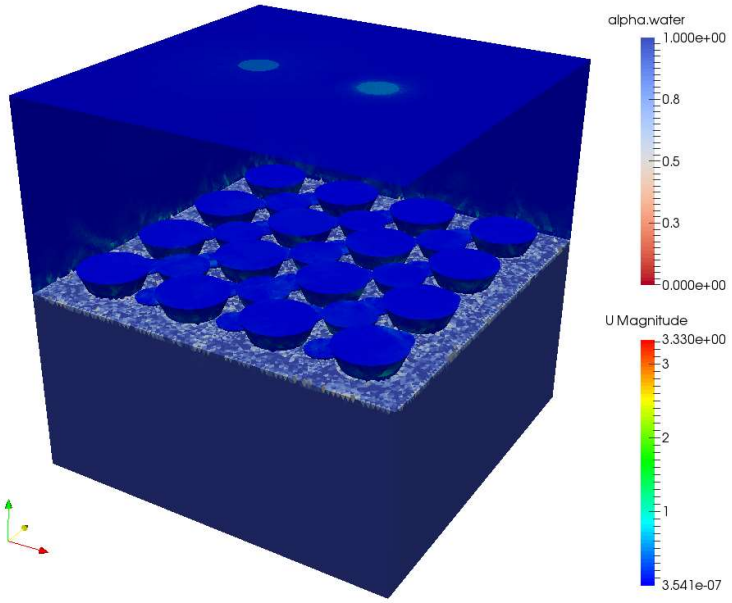

Figure 6.59. Configuration 2 fuel tank with Small, Medium, and Large inverted cones – 49 Cones.

The exposed surface area for each configuration is listed in Table 6.6, where dz/L = 0.0 corresponds to the water surface. Note that the exposed surface area for 25 Cones and 49 Cones is the same at the distances of interests because the top of the Small Inverted Cones is below dz/L = 0.01. The exposed surface area for all configurations at dz/L = 0.08 is 0.25 m^2. The smallest gap between floating objects is listed in Table 6.7.

Table 6.6. Exposed Surface Area (m^2)

	dz/L = 0.0	**dz/L = 0.01**	**dz/L = 0.02**	**dz/L = 0.05**
Without Objects	0.25	0.25	0.25	0.25
16 Rectangles	0.1476	0.1476	0.1476	0.1476
16 Cones	0.192490	0.184566	0.176131	0.147760
25 Cones	0.174293	0.162990	0.150890	0.147760
49 Cones	0.139691	0.162990	0.150890	0.147760

Table 6.7. Smallest gap between floating objects

Array	d (meter)
16 Rectangles	0.040
16 Cones	0.0298
25 Cones	0.008747
49 Cones	0.002498

6.4.1 *Volume Flow Rate and Mass Flow Rate*

The average volume flow rate and average mass flow rate as a function of Reynolds number at various distances above the fluid surface is shown in Figure 6.60 to Figure 6.67. The volume flow rate of water vapor normalized by the volume flow rate of the inlet are shown in Figure 6.68 to Figure 6.71. Distances dz/L = 0.01 and 0.02 correspond to measurements taken between floating objects, dz/L = 0.05 is flush with the top of the largest floating object, and dz/L = 0.08 is above all floating objects.

As expected, based on the experimental results [4], the volume flow rate for the tank without objects increases as the inlet speed increases. The velocity vector plot through a slice down the center of the tank (Figure 6.72) shows the air flow forming a vortex around the inlet jet when it hits the water surface. As the inlet speed increases, more air carrying water vapor is sucked into the outlet to maintain constant pressure. Similar to Configuration 1, air flow from the inlet jet is not dominated by buoyancy effects due to the smaller Richardson number at higher inlet speeds (see Table 6.5). Convective flow in the liquid layer is observed only in the left half of the fuel tank without objects with a counterclockwise rotation in the same direction as the air flow from the inlet jet as it hits the water surface, and therefore it not a contributing factor to the volume flow rate (see Appendix B for additional flow visualizations). The volume flow rate at various distances above the water surface for the tank without objects can be modeled by the power equations:

$$\dot{V}_{water} = 0.067\mathrm{Re}^{0.0004} \quad (6.11)$$

$$\dot{V}_{water} = 0.0598\mathrm{Re}^{0.0077} \quad (6.12)$$

$$\dot{V}_{water} = 0.0221\mathrm{Re}^{0.0743} \quad (6.13)$$

$$\dot{V}_{water} = 0.0051\mathrm{Re}^{0.2192}\,, \quad (6.14)$$

where Re is the Reynolds number of the inlet and the equations correspond to dz/L = 0.01, 0.02, 0.05, and 0.08 respectively.

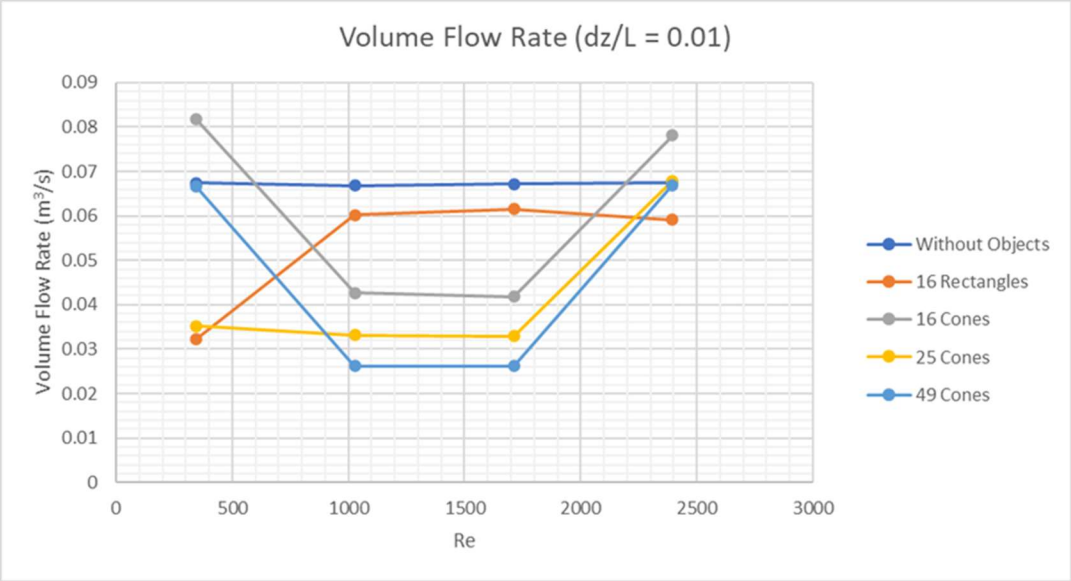

Figure 6.60. Volume flow rate at dz/L = 0.01.

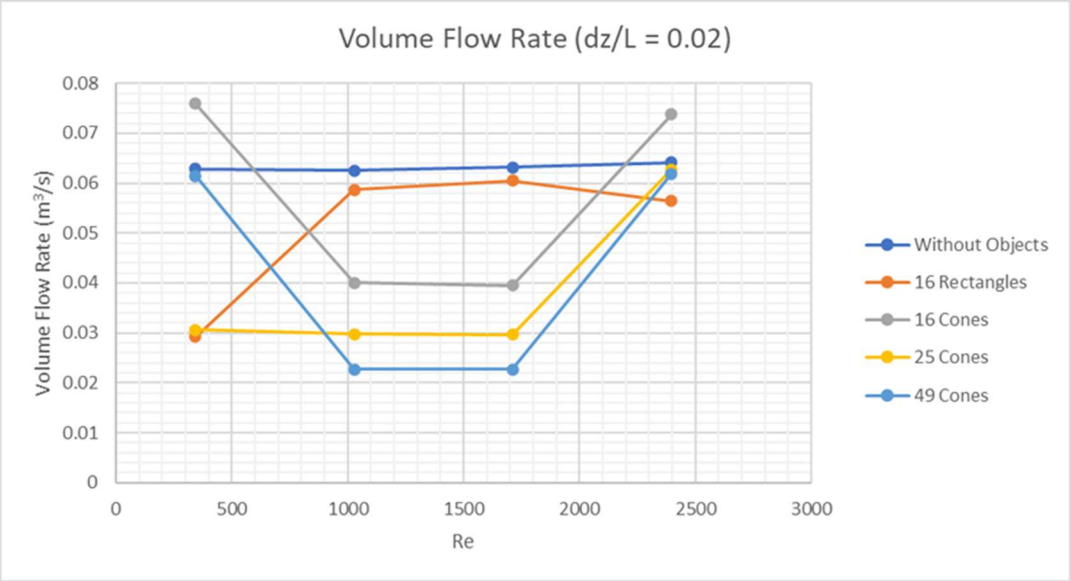

Figure 6.61. Volume flow rate at dz/L = 0.02.

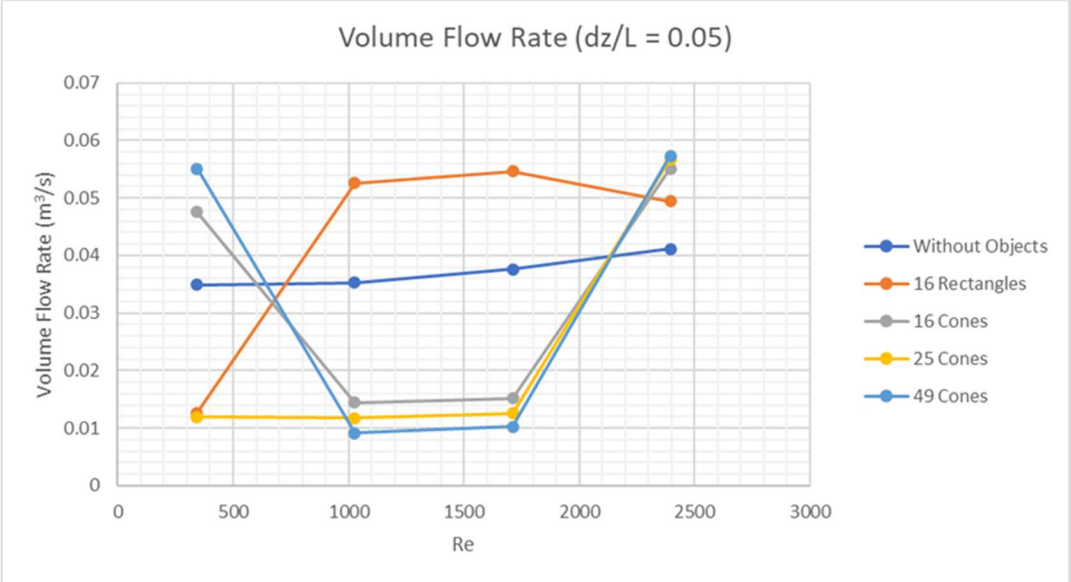

Figure 6.62. Volume flow rate at dz/L = 0.05.

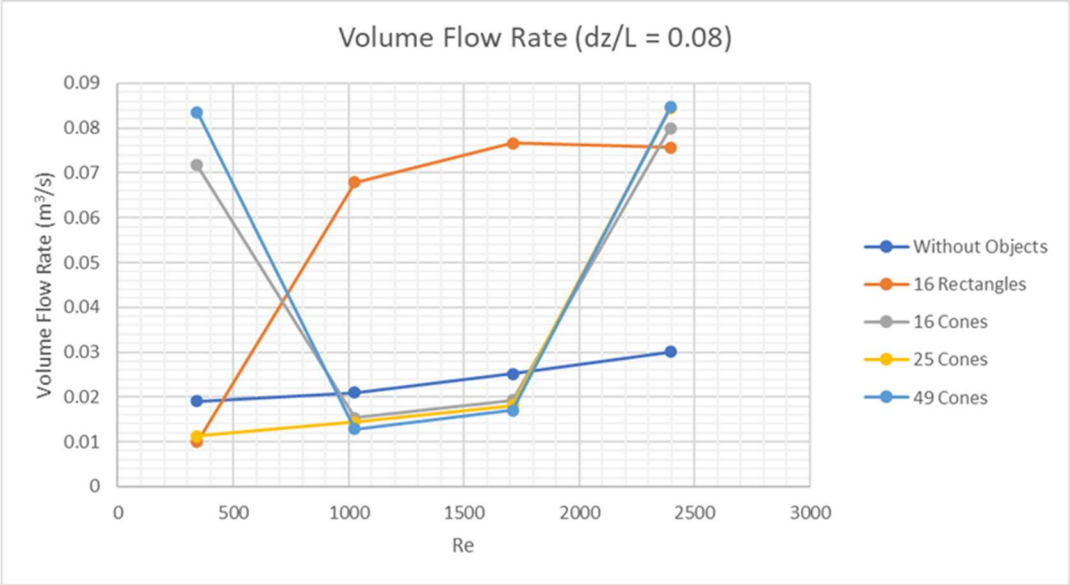

Figure 6.63. Volume flow rate at dz/L = 0.08.

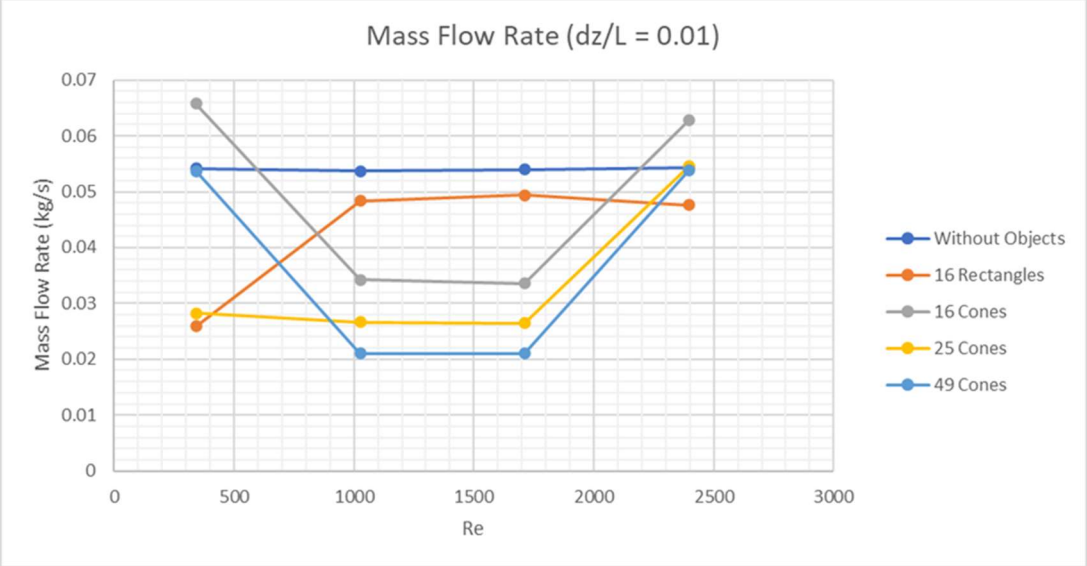

Figure 6.64. Mass flow rate at dz/L = 0.01.

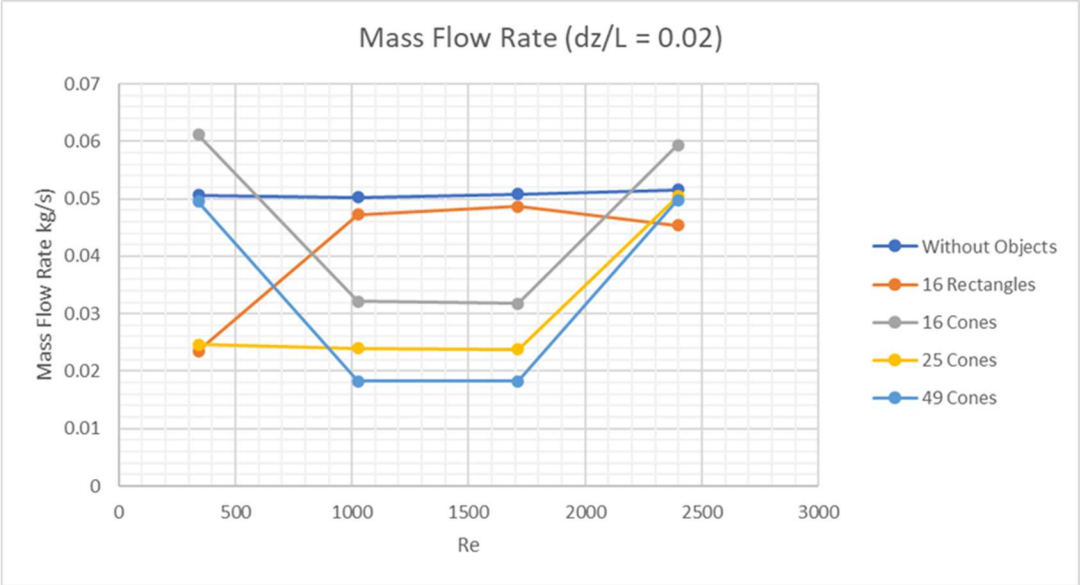

Figure 6.65. Mass flow rate at dz/L = 0.02.

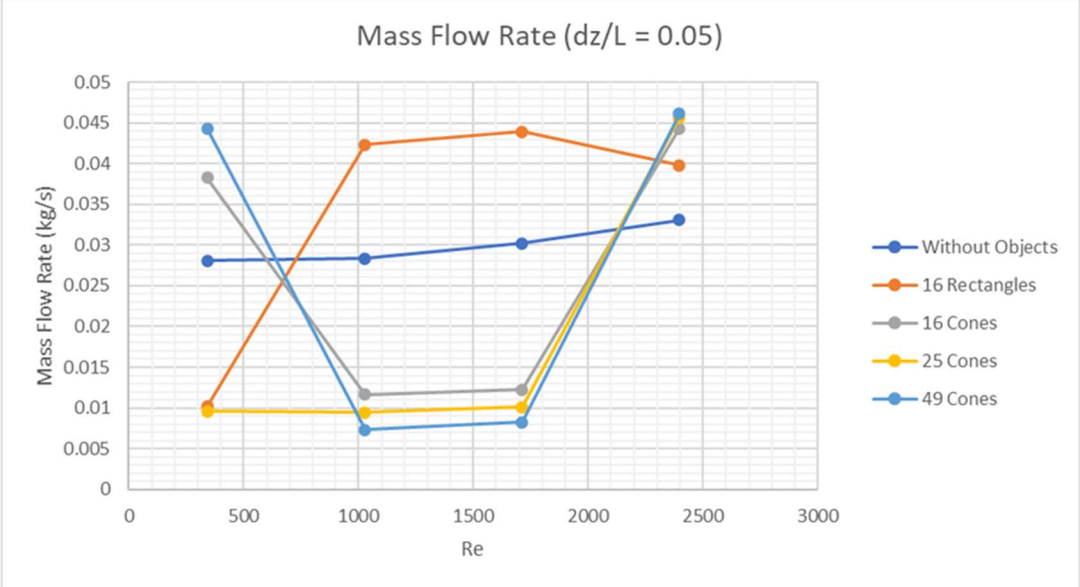

Figure 6.66. Mass flow rate at dz/L = 0.05.

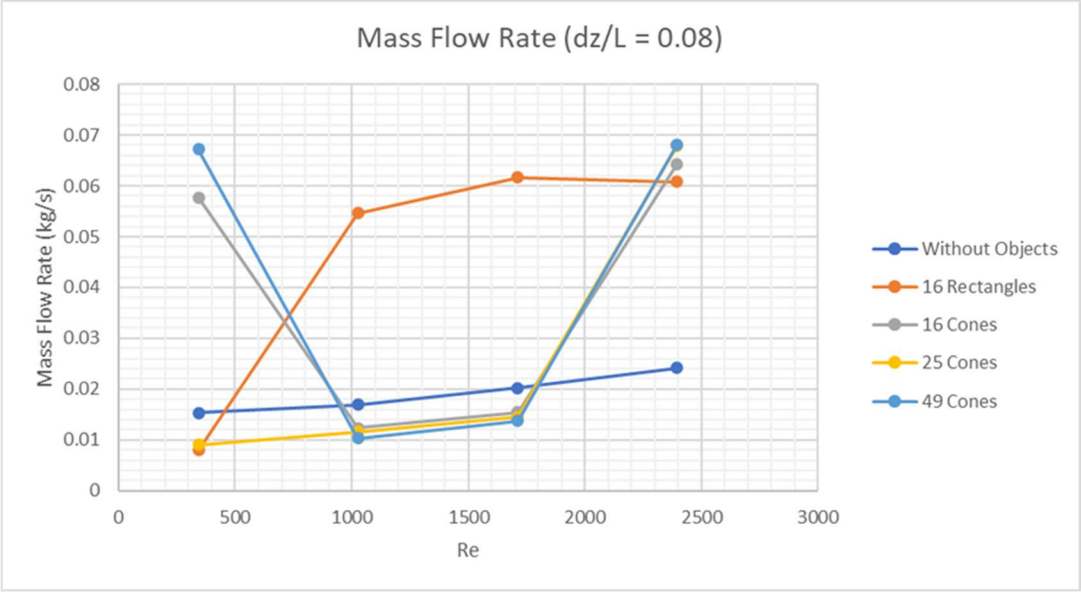

Figure 6.67. Mass flow rate at dz/L = 0.08.

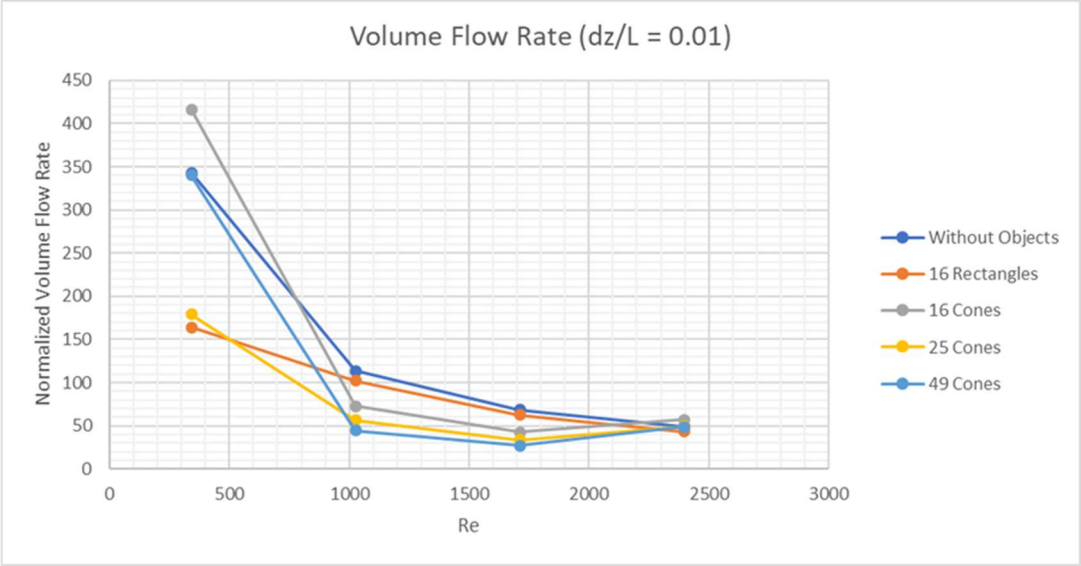

Figure 6.68. Normalized volume flow rate at dz/L = 0.01.

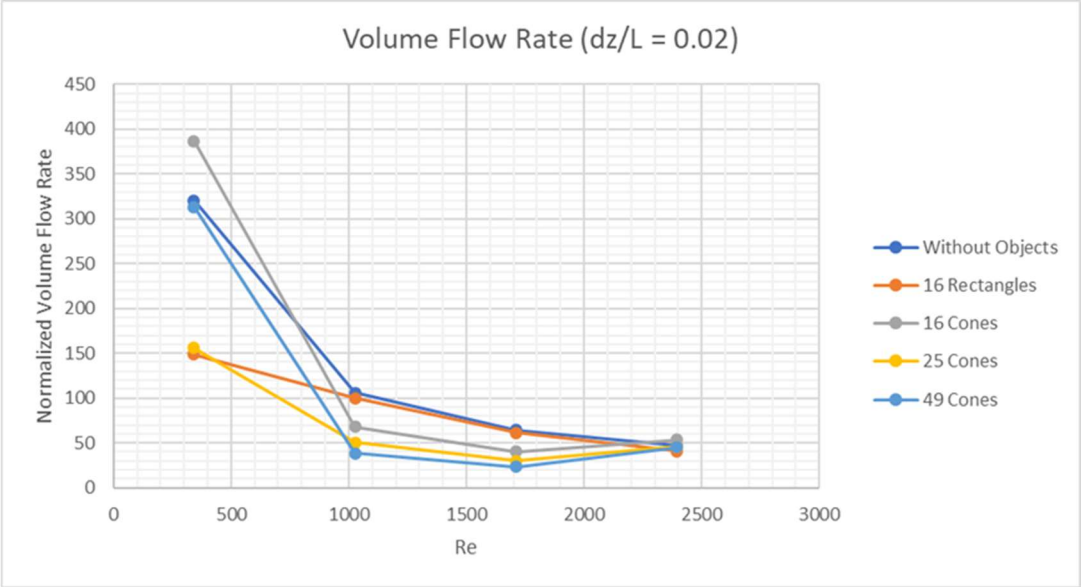

Figure 6.69. Normalized volume flow rate at dz/L = 0.02.

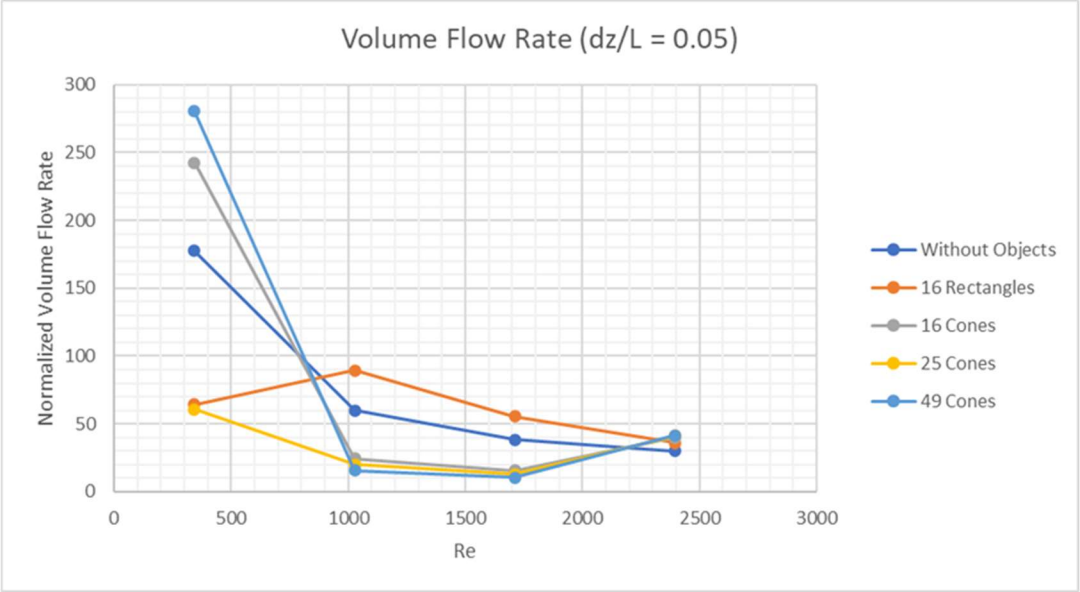

Figure 6.70. Normalized volume flow rate at dz/L = 0.05.

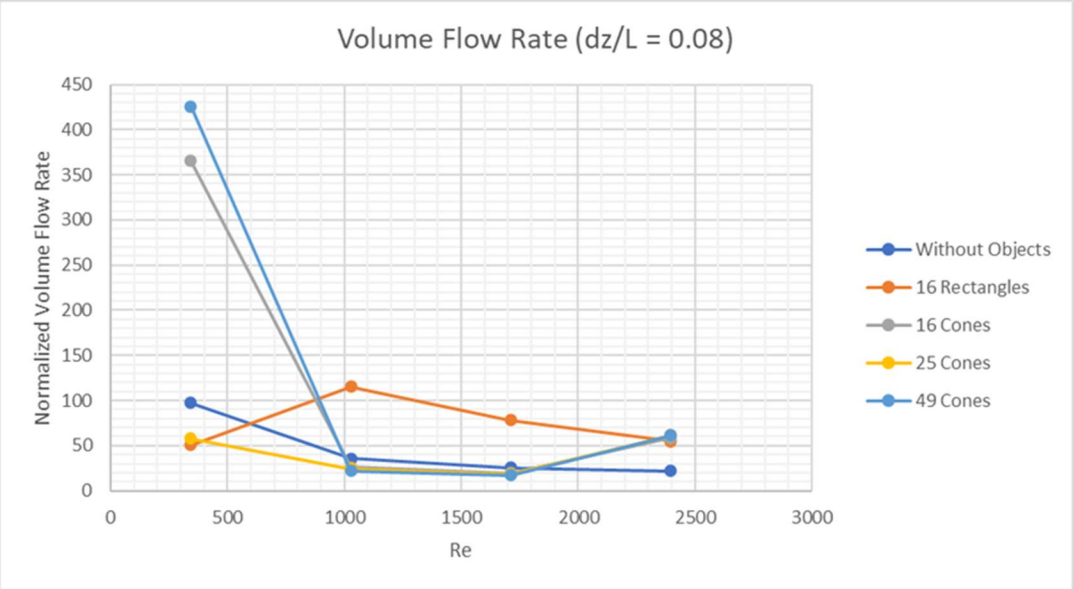

Figure 6.71. Normalized volume flow rate at dz/L = 0.08.

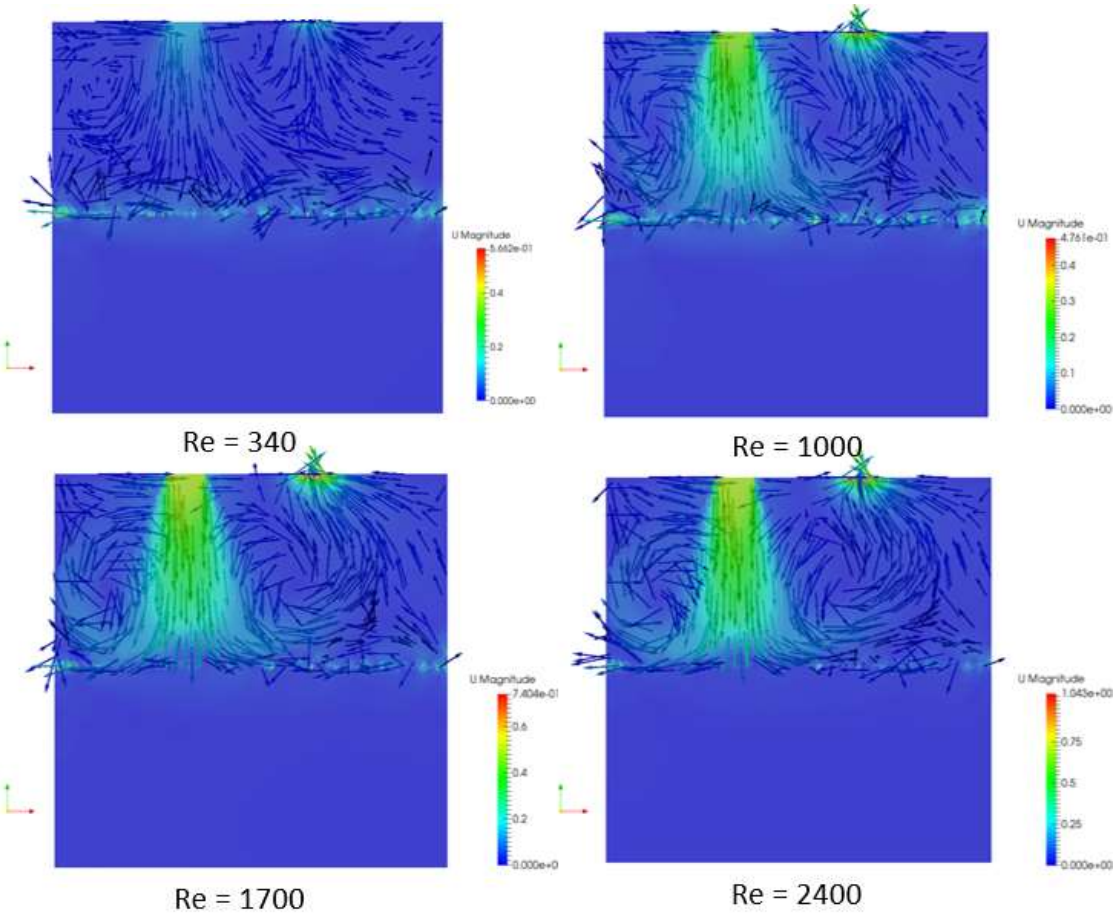

Figure 6.72. Velocity vectors on a slice through the center – Without Objects.

At the lowest inlet speed Re = 340, the volume flow rate for the rectangular blocks is below that of the tank without objects. However, as the inlet speed increases, the volume flow rate increases between the blocks and is even greater than the tank without objects values at dz/L = 0.05. This is likely due to the sharp corners of the rectangular blocks encouraging vortex shedding. A visual study of the streamlines originating below the inlet at the top surface of the blocks (see Figure 6.73) shows that at inlet speeds Re > 340 the air flow skims over the top of the blocks creating smaller eddies before reaching the outlet.

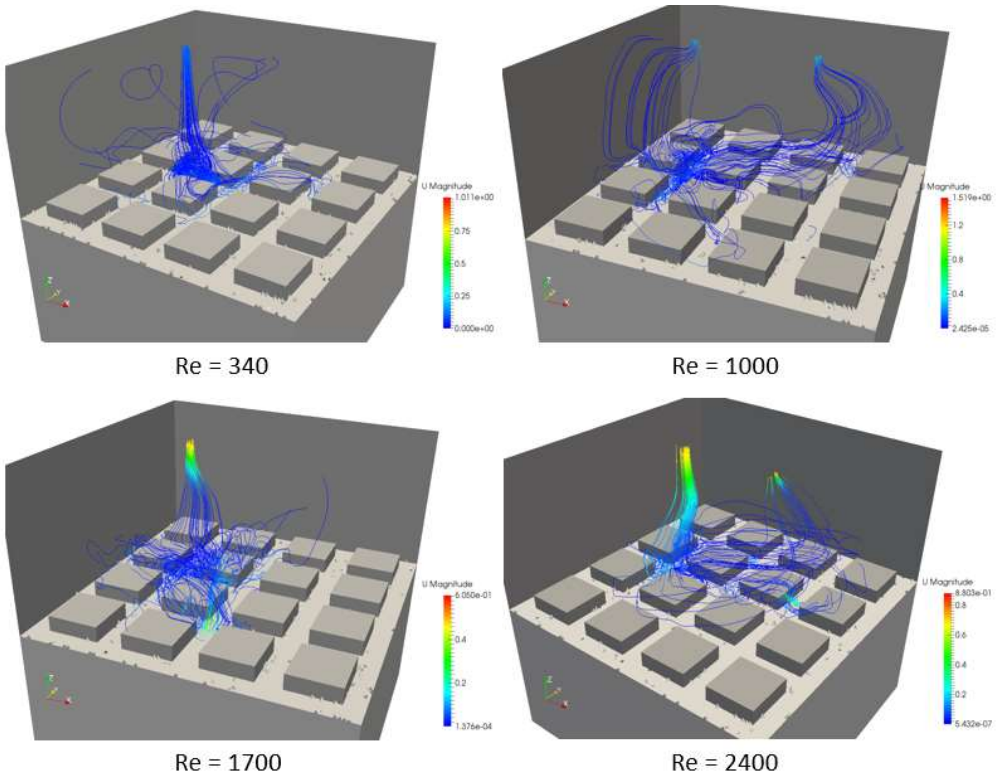

Figure 6.73. Streamlines traced at the top of the rectangular blocks under the inlet (0.167, 0.25, 0.275).

Of the floating objects simulated, the lowest volume flow rates were achieved by the inverted cones only at inlet speed Re = 1000 and 1700, with 49 Cones having the lowest values. Less

exposed surface area and higher density of cones are likely contributing factors. At Re = 340 the value is near or above the fuel tank without objects for 16 Cones and 49 Cones. Surprisingly the volume flow rate jumps at Re = 2400 to match or exceed the volume flow rate of the fuel tank without objects.

A visual study of the streamlines traced directly under the inlet at the height of the Large cone indicates that for inlet speed Re = 1000 and 1700 the air flow is straight from the inlet to the top of the cones, see Figure 6.74 to Figure 6.76. Unlike the case with the rectangular blocks, the inverted cones do not encourage vortex shedding and prevents small eddies from forming. The inlet jet for Re = 340 is angled at the top of the tank indicating that circulation inside the fuel tank is affecting the inlet jet.

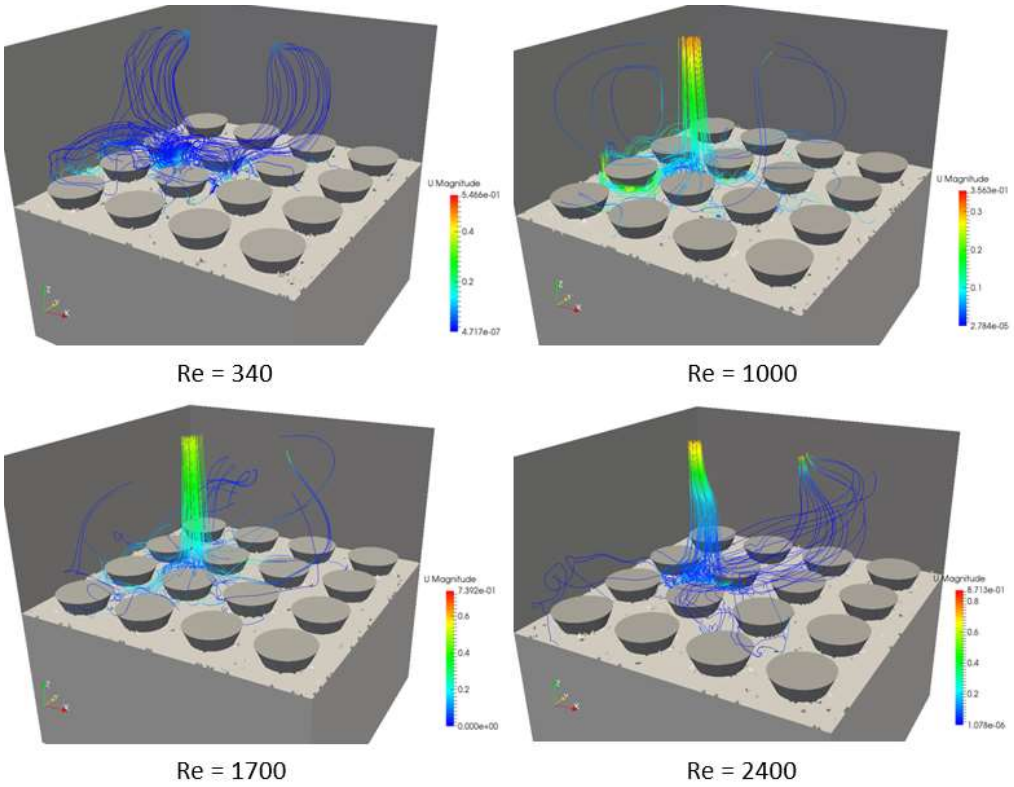

Figure 6.74. Streamlines traced under the inlet for 16 Cones (0.167, 0.25, 0.275).

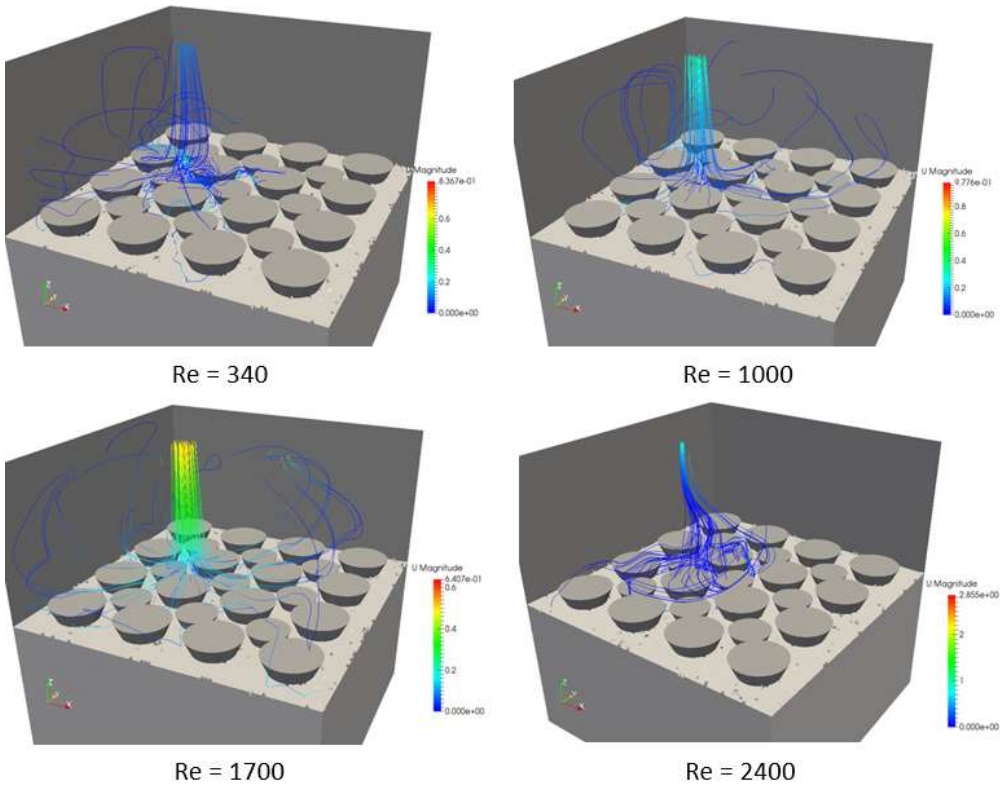

Figure 6.75. Streamlines traced under the inlet for 25 Cones (0.167, 0.25, 0.275).

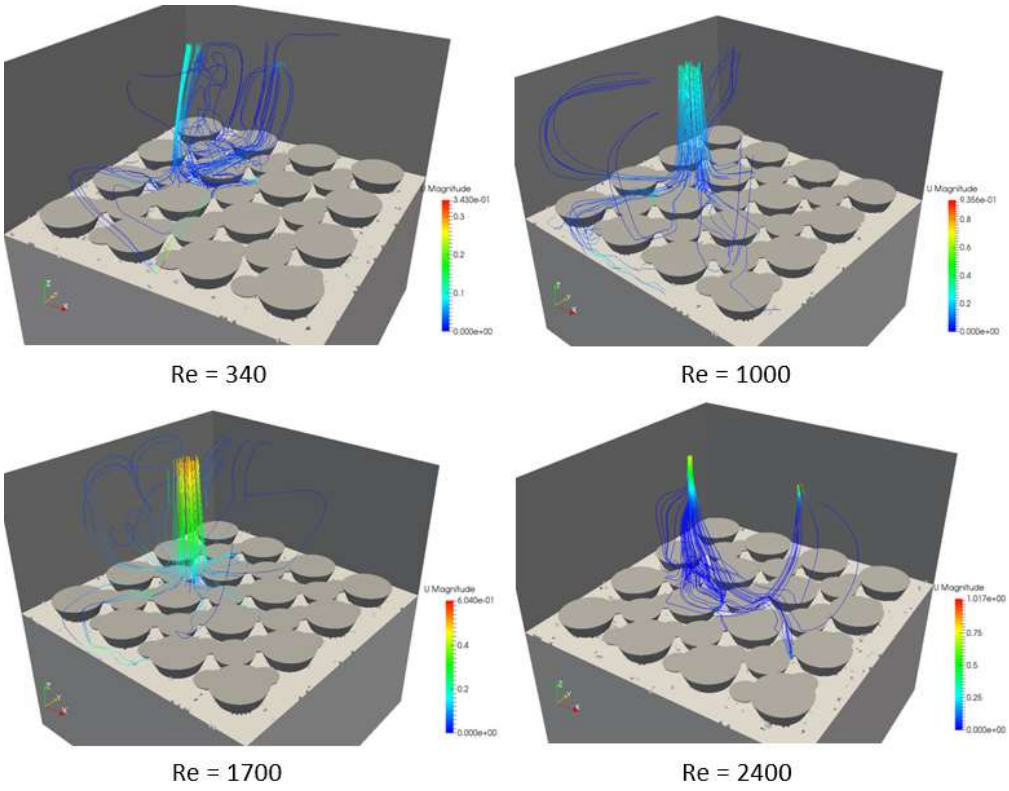

Figure 6.76. Streamlines traced under the inlet for 49 Cones (0.167, 0.25, 0.275).

The angled inlet jet for Re = 340 can be seen more clearly in vector plots through a slice in the center of the fuel tank (Figure 6.77 to Figure 6.79). The inlet air flow passes along the water surface then exits through the outlet. As shown in the streamline plots, the air flow slows and forms small eddies near the water surface which increase the volume flow rate. However, with 25 Cones the inlet jet appears to be straight, similar to that for inlet speed Re = 1000 and 1700. The cause is unclear, but it follows that the volume flow rate for Re = 340 is similar to Re = 1000 and 1700.

For Re = 1000 and 1700, a portion of the air flow recirculates into the downward inlet jet flow after passing over the top of the floating objects while the remainder stays between the floating objects. For all configurations of floating objects, the inlet jet for Re = 2400 is visibly affected by suction from the outlet needed to maintain constant pressure. This creates a direct path for air flow from the inlet to the outlet similar to inlet speed Re = 340.

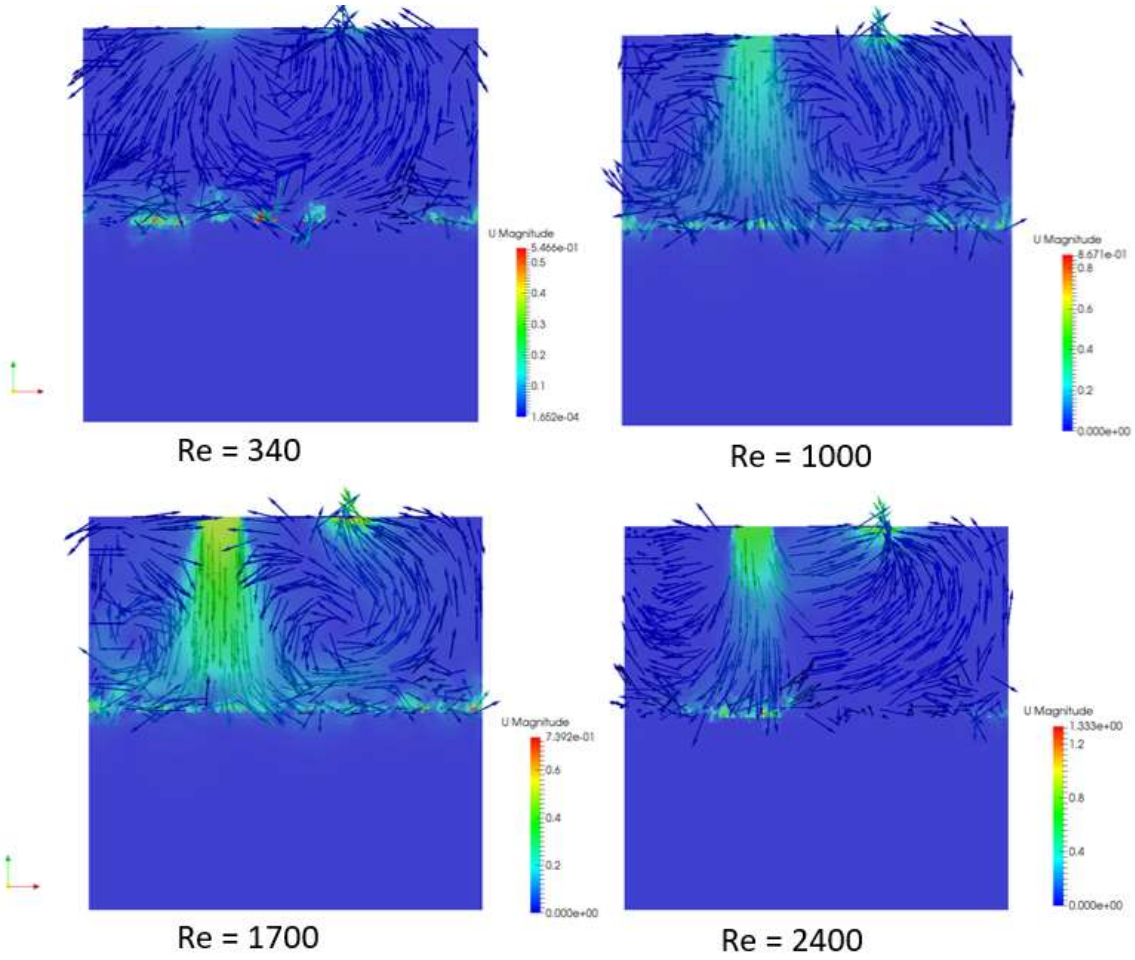

Figure 6.77. Velocity vectors of a slice through the center – 16 Cones.

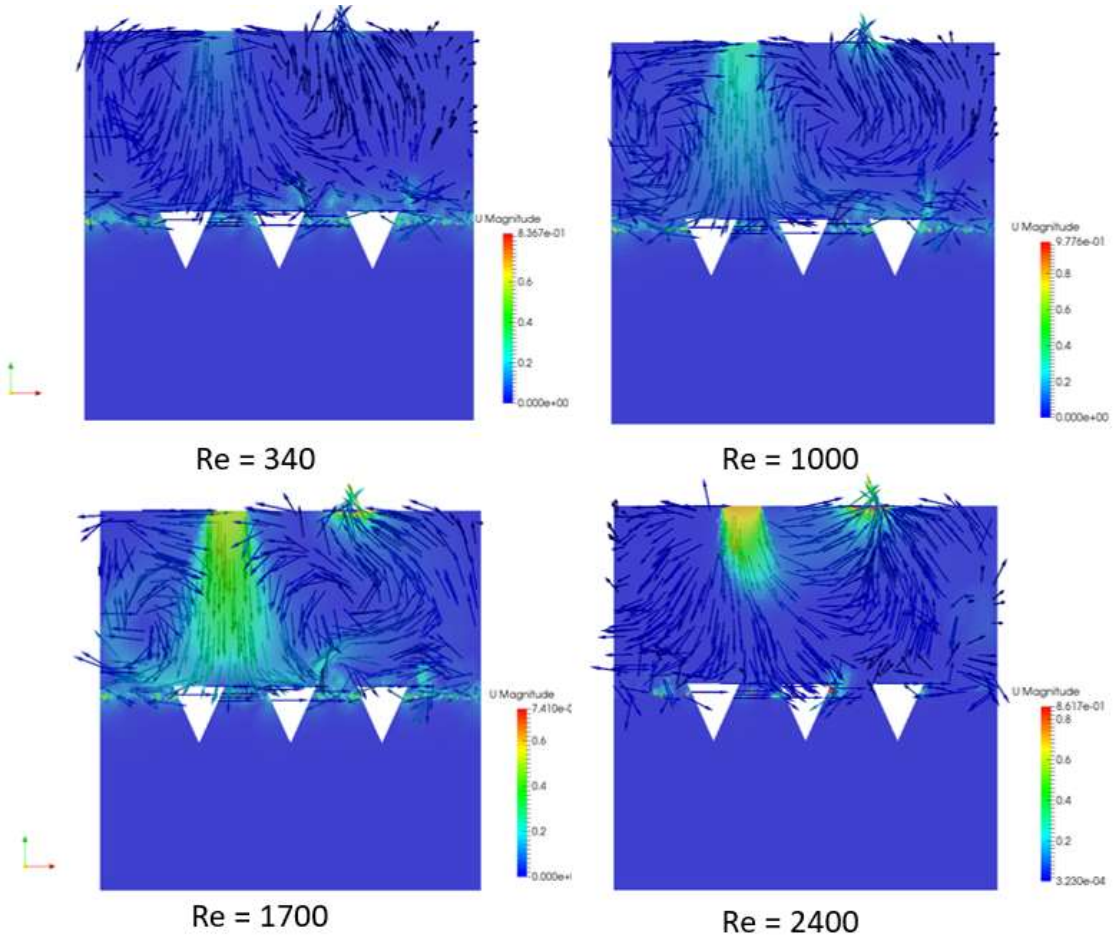

Figure 6.78. Velocity vectors of a slice through the center – 25 Cones.

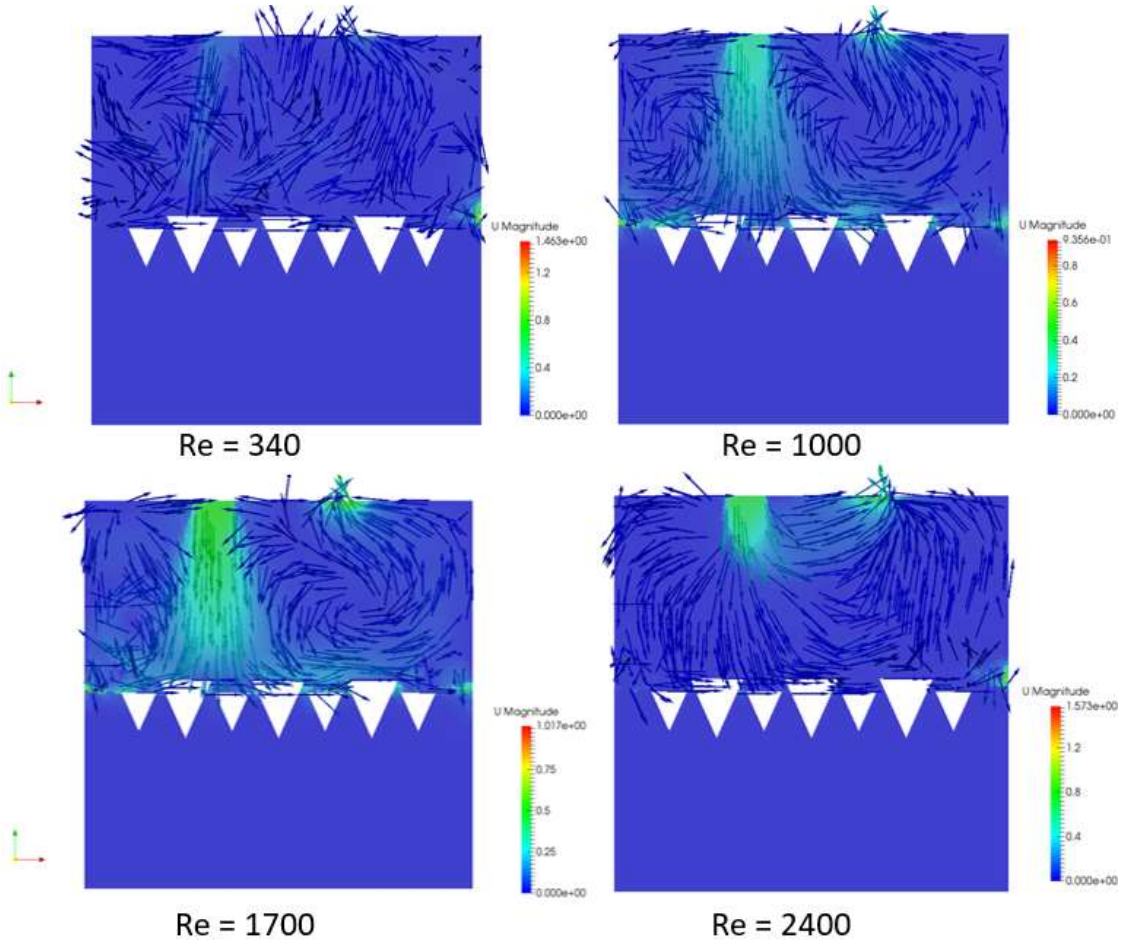

Figure 6.79. Velocity vectors of a slice through the center – 49 Cones.

The effect of the floating objects has on the volume flow rate as a function of height above the water surface is shown in Figure 6.80 to Figure 6.84. In the Configuration 2 fuel tank without objects, the volume flow rate decreases farther away from the water surface, similar to Configuration 1. However, the rectangular blocks increase the volume flow rate above the top of the objects (dz/L = 0.08) for inlet speeds Re > 340. The inverted cones consistently lower the volume flow rate for Re = 1000 and 1700 when compared to the tank without objects; with a local minimum at the top of the largest floating objects (dz/L = 0.05).

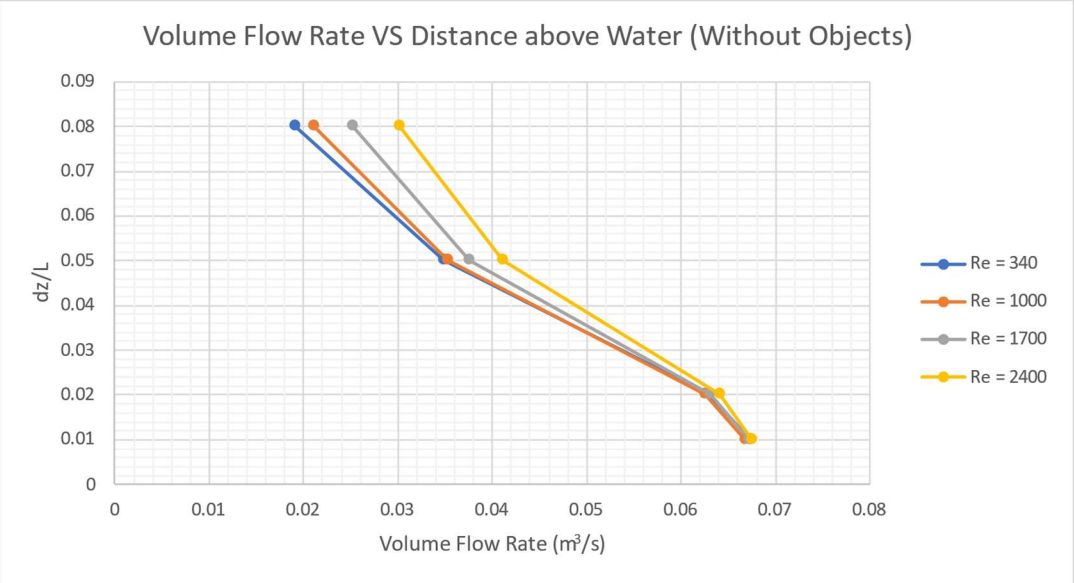

Figure 6.80. Volume flow rate vs dz/L – Without Objects.

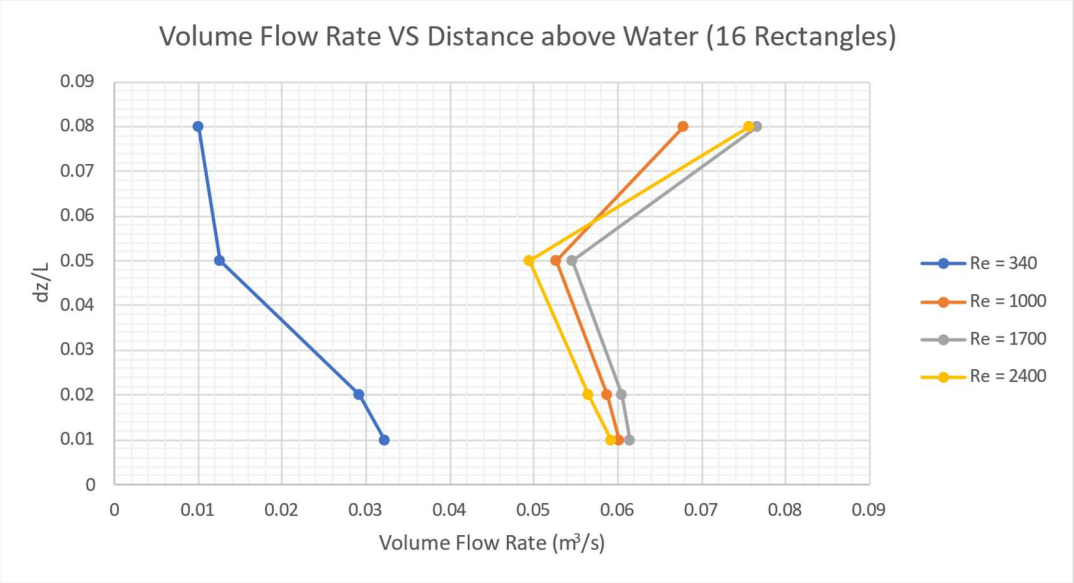

Figure 6.81. Volume flow rate vs dz/L – 16 Rectangles.

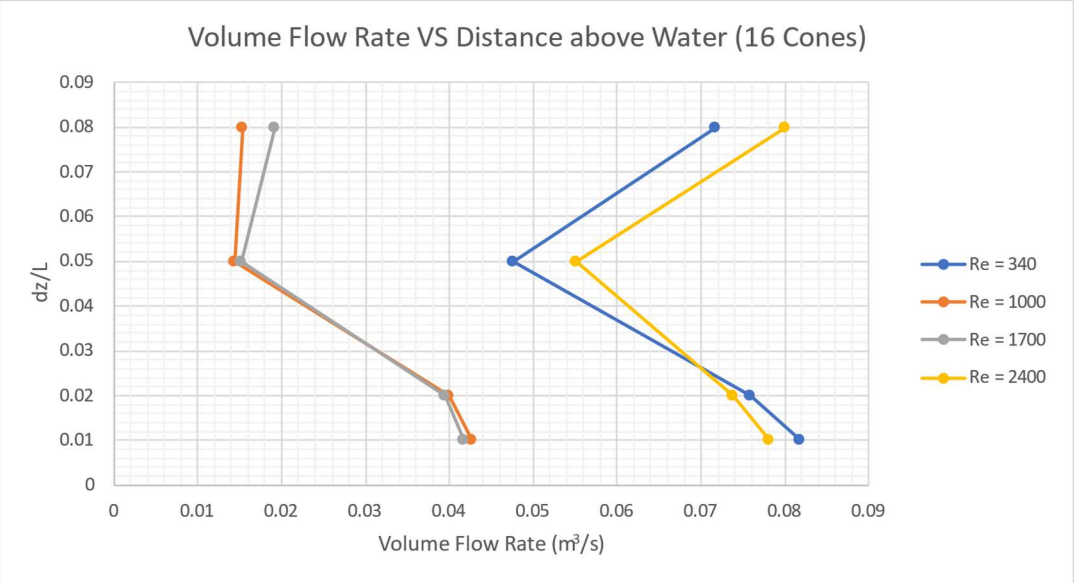

Figure 6.82. Volume flow rate vs dz/L – 16 Cones.

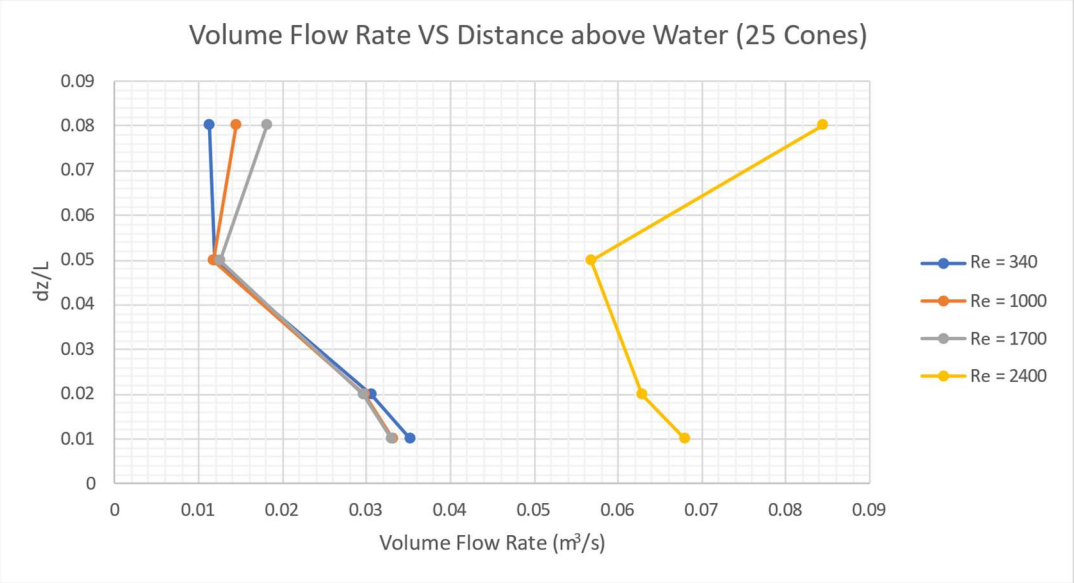

Figure 6.83. Volume flow rate vs dz/L – 25 Cones.

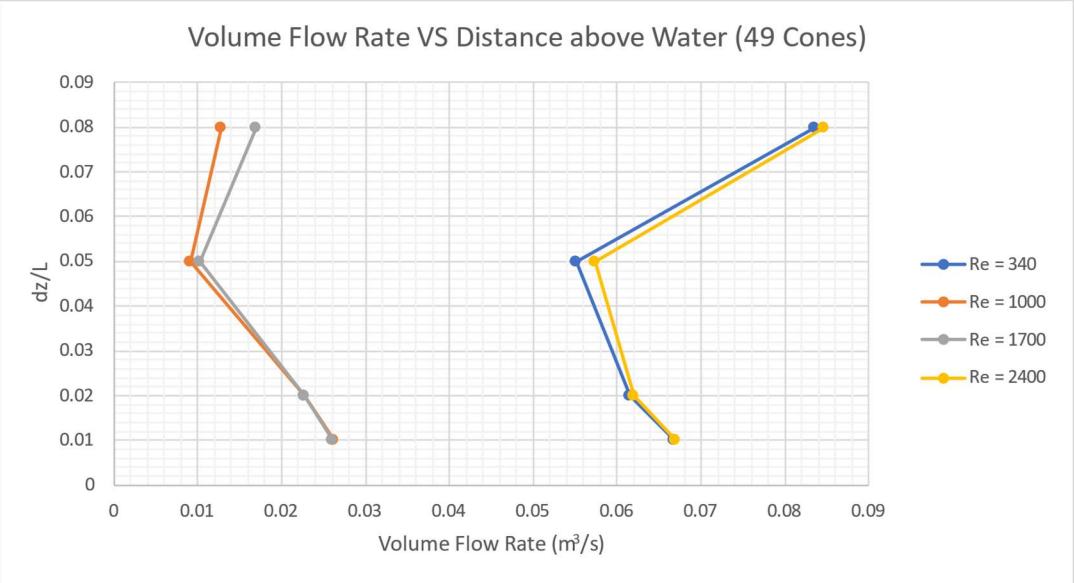

Figure 6.84. Volume flow rate vs dz/L – 49 Cones.

The inverted cones were the most effective at reducing the volume flow rate. The ratio of volume flow rate of the fuel tank floating objects to the fuel tank without objects (shown in Figure 6.85 to Figure 6.88) shows that the volume flow rate is reduced about 40 – 60% using multiple sized cones at inlet speeds Re = 1000 and 1700 at all distances above the water. However, the rectangular blocks increased the volume flow rate measured above the water surface at dz/L = 0.05 and 0.08 by about 40 – 200% for the same inlet speeds.

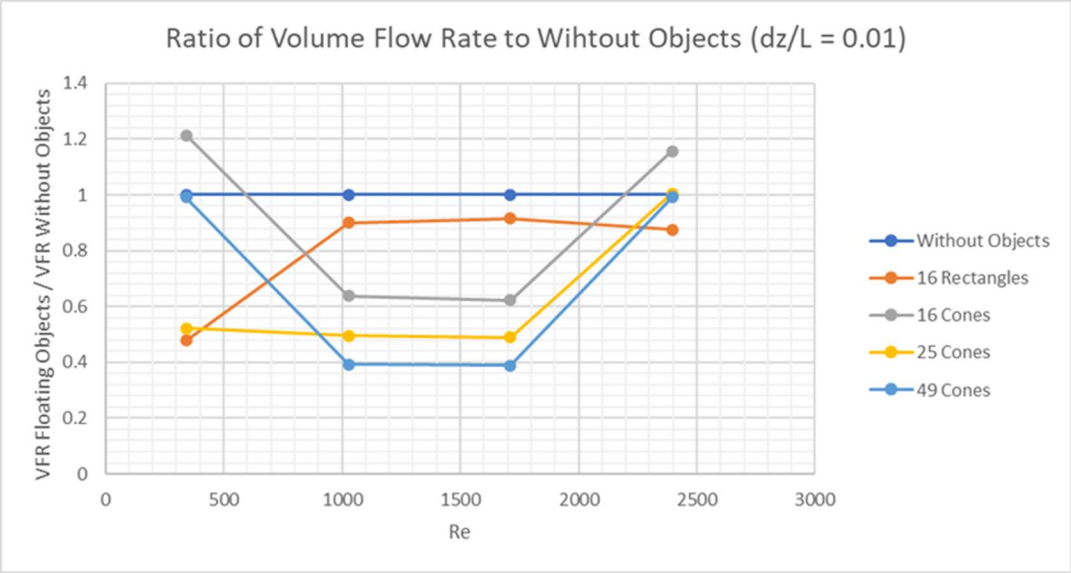

Figure 6.85. Ratio of Volume Flow Rate of floating objects to Volume Flow Rate of the fuel tank without objects, at dz/L = 0.01.

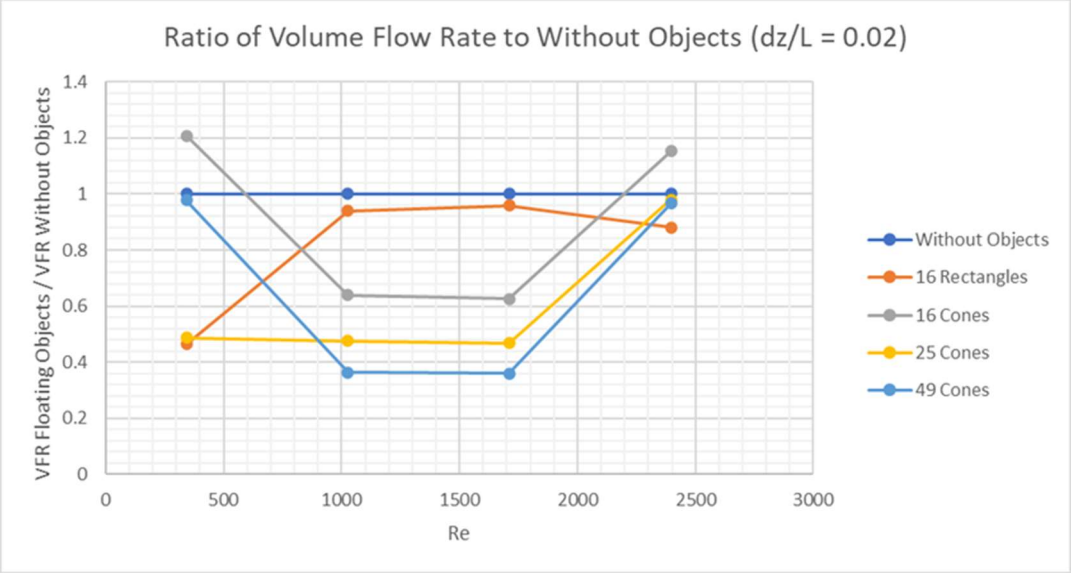

Figure 6.86. Ratio of Volume Flow Rate of floating objects to Volume Flow Rate of the fuel tank without objects, at dz/L = 0.02.

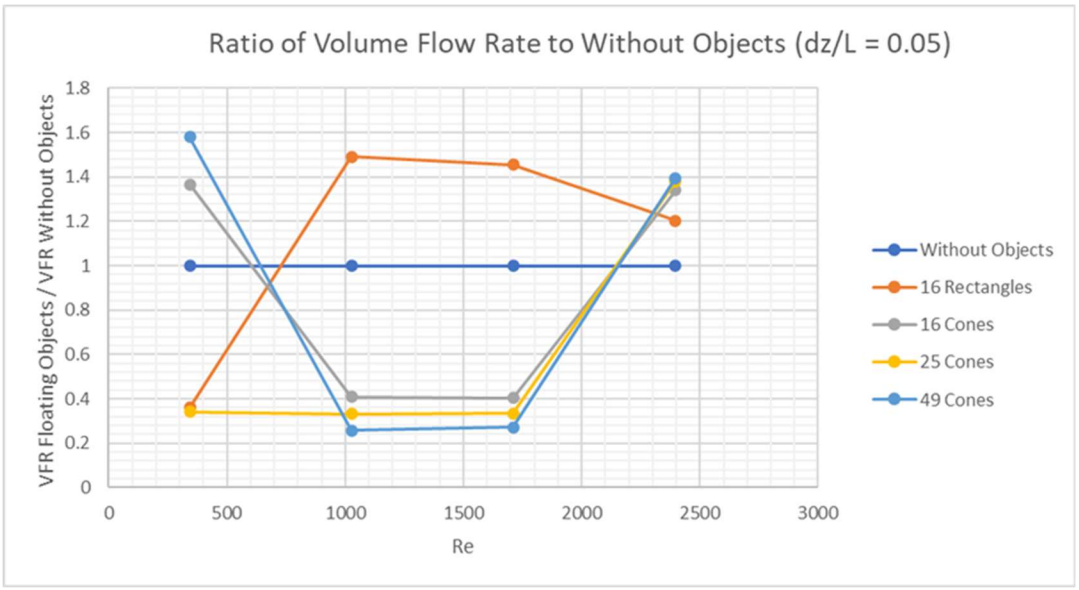

Figure 6.87. Ratio of Volume Flow Rate of floating objects to Volume Flow Rate of the fuel tank without objects, at dz/L = 0.05.

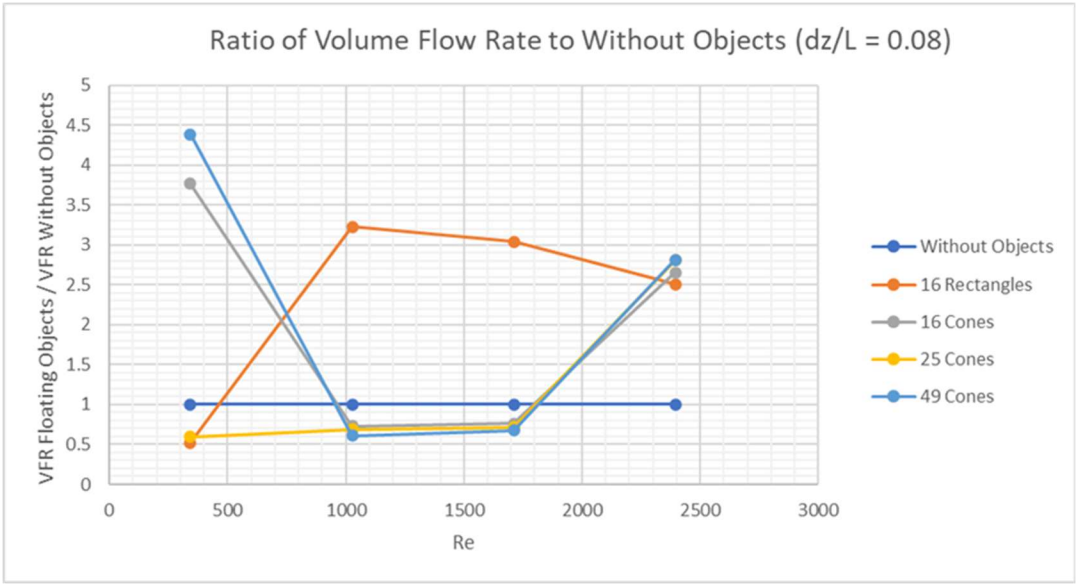

Figure 6.88. Ratio of Volume Flow Rate of floating objects to Volume Flow Rate of the fuel tank without objects, at dz/L = 0.08.

Close up views of the streamlines shows that the concave shape regions between inverted cones were better at trapping air than the rectangular blocks (see Figure 6.89 to Figure 6.96). As shown, eddies are formed as air flows into the gaps between floating objects. The rectangular blocks allow the eddies to propagate above the blocks. The concave shape created between inverted cones is shown to trap the eddies with 16 Cones and 25 Cones as seen in Figure 6.91 to Figure 6.93. In the case of 49 Cones, the smallest size cones appear to prevent eddies from forming due to the no slip condition on the cone surface (see Figure 6.95 and Figure 6.96). Both trapping eddies in concave regions and preventing eddies from forming using a higher density of floating objects resulted lower volume flow rates.

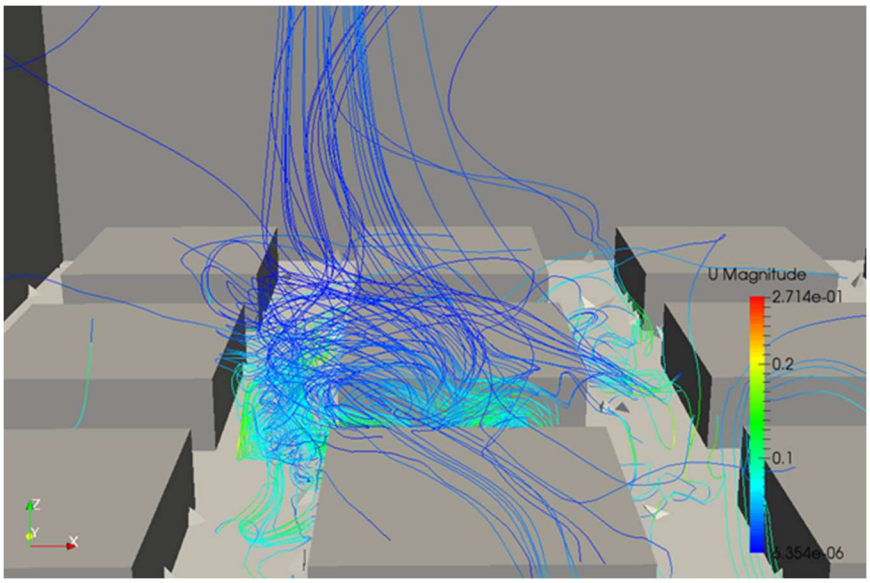

Figure 6.89. Close up of streamlines traced under inlet for 16 Rectangles (0.167, 0.25, 0.275), at Re = 340.

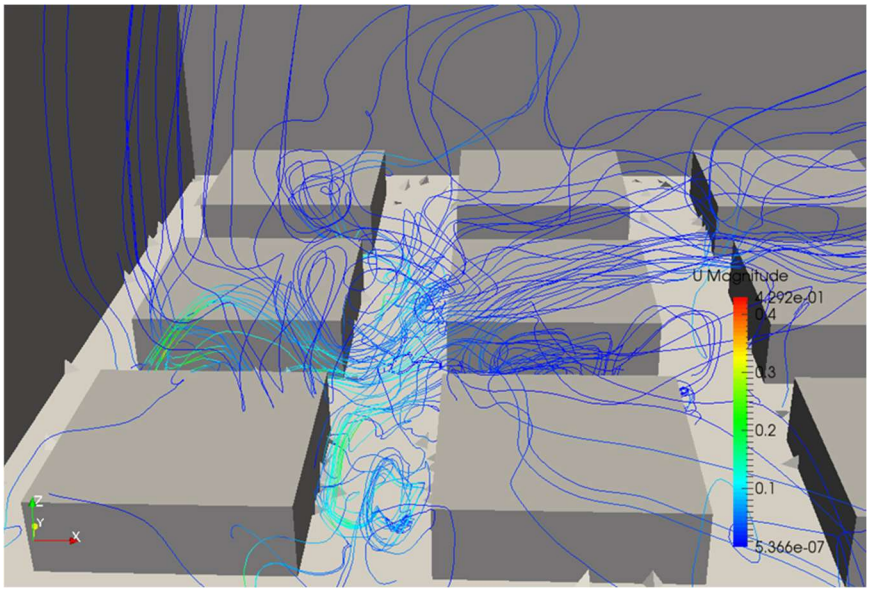

Figure 6.90. Close up of streamlines traced under inlet for 16 Rectangles (0.167, 0.25, 0.275), at Re = 1000.

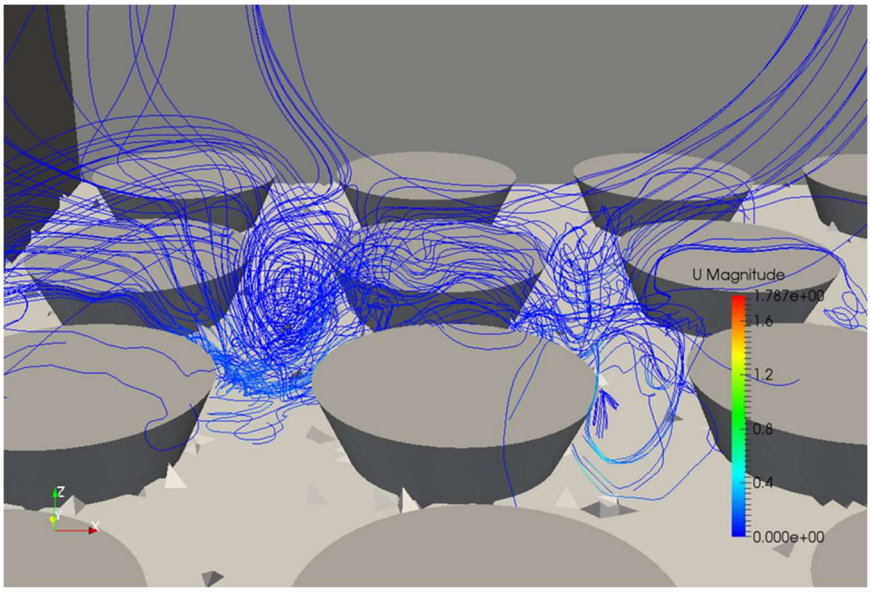

Figure 6.91. Close up of streamlines traced under inlet for 16 Cones (0.167, 0.25, 0.275), at Re = 340.

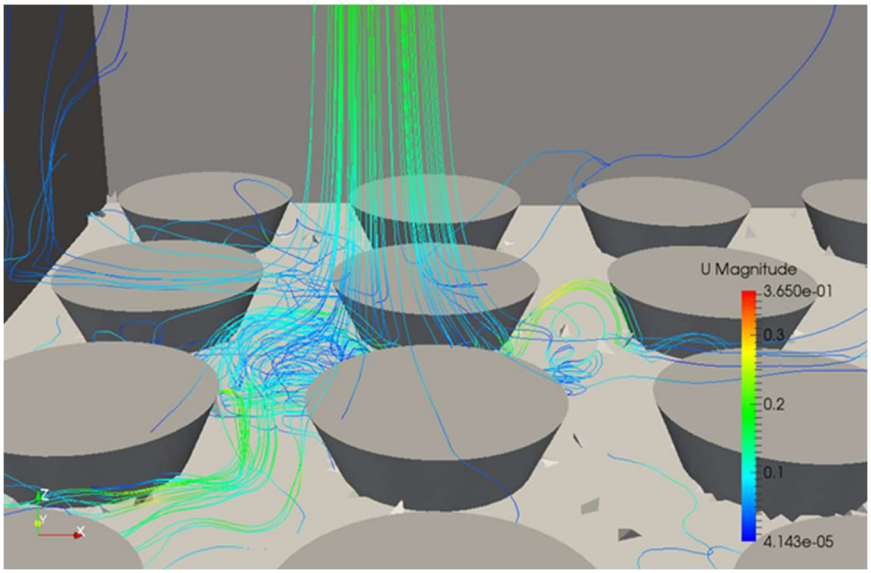

Figure 6.92. Close up of streamlines traced under inlet for 16 Cones (0.167, 0.25, 0.275), at Re = 1000.

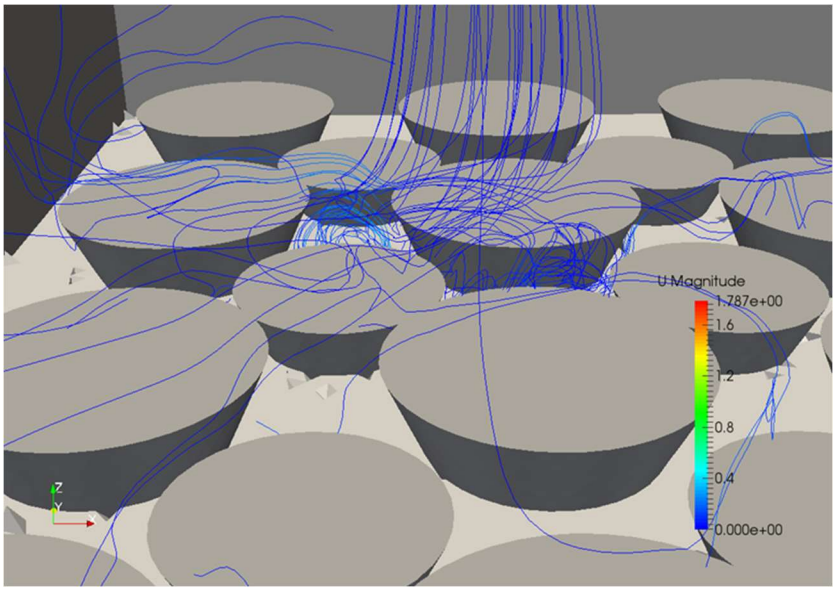

Figure 6.93. Close up of streamlines traced under inlet for 25 Cones (0.167, 0.25, 0.275), at Re = 340.

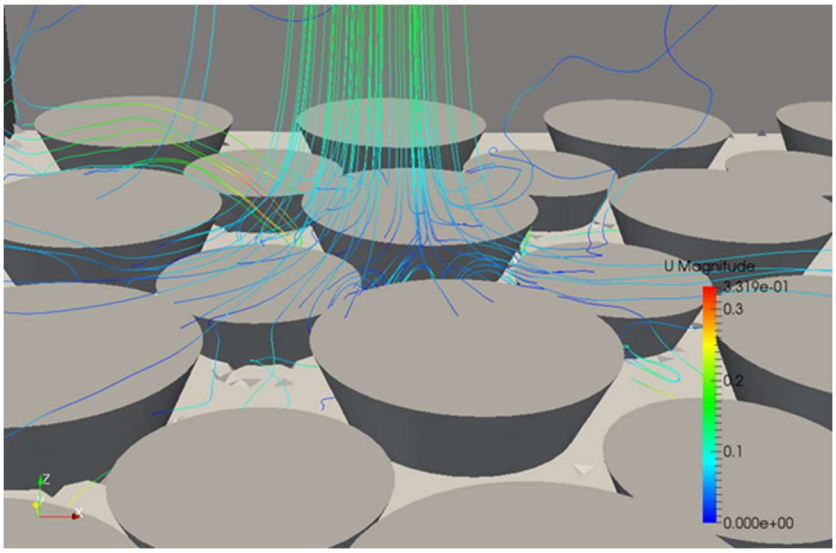

Figure 6.94. Close up of streamlines traced under inlet for 25 Cones (0.167, 0.25, 0.275), at Re = 1000

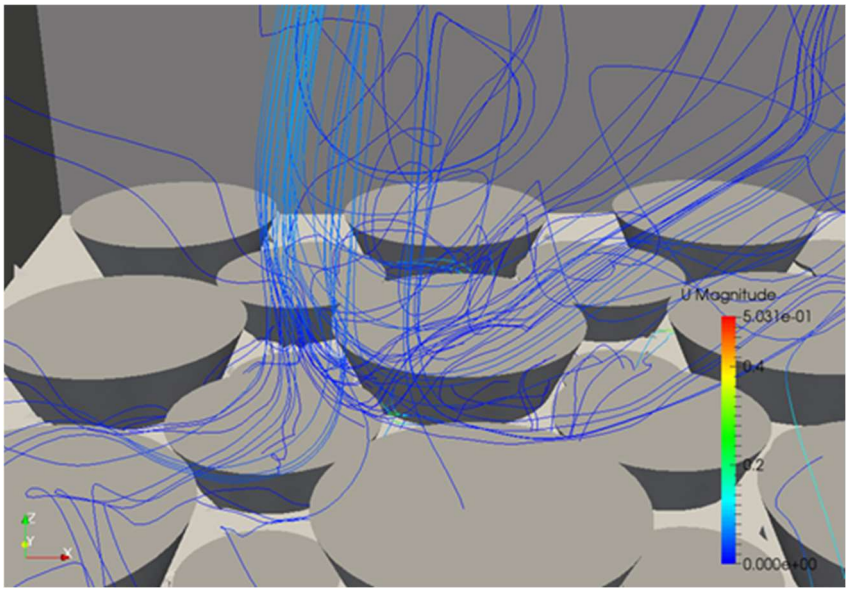

Figure 6.95. Close up of streamlines traced under inlet for 49 Cones (0.167, 0.25, 0.275), at Re = 340.

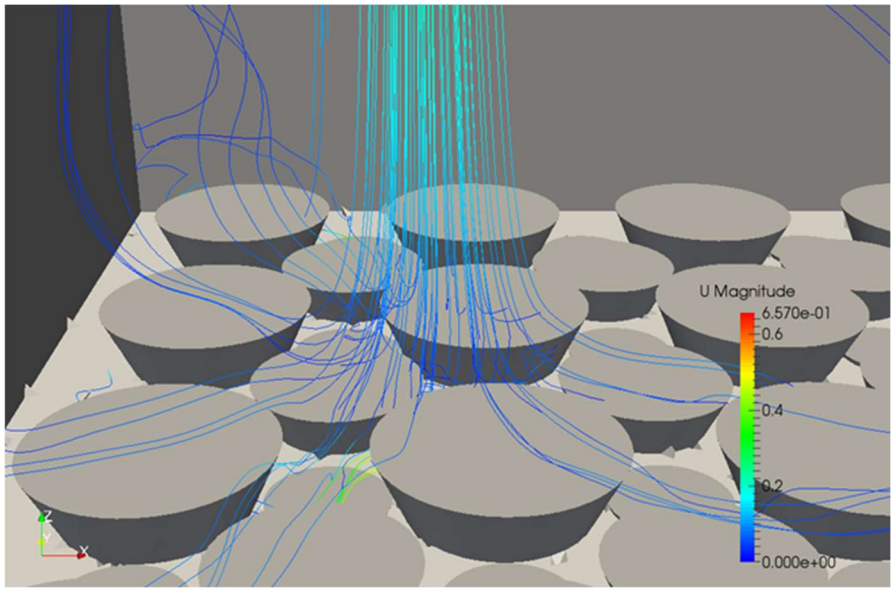

Figure 6.96. Close up of streamlines traced under inlet for 49 Cones (0.167, 0.25, 0.275), at Re = 1000.

6.4.2 *Volume Concentration of Water Vapor*

Similar to Configuration 1, the volume concentration of water vapor decreases linearly for the Configuration 2 fuel tank without objects (see Figure 6.97). The linear fit to data is given by

$$C_{water} = -8e^{-6}\mathrm{Re} + 0.9999 \tag{6.15}$$

$$C_{water} = -9e^{-6}\mathrm{Re} + 0.9997 \tag{6.16}$$

$$C_{water} = -1e^{-5}\mathrm{Re} + 0.9979 \tag{6.17}$$

$$C_{water} = -2e^{-5}\mathrm{Re} + 0.9925\,, \tag{6.18}$$

for dz/L = 0.01, 0.02, 0.05, and 0.08 respectively (see Figure 6.98). The value of water vapor volume concentration for Configuration 2 is consistently lower than Configuration 1. Near the water surface at dz/L = 0.01 and 0.02 for Configuration 2 is in close agreement with a difference of 0.018 – 0.06% compared to Configuration 1. Farther from the water surface at dz/L = 0.05, the

volume concentration for Configuration 2 has a larger difference, 0.225 – 0.614%. At dz/L = 0.08, the difference in volume concentration is 0.396 – 0.791%. Similar to Configuration 1, the concentration of water vapor decreases farther from the water surface as it mixes with dry air as shown in Figure 6.99.

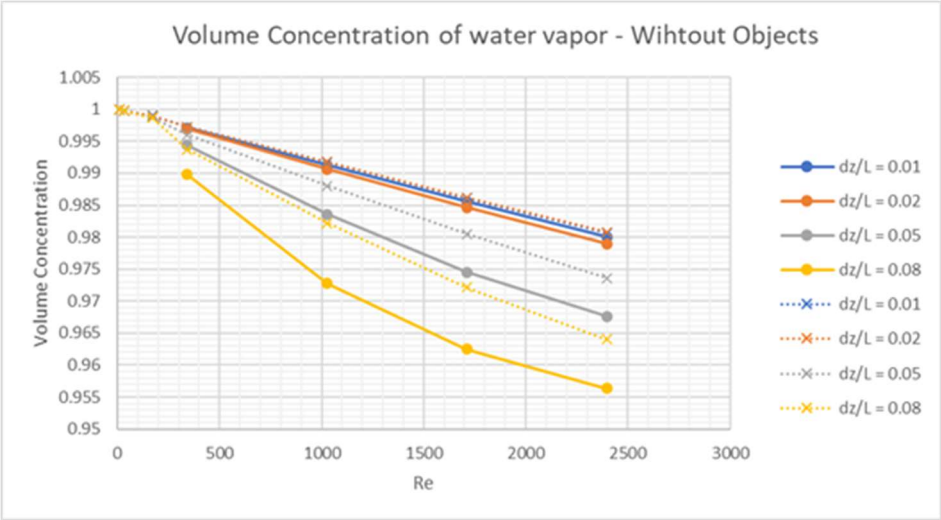

Figure 6.97. Volume concentration of water vapor for fuel tank without objects. Configuration 2 – solid lines, Configuration 1 – dotted lines.

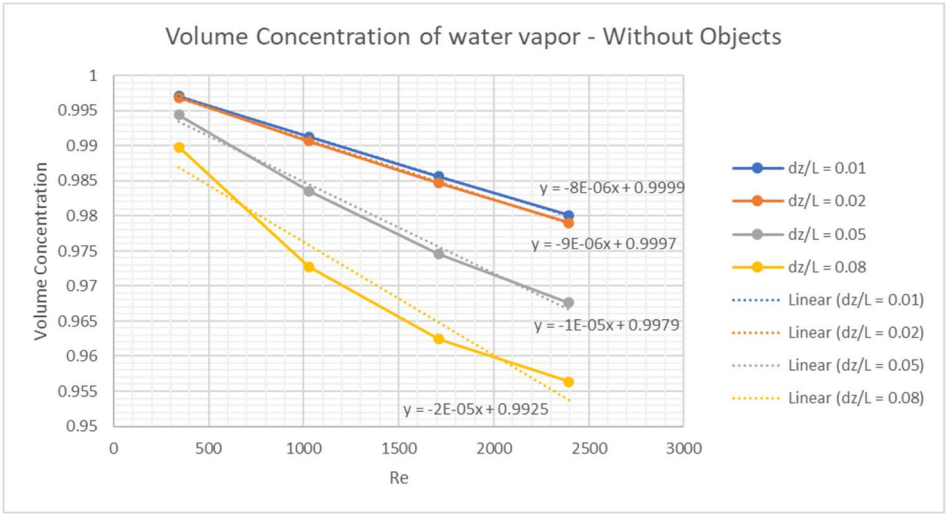

Figure 6.98. Volume concentration of water vapor for Configuration 2 fuel tank without objects (dotted lines are linear trendlines).

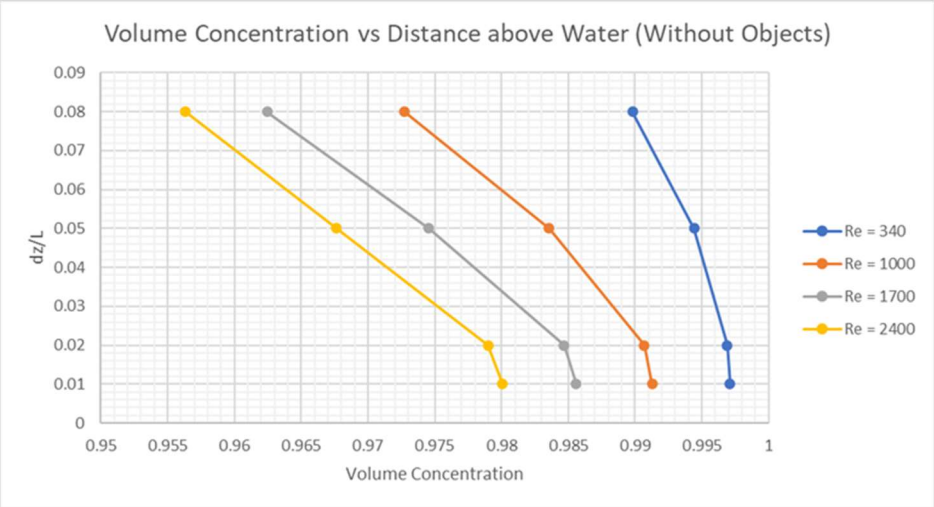

Figure 6.99. Volume concentration of water vapor vs dz/L – Without Objects.

The volume concentration of water vapor for Configuration 2 with floating objects is shown in Figure 6.100 to Figure 6.103 at each height above the water surface. Compared to the tank without objects, the inverted cones decrease the volume concentration of water vapor for inlet speeds Re = 1000 and 1700 and the rectangular blocks increases the concentration at dz/L = 0.05 and 0.08 above the water surface. The lowest volume concentration occurred at inlet speed Re = 1700 for the Configuration 2 fuel tank with 49 Cones. Near the water surface 49 Cones lowers the concentration by 1.3 – 2.6% and above the inverted cones, at dz/L = 0.08, the concentration decreases by 1.7 – 1.8%. At dz/L = 0.05 above the water surface the concentration is 4.5 – 6.4% lower with 49 Cones. This reduction could have a significant impact on reducing the evaporation of kerosene which has a lower flammability limit of 0.6% [14]. In the TWA 800 central fuel tank, evaporation of 1.4% of the fuel was necessary to reach the lower flammability limit [3]. That is a fuel vapor concentration of approximately 0.0053% at the lower flammability limit. Assuming the same volume flow rate for kerosene, the fuel vapor concentration could reduce to 0.00527 – 0.00528% with the use of 49 Cones and an inlet speed Re = 1700 in the TWA 800 central fuel tank.

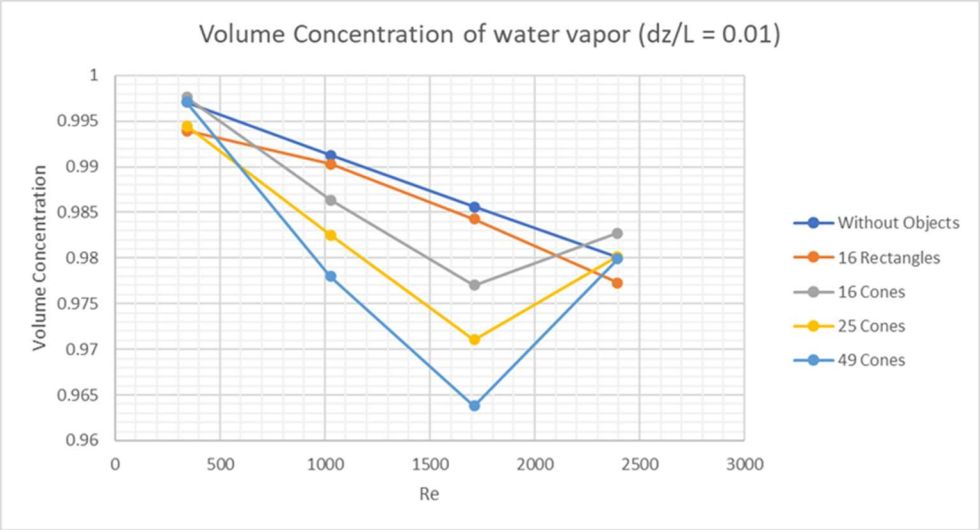

Figure 6.100. Volume concentration of water vapor, at dz/L = 0.01.

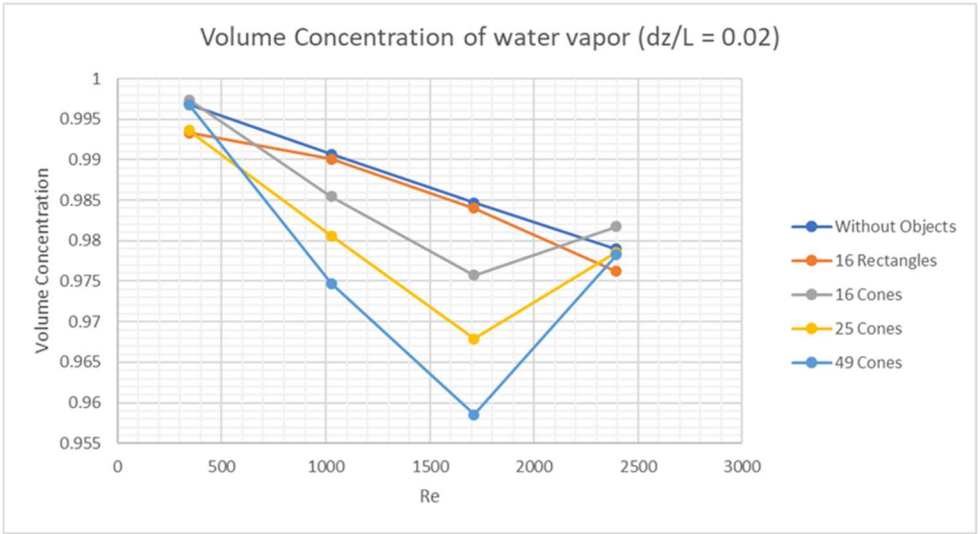

Figure 6.101. Volume concentration of water vapor, at dz/L = 0.02.

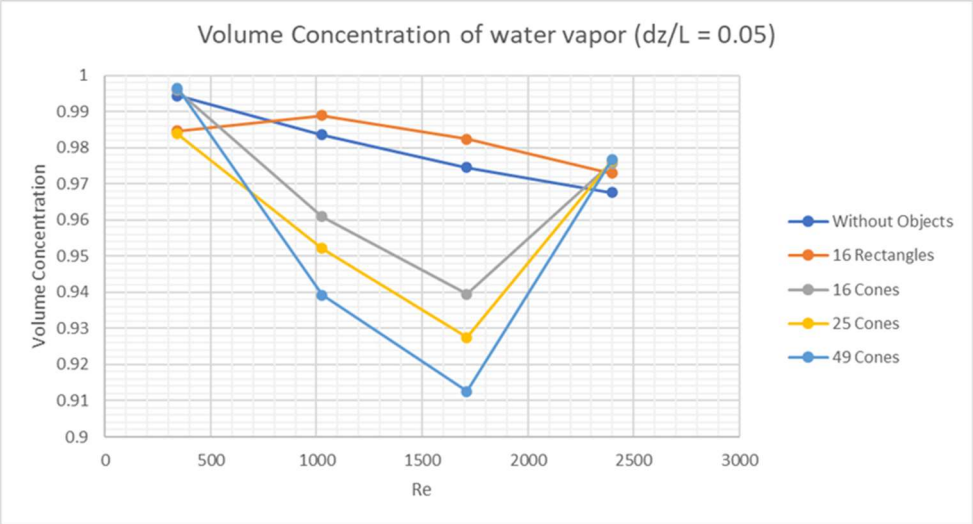

Figure 6.102. Volume concentration of water vapor, at dz/L = 0.05.

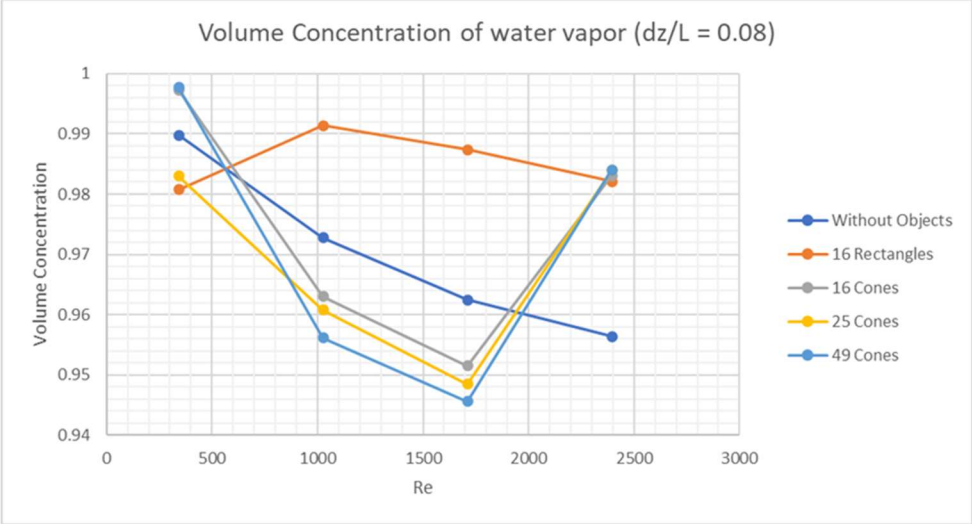

Figure 6.103. Volume concentration of water vapor, at dz/L = 0.08.

The adverse effect of the rectangular blocks on the volume concentration of water vapor is best shown in Figure 6.104. For Re ≥ 1000, the volume concentration farthest from the water surface is greater than the volume concentration near the water surface (dz/L = 0.01). Unlike the inverted cones which is shown to have a lower volume concentration farthest from the wall compared to near the water surface at Re = 1000 and 1700 (see Figure 6.105 to Figure 6.107).

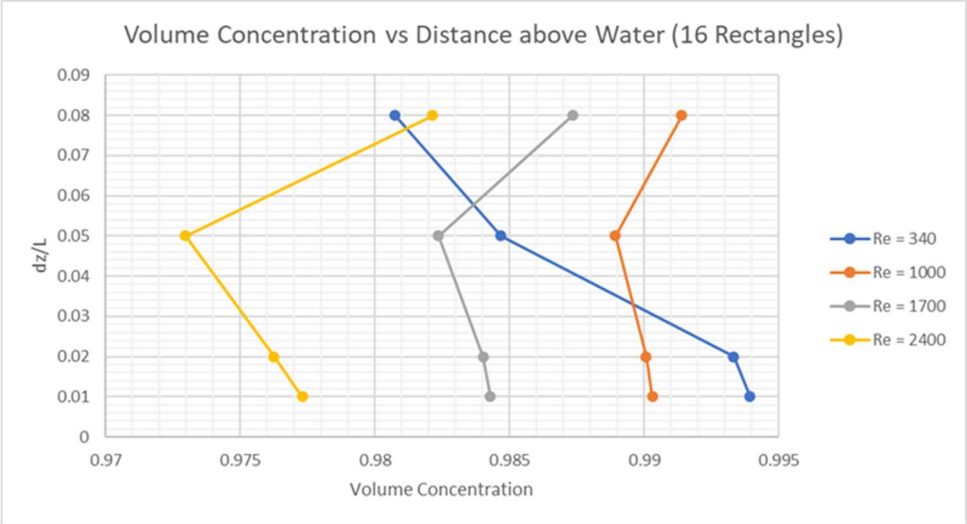

Figure 6.104. Volume concentration of water vapor vs dz/L – 16 Rectangles.

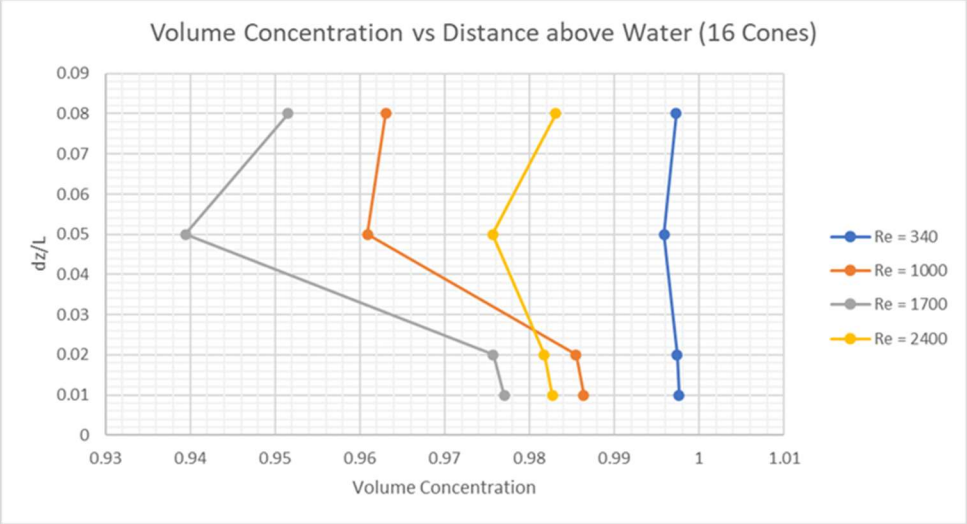

Figure 6.105. Volume concentration of water vapor vs dz/L – 16 Cones.

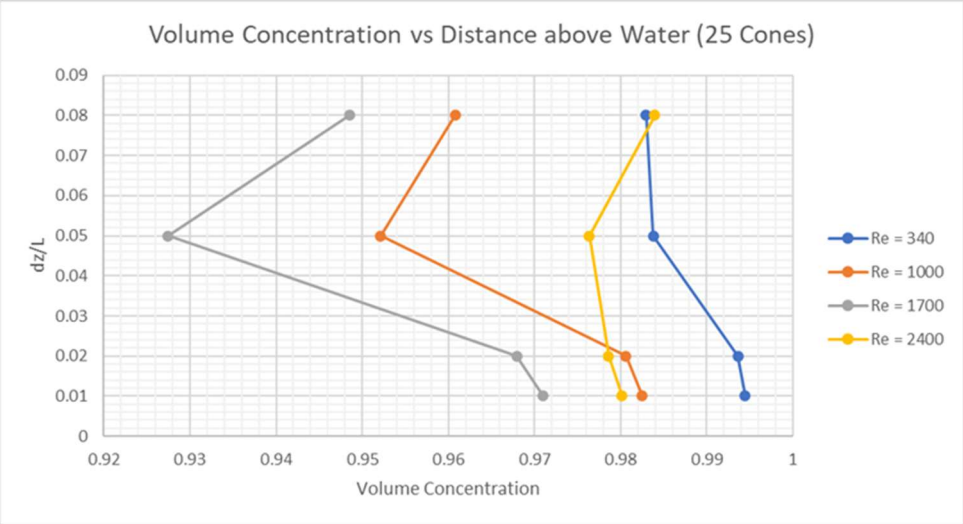

Figure 6.106. Volume concentration of water vapor vs dz/L – 25 Cones.

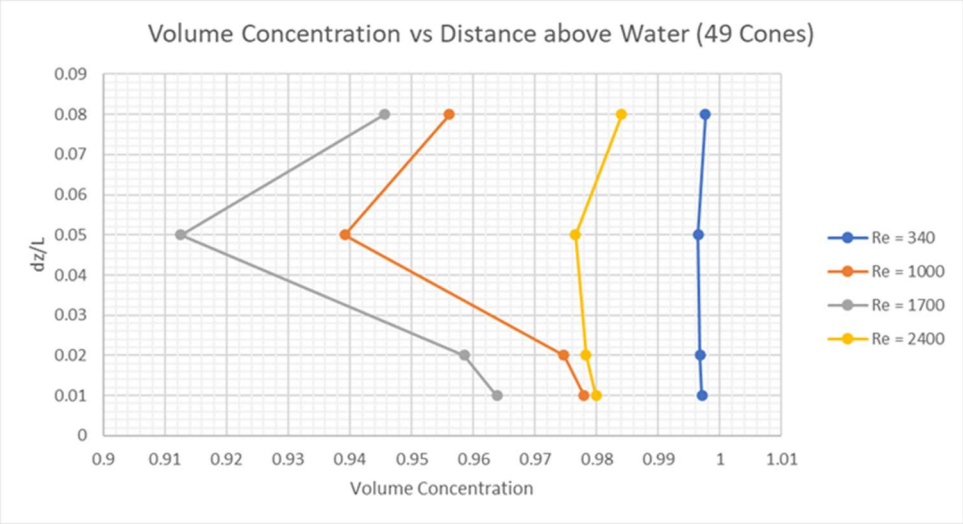

Figure 6.107. Volume concentration of water vapor vs dz/L – 49 Cones.

Chapter 7. CONCLUSION

The transient CFD simulations were cut off before reaching steady state due to limited computing resources available. However, graphs show that the simulations neared an asymptote at the cutoff and all results are treated as steady state.

The air flow and volume flow rate of a fuel tank without objects with the inlet and outlet close to the water surface showed a dependency on the inlet speed. This is due to the effect of buoyancy on the inlet jet decreasing as the inlet speed increases and the water surface acting as a flat plate for higher inlet speeds. The volume flow rate is highest with low inlet speeds and hits a minimum at inlet speed Re = 340. It is also observed that the average volume flow rate decreases when measured farther from the water surface.

Changing the fuel tank design to place the inlet and outlet on the top wall showed the same trends as the fuel tank with the inlet and outlet on the side walls. As the inlet speed increased, the volume flow rate decreased for a fuel tank without objects. Placing floating objects on the water surface greatly affected the air flow and entrainment of water vapor. Rectangular blocks increased the volume flow rate compared to the tank without objects. Inverted cones showed the volume flow rate to decrease at inlet speeds Re = 1000 and 1700 with a local minimum at Re = 1700. Additional cones scaled to size consistently decreased the minimum volume flow rate at each height above the water surface. This is due to reduction in exposed surface area of water, eddies trapped in the concave space between cones, and eddies unable to form between cones.

The volume concentration of water vapor showed a 2% reduction as the inlet speed increased in a fuel tank with the inlet and outlet on the side walls. In the fuel tank with the inlet and outlet on the top wall, the volume concentration decreased by 1.3 – 2.6% near the water surface and 4.5

– 6.4% farther away with the addition of 49 inverted cones evenly distributed across the water surface.

There are multiple possibilities for future research. Changing the static fuel tank design to include baffles may impede the circulation of the fluid layer and potentially reduce the evaporation due to the shear stress caused by the thermocapillary effect [15], [16]. Simulating sloshing of a fuel tank is possible in OpenFOAM (set up described in Appendix C), but it has a high computational expense that, by Moore's Law, will be functionally possible in the near future. Current simulations without sloshing and evaporation calculations each took approximately 400 wall clock hours to run on Hyak using the maximum processors and memory allowed.

Another direction to explore would focus on the floating objects. A higher density of floating objects could lead to reduced air flow over the fluid surface and trap the vapor in the layer between the fluid and top of the floating objects. A study with a higher density of floating objects would work best as a physical experiment to avoid singularities that would likely occur in numerical simulations. Also, the trade-off between additional weight from a high density of floating objects compared to the evaporation reduction could be explored.

For realistic physical applications, an inverted cone with a rounded top would likely be ideal. The inverted cone allows for crowding the floating objects on the surface while keeping upright in situations where the tank is sloshing. The rounded top would allow for any splashing liquid that wets the top to roll off rather than quickly evaporating.

BIBLIOGRAPHY

[1] (2000). *Aircraft Accident Report: In-flight Breakup Over The Atlantic Ocean Trans World Airlines Flight 800 Boeing 747-131, N93119 Near East Moriches, New York July 17,1996.* National Tranportaiton Safety Board.

[2] Jensen, D. L. (2001). Analysis of a Boeing 747 Aircraft Fuel Tank Vent System. *Journal of Aircraft*, 828-834.

[3] Fuel Flammability Task Group. (1998). *A Review of the Flammability Hazard of Jet A Fuel Vapor in Civil Transport Aircraft Fuel Tanks.* U.S. Department of Transportation, Federal Aviation Administration.

[4] Lyulin, Y., & Kabov, O. (2014). Evaporative convection in a horizontal liquid layer under shear–stress gas flow. *International Journal of Heat and Mass Transfer*, 599-609.

[5] Wilcox, D. C. (2007). *Basic Fluid Mechanics* (Third ed.). California: DCW Industries, Inc.

[6] Hirsch, C. (2007). *Numerical Computation of Internal and External Flows* (Second ed.). Oxford: Butterworth-Heinemann.

[7] Greenshields, Christopher J; CFD Direct Ltd. (2015, May 21). *OpenFOAM: The Open Source CFD Toolbox User Guide* (Version 2.4.0 ed.).

[8] OpenCFD. (2018, January 10). *OpenFOAM: Reynolds Averaged Simulation (RAS)*. Retrieved from OpenFOAM: https://www.openfoam.com/documentation/cpp-guide/html/guide-turbulence-ras.html

[9] OpenCFD. (2019, 6 5). *OpenFOAM: User Guide: k-omega Shear Stress Transport (SST)*. Retrieved from OpenFOAM: https://www.openfoam.com/documentation/guides/latest/doc/guide-turbulence-ras-k-omega-sst.html

[10] OPEN CASCADE. (2018, June 4). *History - SALOME Platform*. Retrieved from SALOME: https://www.salome-platform.org/user-section/about/history

[11] *Compute Grid Spacing for a Given Y+*. (2018). Retrieved from Pointwise: https://www.pointwise.com/yplus/index.html

[12] *Overview | ParaView*. (2019, June 7). Retrieved from ParaView: https://www.paraview.org/overview/

[13] Kundu, P. K., & Cohen, I. M. (2010). *Fluid Mechanics, Fourth Edition.* Academic Press.

[14] *JET FUELS, [JP-5] | CAMEO Chemicals | NOAA*. (2022, April). Retrieved from CAMEO Chemicals: https://cameochemicals.noaa.gov/chemical/11699

[15] Abramson, H. N. (1969). *Slosh Suppression.* NASA Space Vehicle Design Criteria (Structures).

[16] Singal, V., Bajaj, J., Awalgaonkar, N., & Tibdewal, S. (2014). CFD Analysis of a Kerosene Fuel Tank to Reduce Liquid Sloshing. *Pocedia Engineering 69*, pp. 1365-1371.

[17] Greenshields, Christopher J.; CFD Direct Ltd. (2015). *OpenFOAM: The Open Source CFD Toolbox Programmer's Guide.*

[18] Wallevik, J. E. (2016, September). *Variation of gravity with time -- CFD Online Discussion Forums*. Retrieved from CFD Online: https://www.cfd-online.com/Forums/openfoam-programming-development/71740-variation-gravity-time-2.html

[19] *Wolfram: Computation Meets Knowledge*. (2022, May). Retrieved from Moment of Inertia of a Cone | Wolfram Formula Repository: https://resources.wolframcloud.com/FormulaRepository/resources/Moment-of-Inertia-of-a-Cone

APPENDIX A

Density of Water Vapor

The density of water vapor at standard temperature and pressure was calculated using the ideal gas law equation

$$PV = nRT\ , \tag{A.1}$$

where P is pressure, V is volume, n is number of moles, R is gas constant, and T is temperature. The density equation and molar mass equation are given respectively by

$$\rho = \frac{m}{V} \tag{A.2}$$

$$n = \frac{m}{M}\,, \tag{A.3}$$

where m is mass and M is molar mass. Applying these back into equation (A.1) yields

$$\rho = \frac{PM}{RT}\,. \tag{A.4}$$

Plugging in the molar mass for water gives the density for water vapor:

$$\rho = \frac{(1\ \text{atm})\left(18.01528\ \frac{\text{g}}{\text{mol}}\right)}{\left(0.082057\ \frac{\text{L·atm}}{\text{mol·K}}\right)(273.15\ \text{K})} = 0.80376\ \frac{\text{g}}{\text{L}}\,. \tag{A.5}$$

APPENDIX B

Additional Flow Visualizations

These are additional streamline and velocity vector plots for Configuration 2 of the fuel tank with and without floating objects added. The inlet is on the left and the outlet is on the right. The streamlines are traced from the inlet (0.167, 0.25, 0.49), the outlet (0.333, 0.25, 0.49), and directly below the inlet near the water surface (0.167, 0.25, 0.26) or at the top of the largest floating object (0.167, 0.25, 0.275).

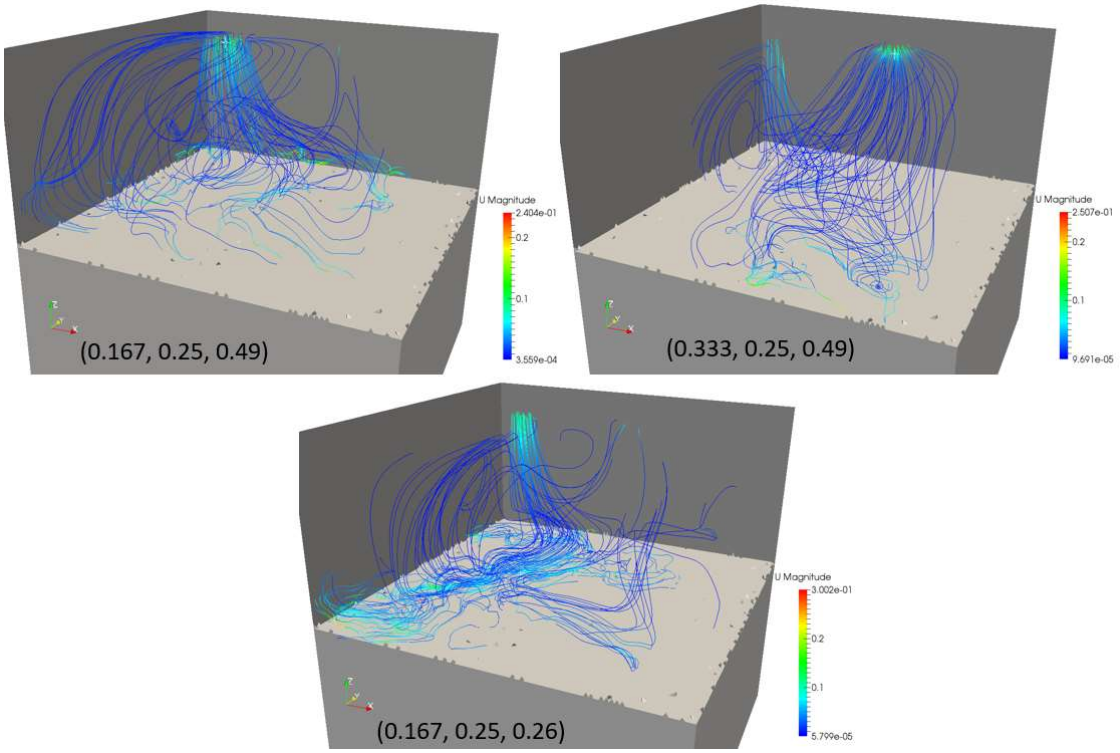

Figure B.1. Streamlines for fuel tank without objects, at Re = 340.

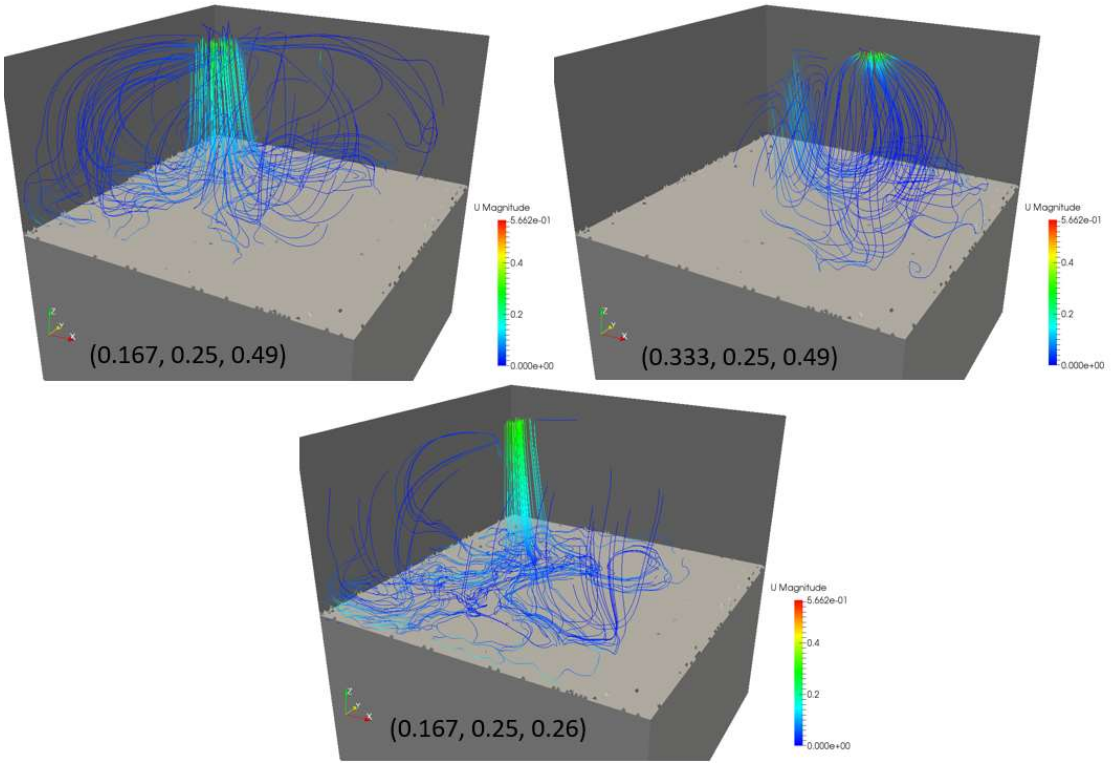

Figure B.2. Streamlines for fuel tank without objects, at Re = 1000.

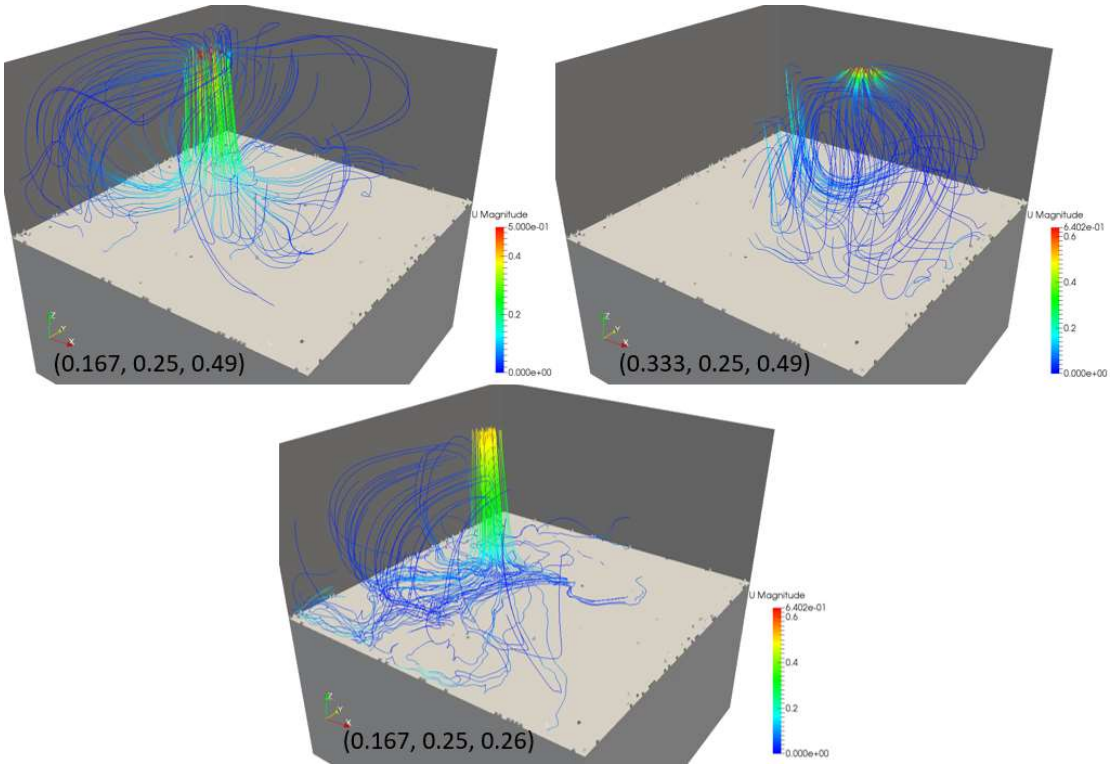

Figure B.3. Streamlines for fuel tank without objects, at Re = 1700.

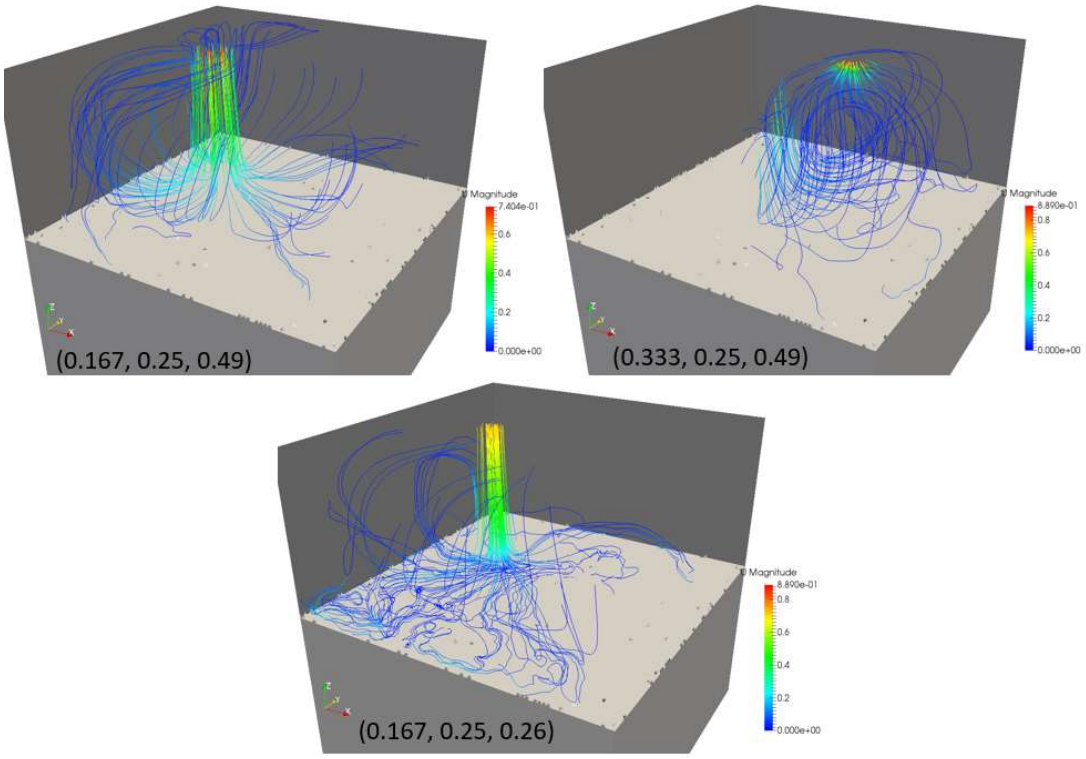

Figure B.4. Streamlines for fuel tank without objects, at Re = 2400.

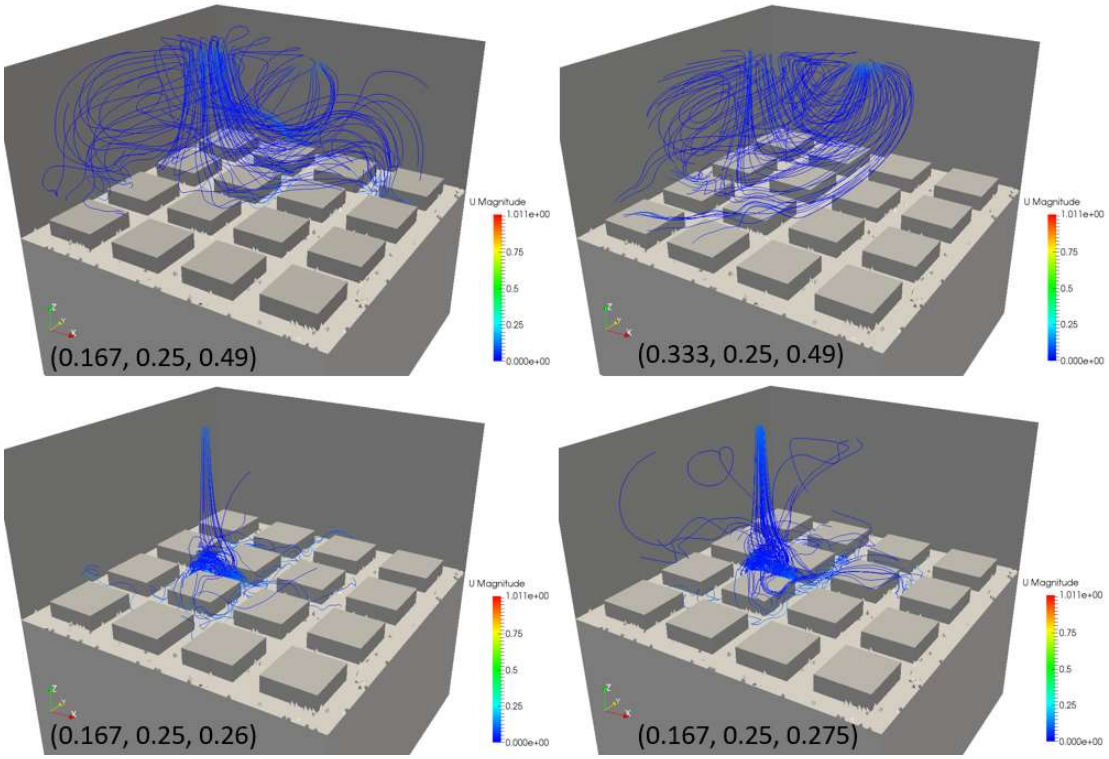

Figure B.5. Streamlines for 16 Rectangles, at Re = 340.

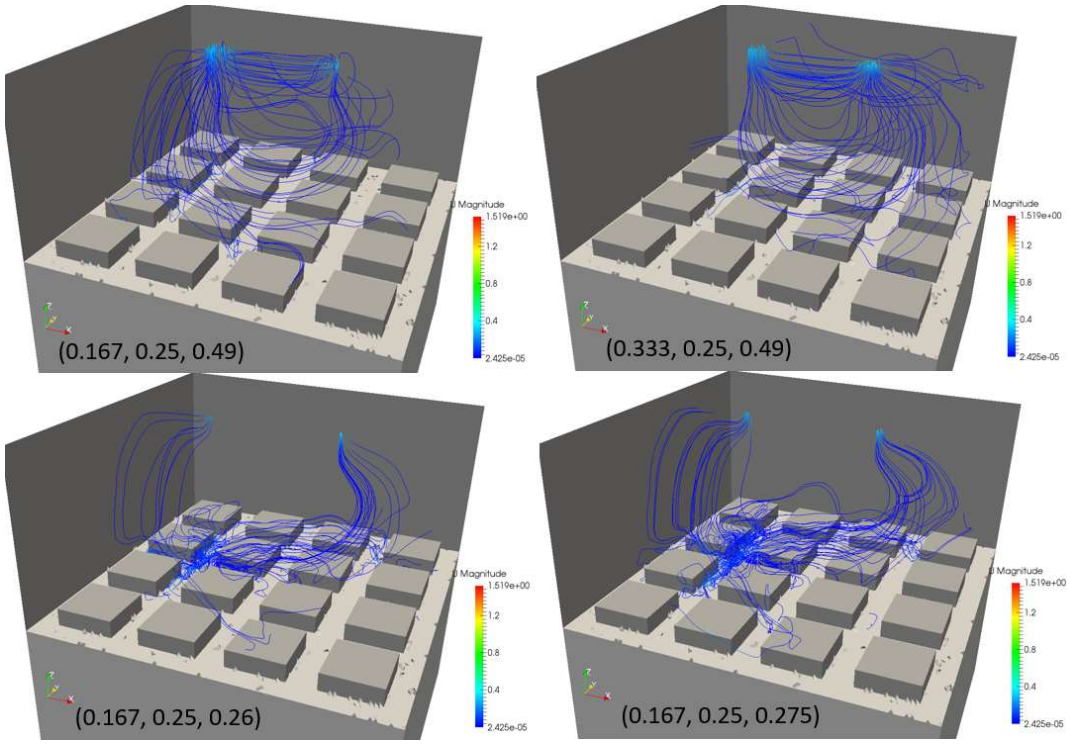

Figure B.6. Streamlines for 16 Rectangles, at Re = 1000.

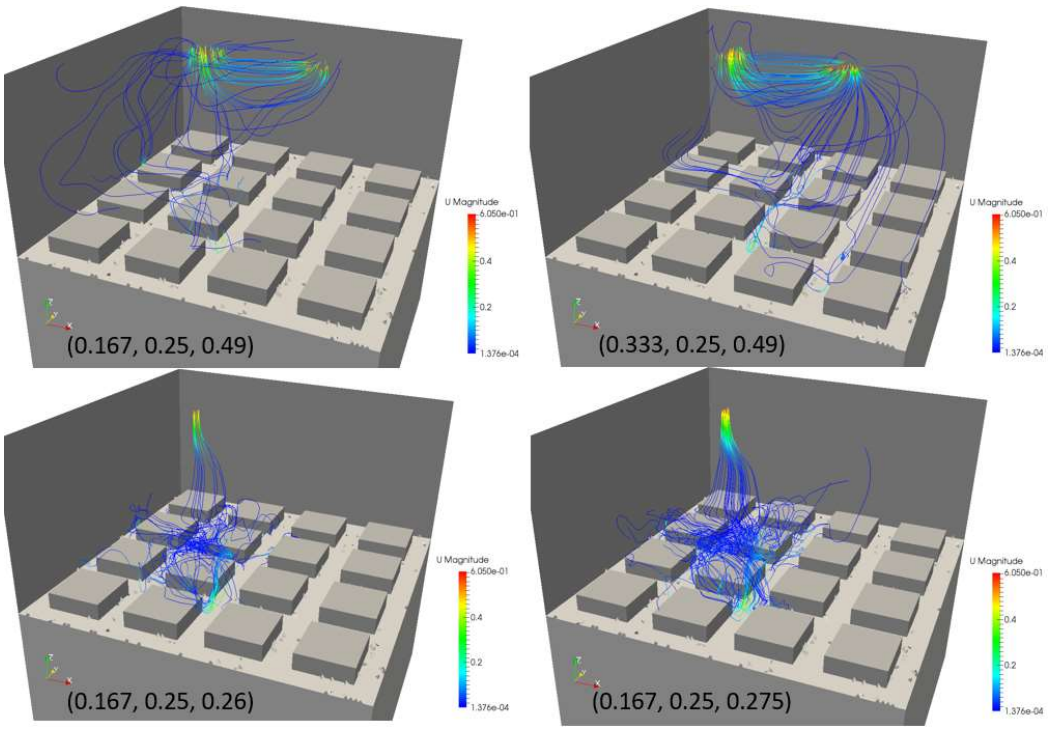

Figure B.7. Streamlines for 16 Rectangles, at Re = 1700.

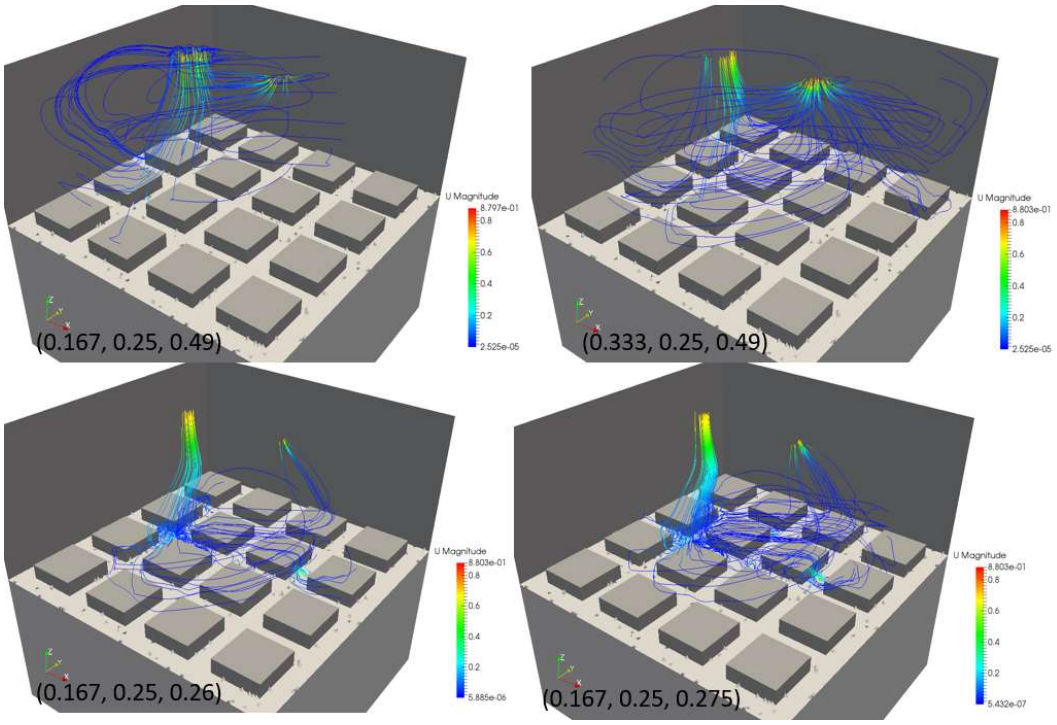

Figure B.8. Streamlines for 16 Rectangles, at Re = 2400.

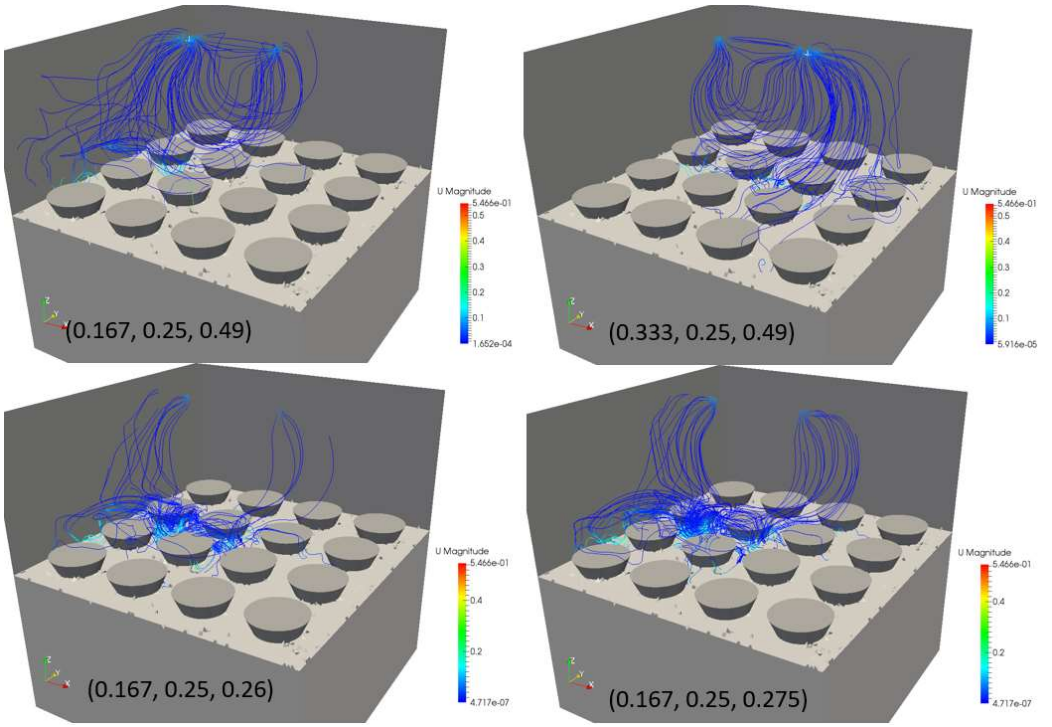

Figure B.9. Streamlines for 16 Cones, at Re = 340.

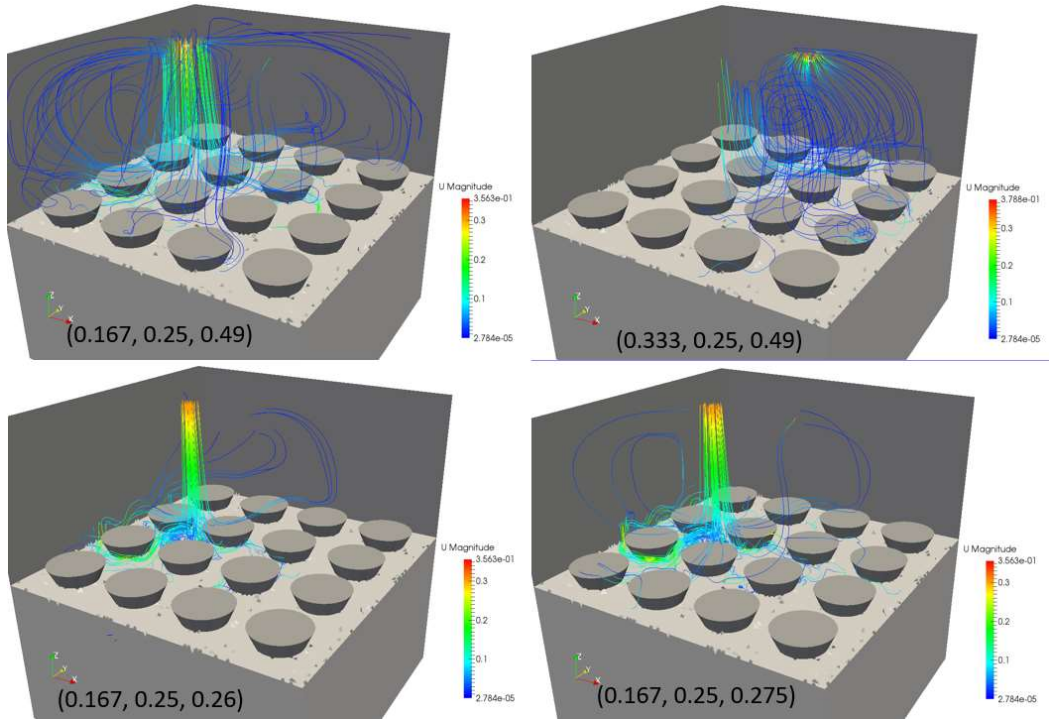

Figure B.10. Streamlines for 16 Cones, at Re = 1000.

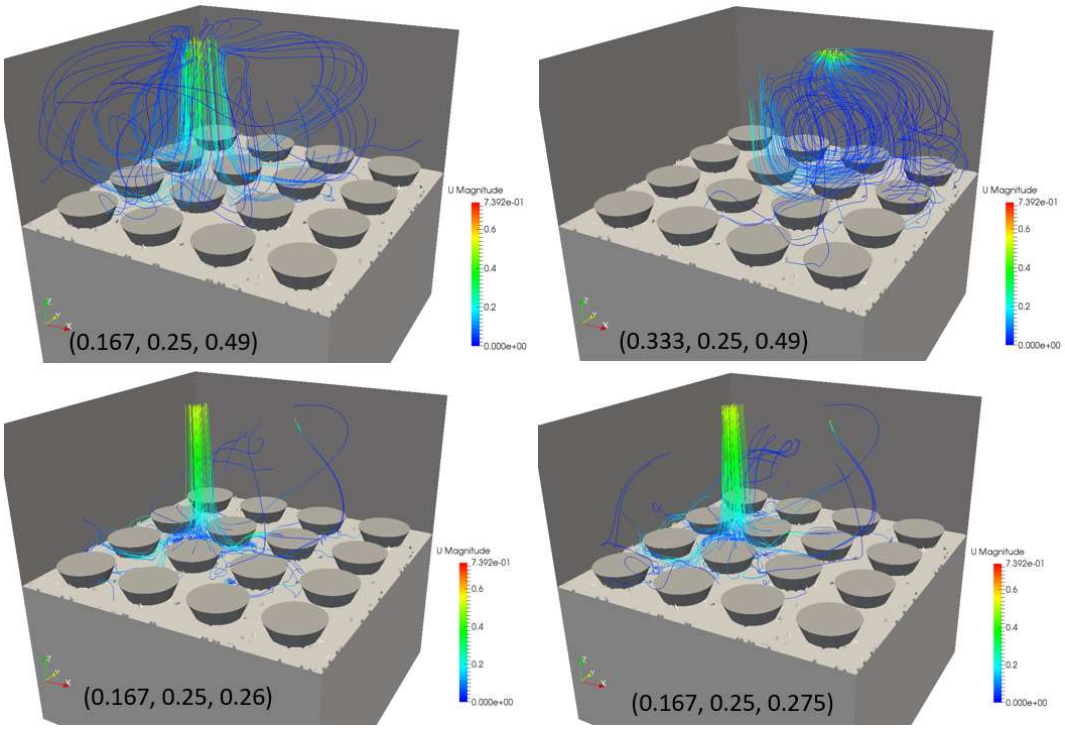

Figure B.11. Streamlines for 16 Cones, at Re = 1700.

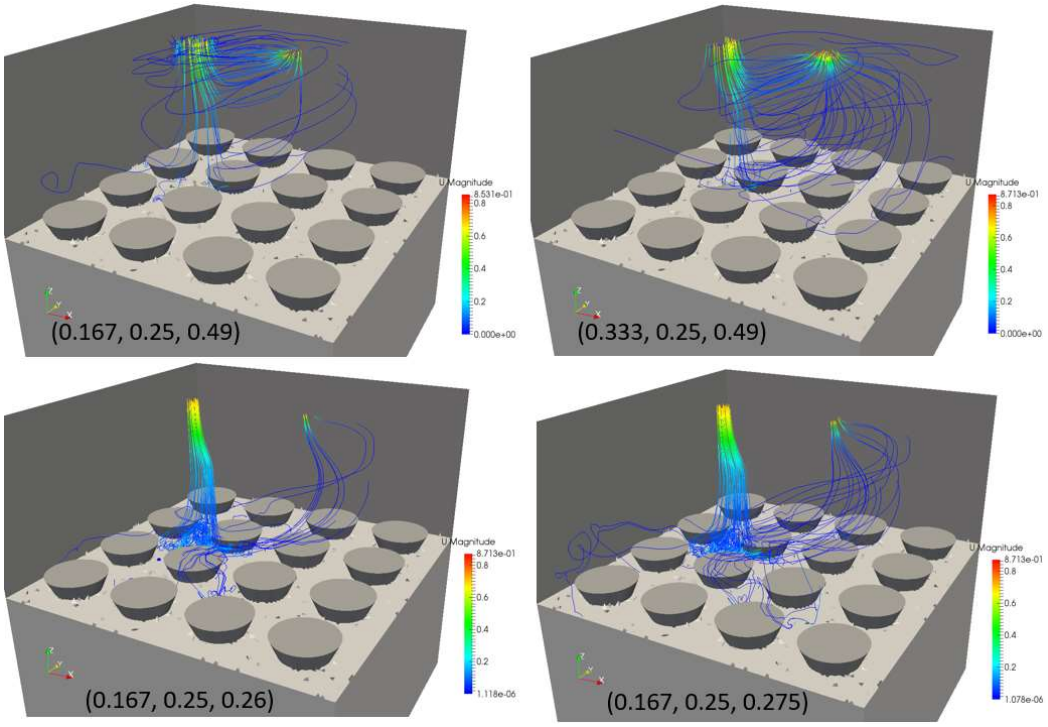

Figure B.12. Streamlines for 16 Cones, at Re = 2400.

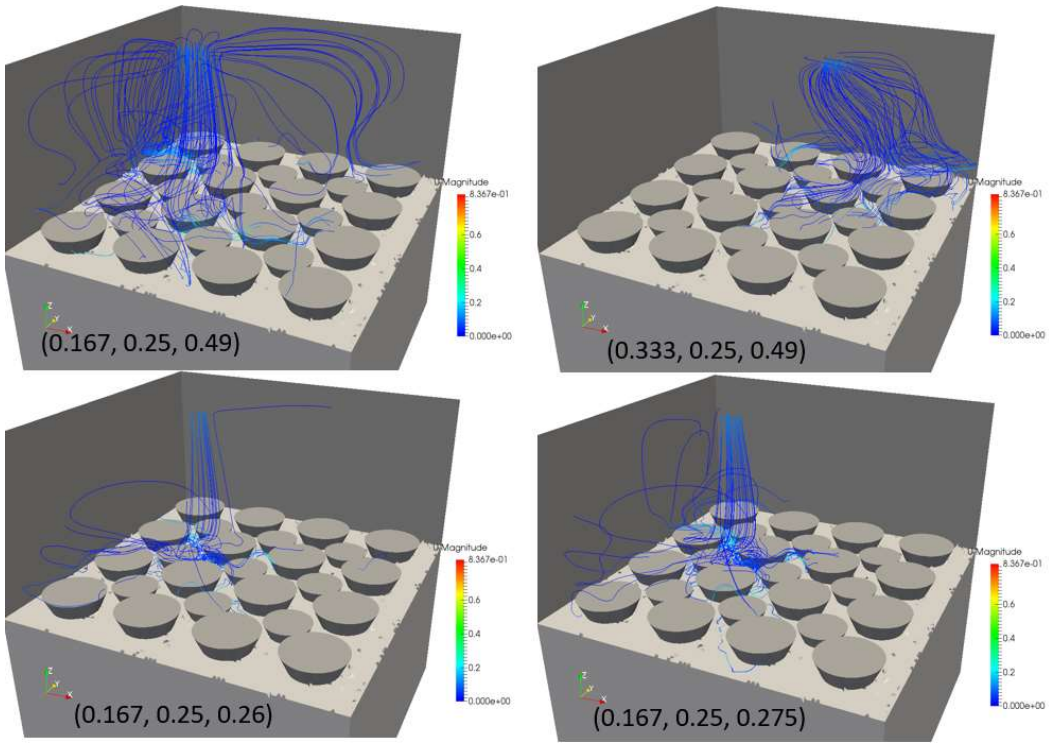

Figure B.13. Streamlines for 25 Cones, at Re = 340.

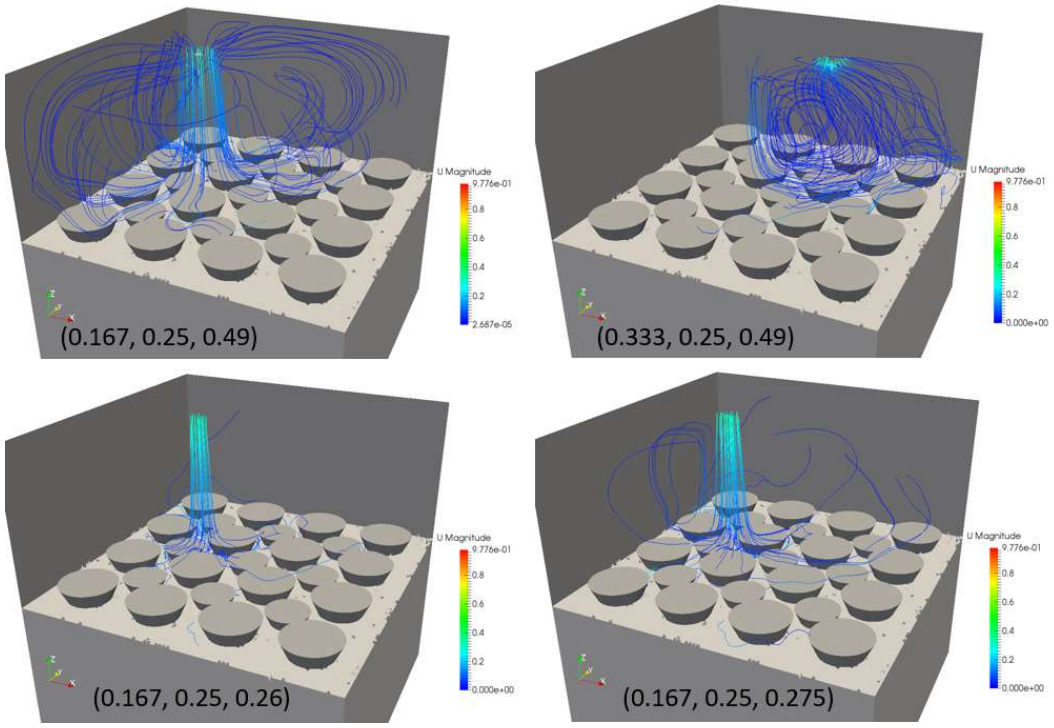

Figure B.14. Streamlines for 25 Cones, at Re = 1000.

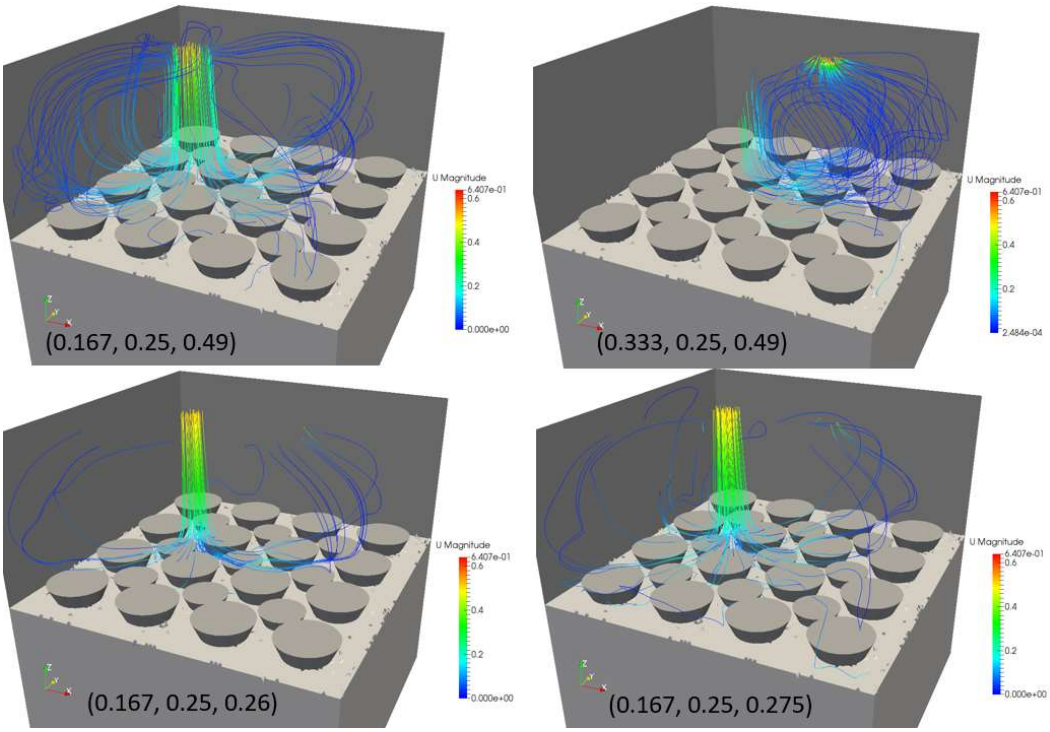

Figure B.15. Streamlines for 25 Cones, at Re = 1700.

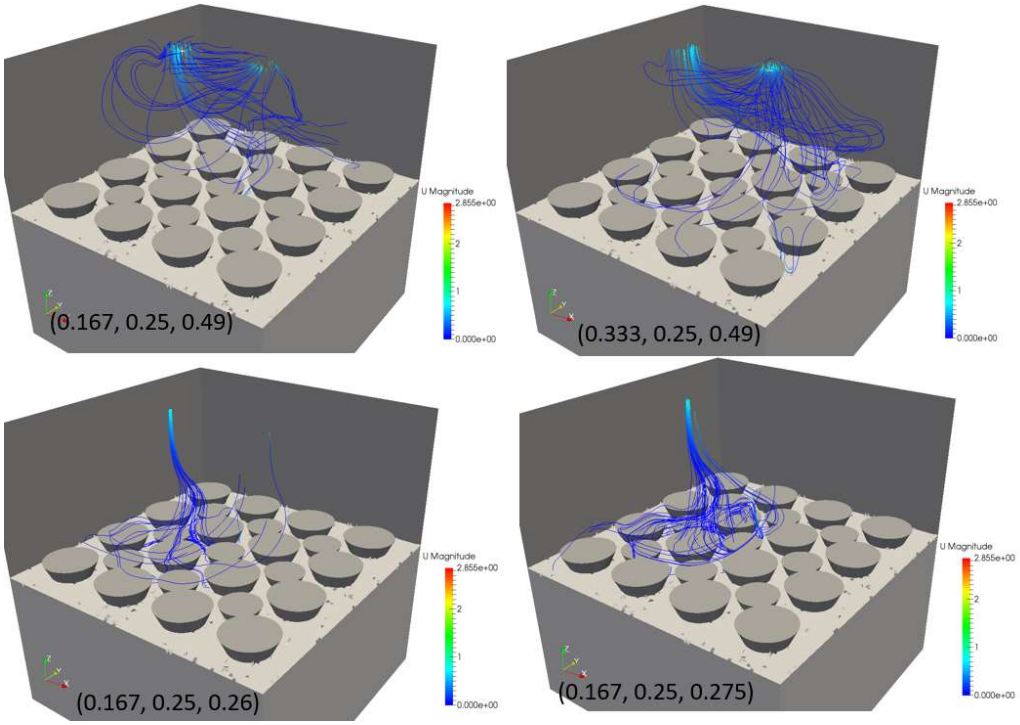

Figure B.16. Streamlines for 25 Cones, at Re = 2400.

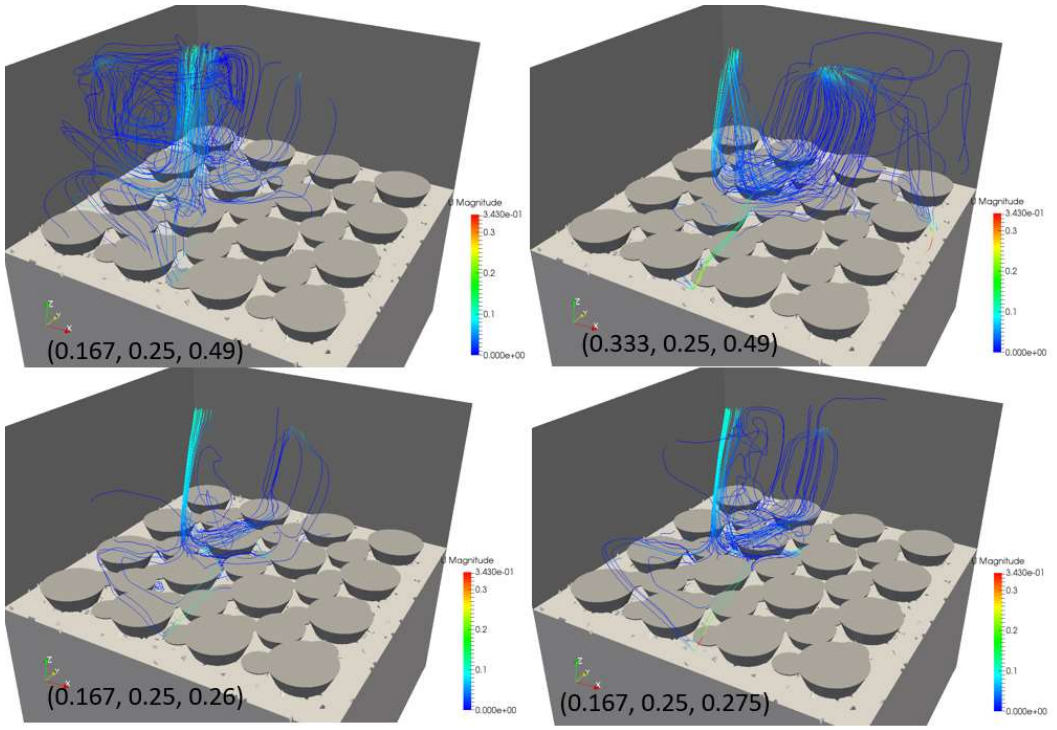

Figure B.17. Streamlines for 49 Cones, at Re = 340.

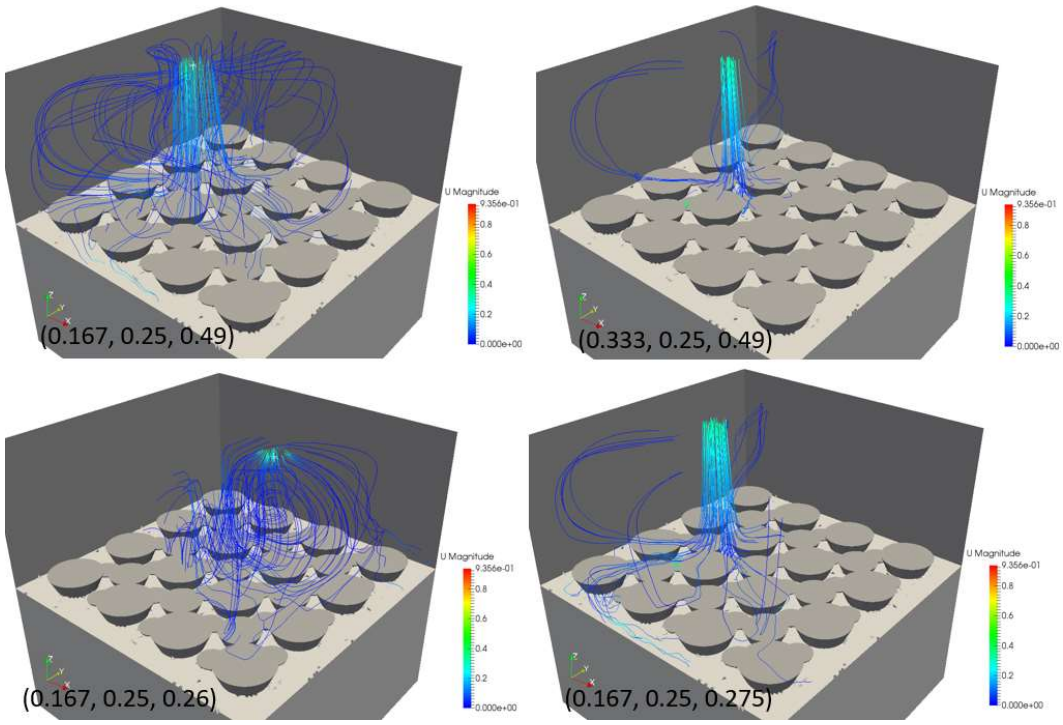

Figure B.18. Streamlines for 49 Cones, at Re = 1000.

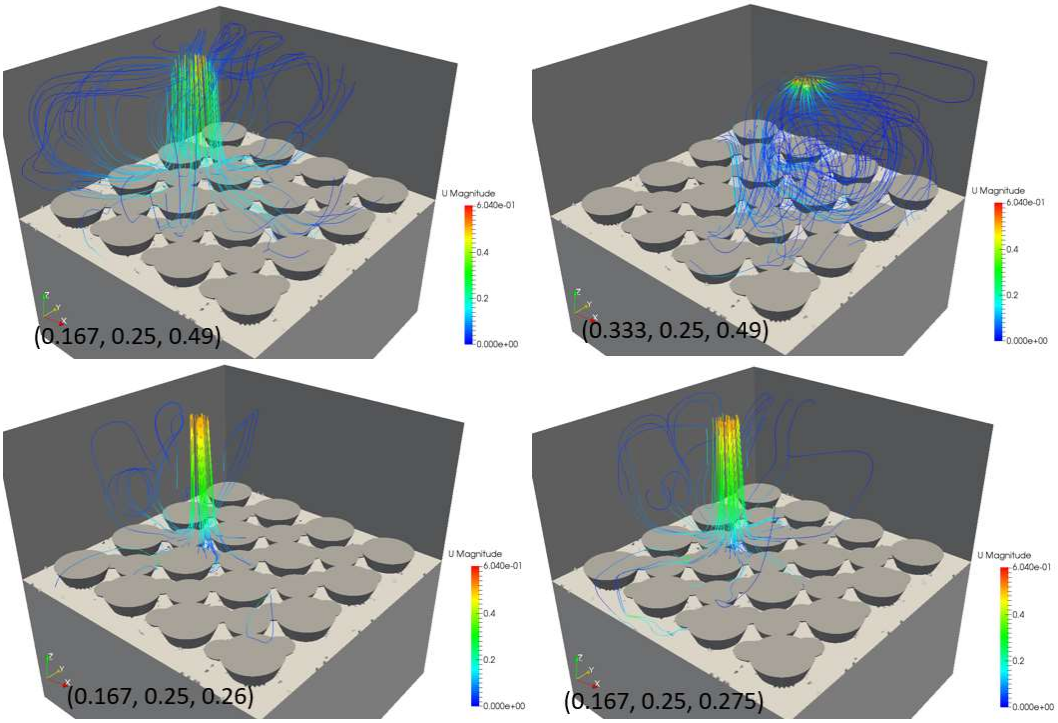

Figure B.19. Streamlines for 49 Cones, at Re = 1700.

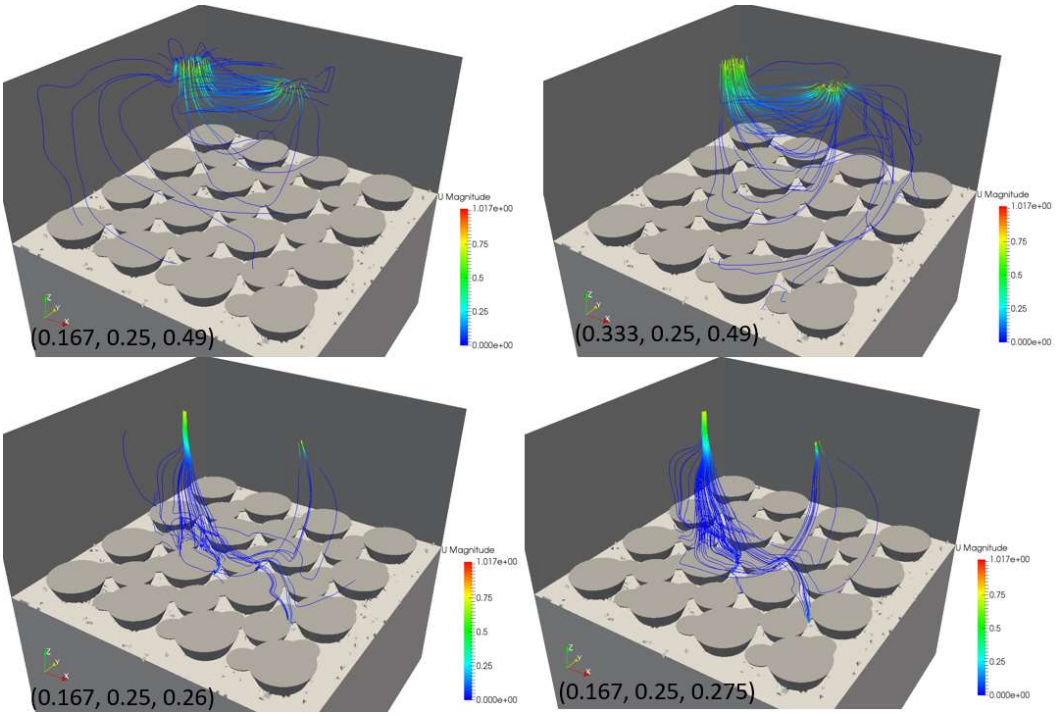

Figure B.20. Streamlines for 49 Cones, at Re = 2400.

The velocity vectors in the liquid layer on a slice through the center of the Configuration 2 fuel tank. The inlet is on the left and the outlet is on the right along the top edge of the tank.

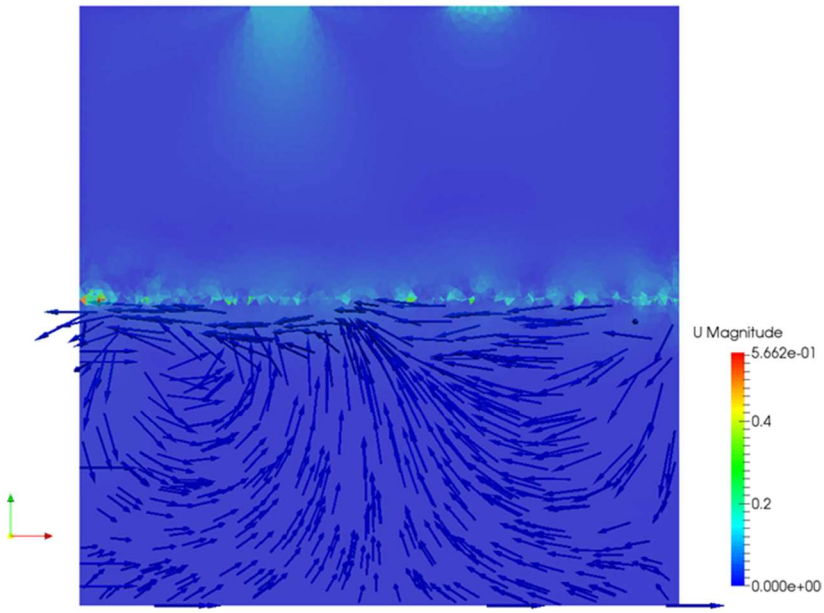

Figure B.21. Velocity vectors in the liquid layer for fuel tank without objects, at Re = 340.

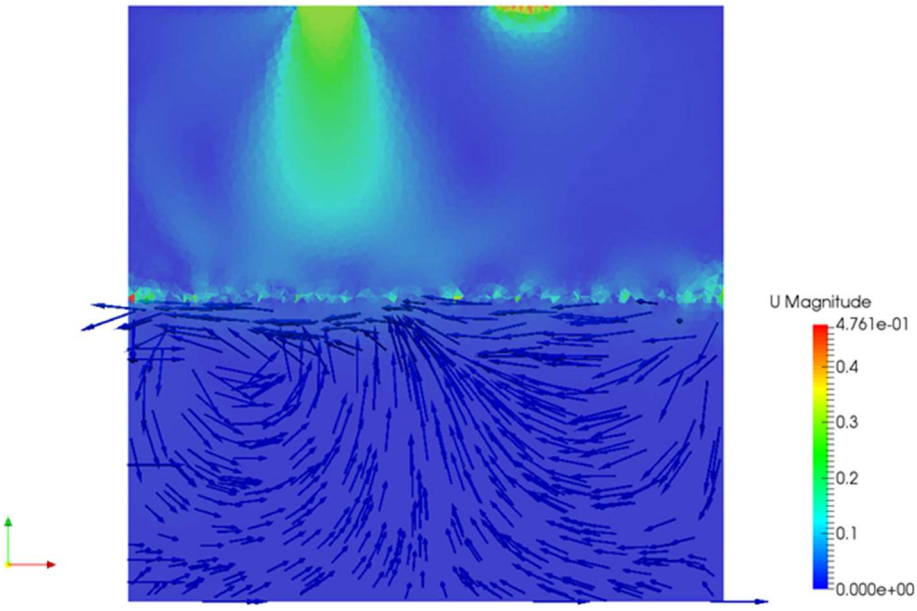

Figure B.22. Velocity vectors in the liquid layer for fuel tank without objects, at Re = 1000.

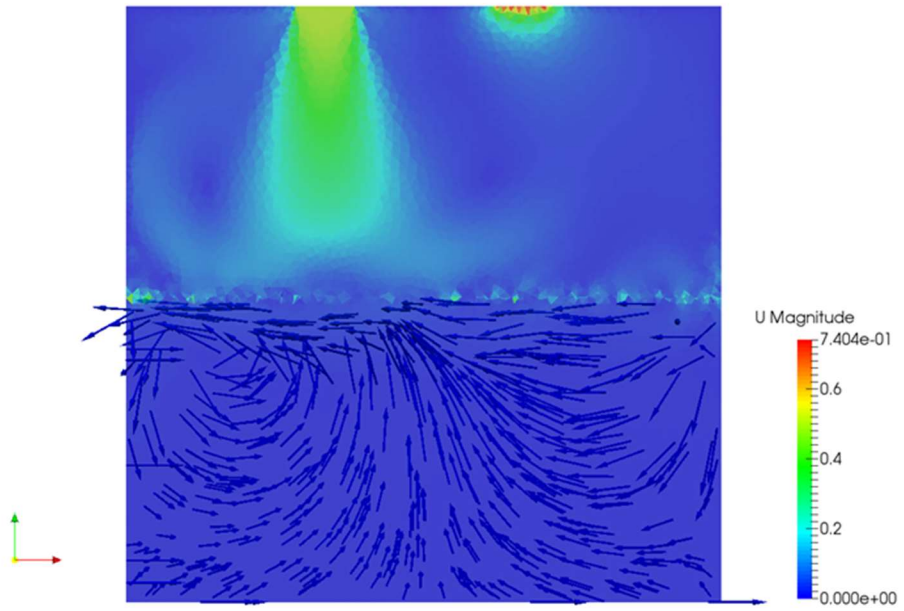

Figure B.23. Velocity vectors in the liquid layer for fuel tank without objects, at Re = 1700.

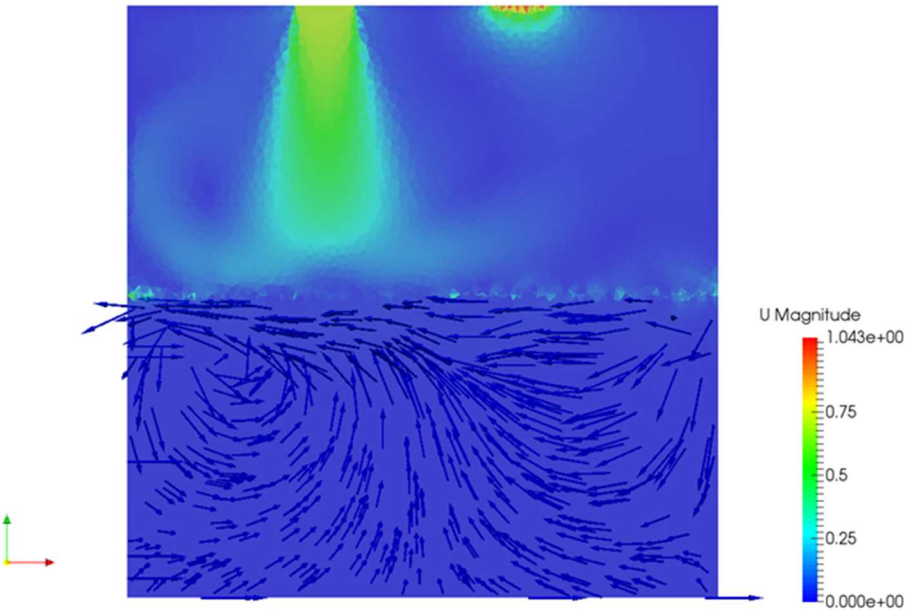

Figure B.24. Velocity vectors in the liquid layer for fuel tank without objects, at Re = 2400.

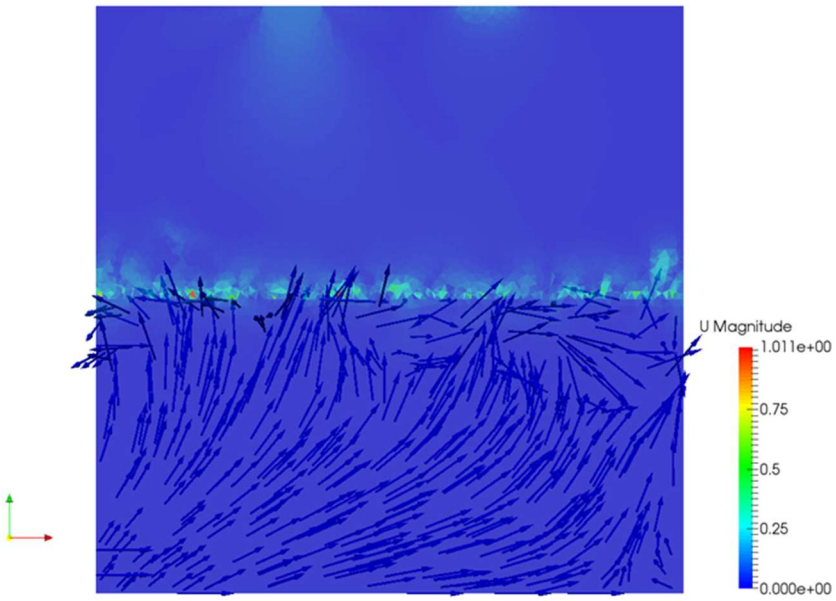

Figure B.25. Velocity vectors in the liquid layer for 16 Rectangles, at Re = 340.

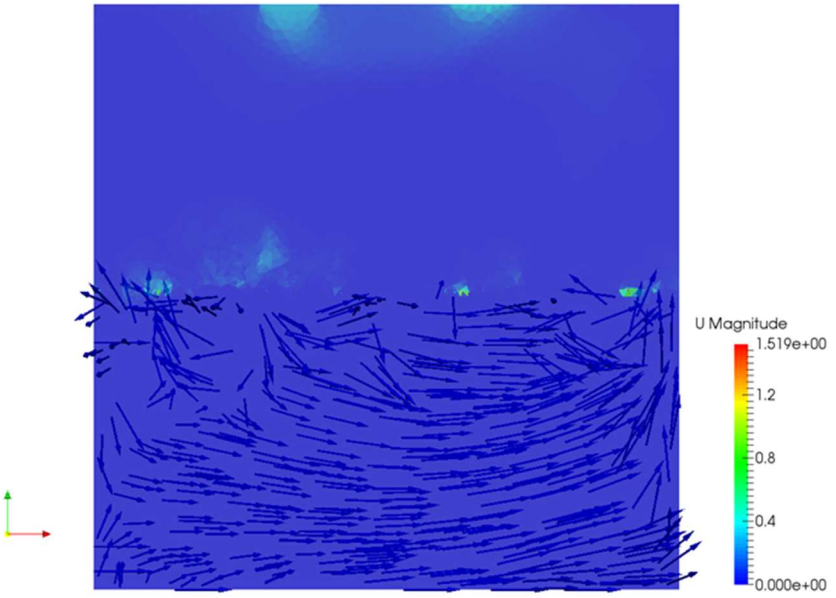

Figure B.26. Velocity vectors in the liquid layer for 16 Rectangles, at Re = 1000.

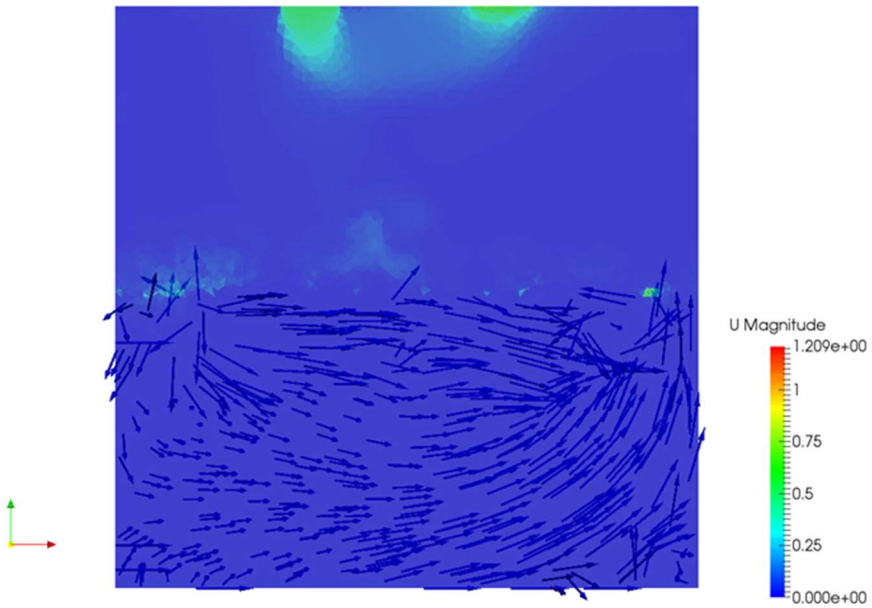

Figure B.27. Velocity vectors in the liquid layer for 16 Rectangles, at Re = 1700.

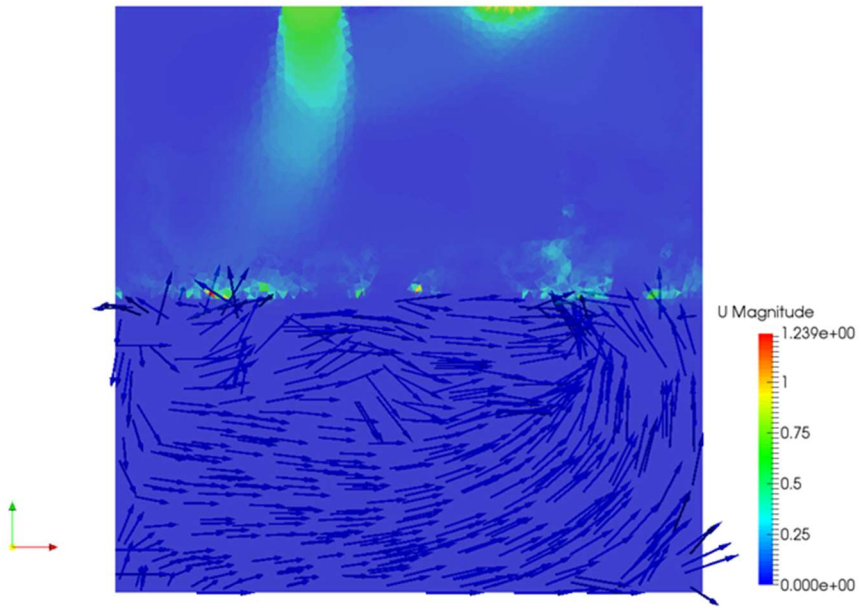

Figure B.28. Velocity vectors in the liquid layer for 16 Rectangles, at Re = 2400.

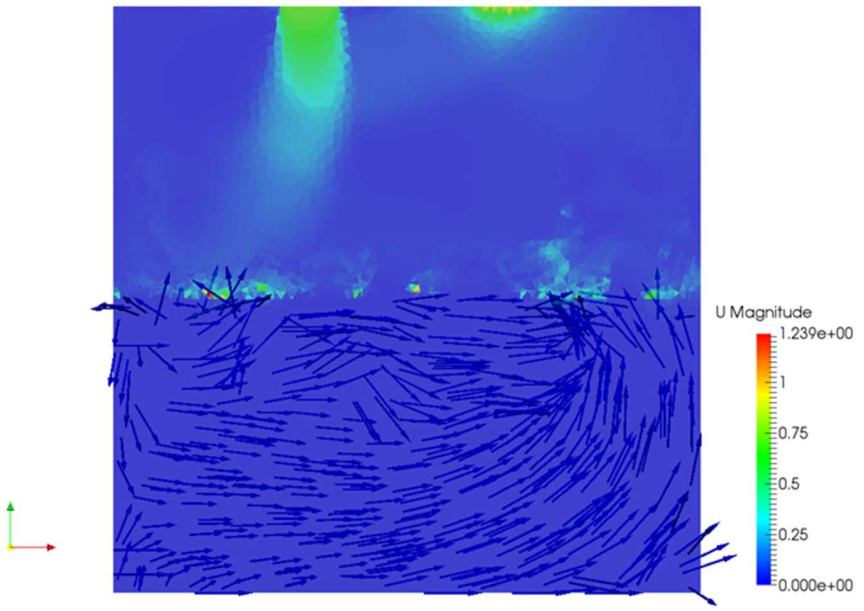

Figure B.29. Velocity vectors in the liquid layer for 16 Cones, at Re = 340.

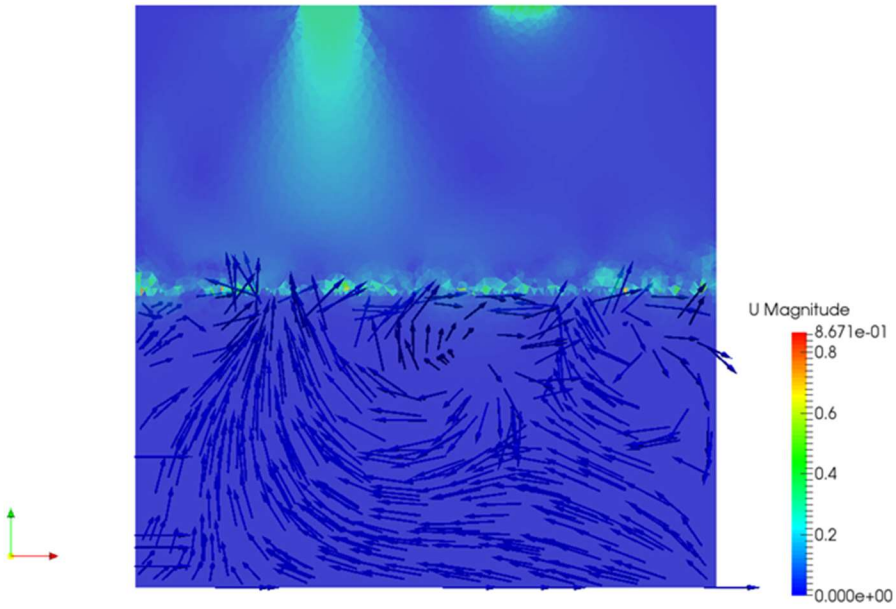

Figure B.30. Velocity vectors in the liquid layer for 16 Cones, at Re = 1000.

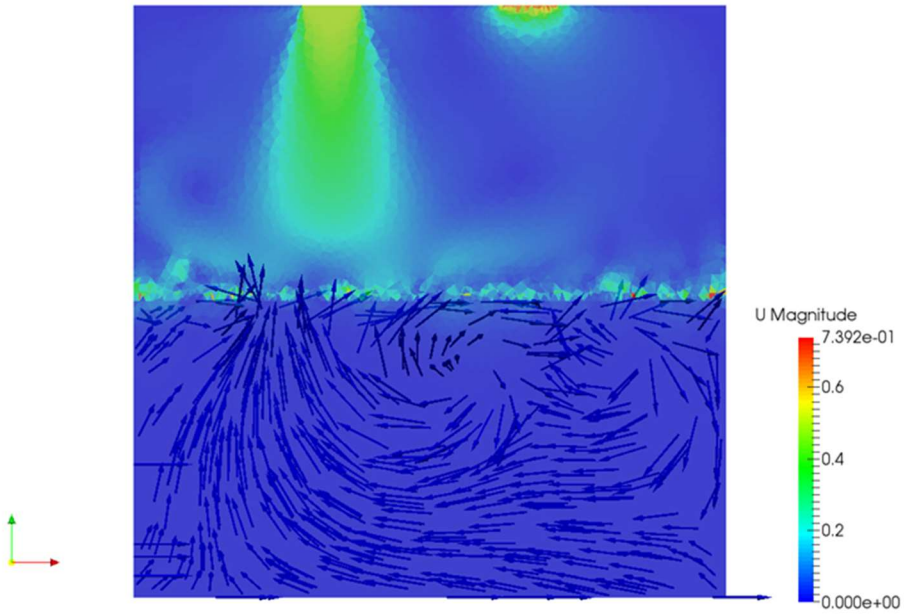

Figure B.31. Velocity vectors in the liquid layer for 16 Cones, at Re = 1700.

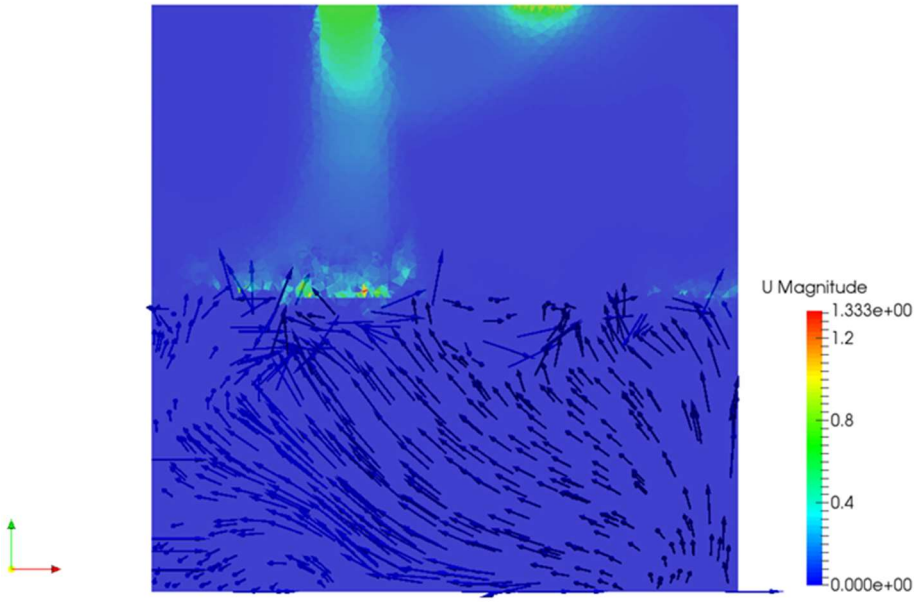

Figure B.32. Velocity vectors in the liquid layer for 16 Cones, at Re = 2400.

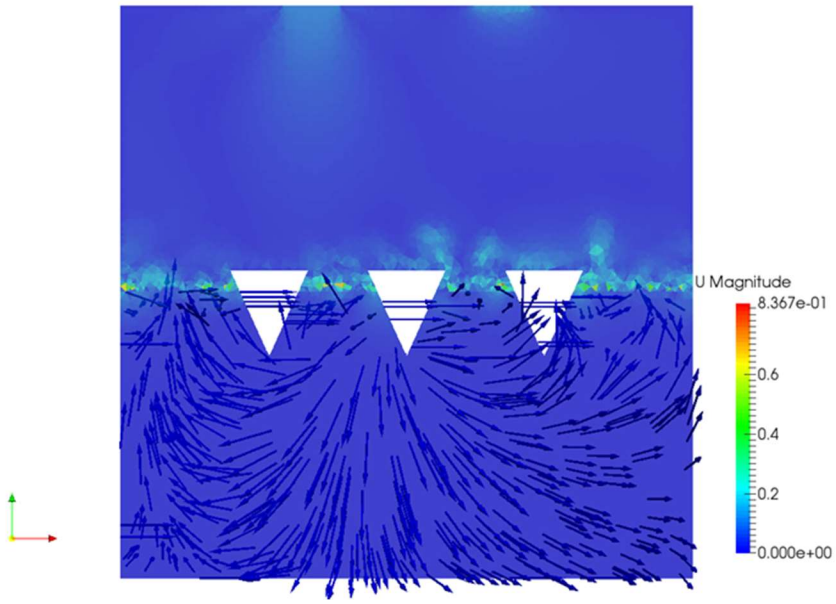

Figure B.33. Velocity vectors in the liquid layer for 25 Cones, at Re = 340.

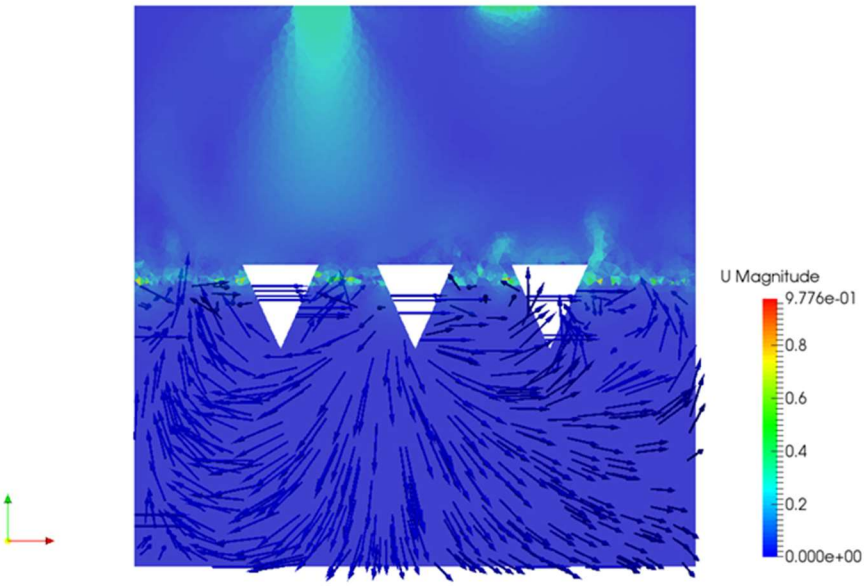

Figure B.34. Velocity vectors in the liquid layer for 25 Cones, at Re = 1000.

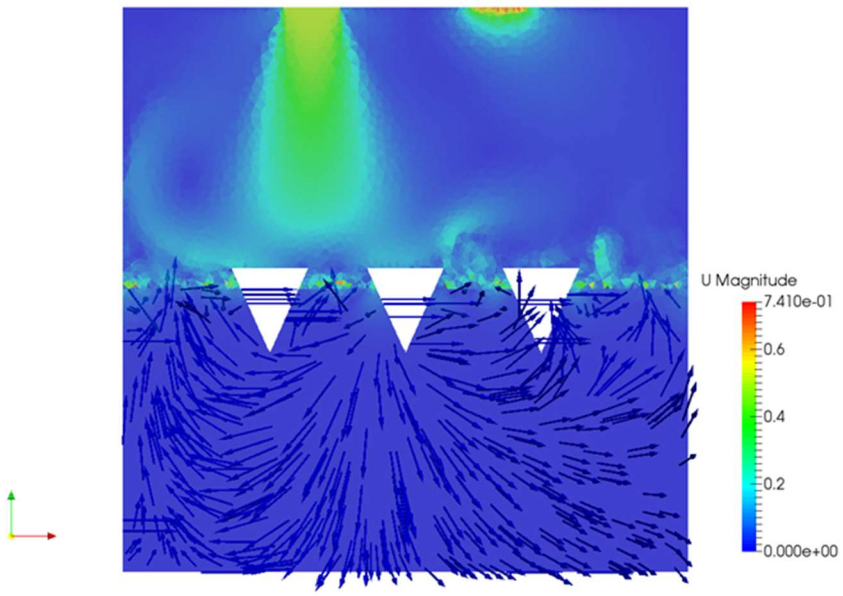

Figure B.35. Velocity vectors in the liquid layer for 25 Cones, at Re = 1700.

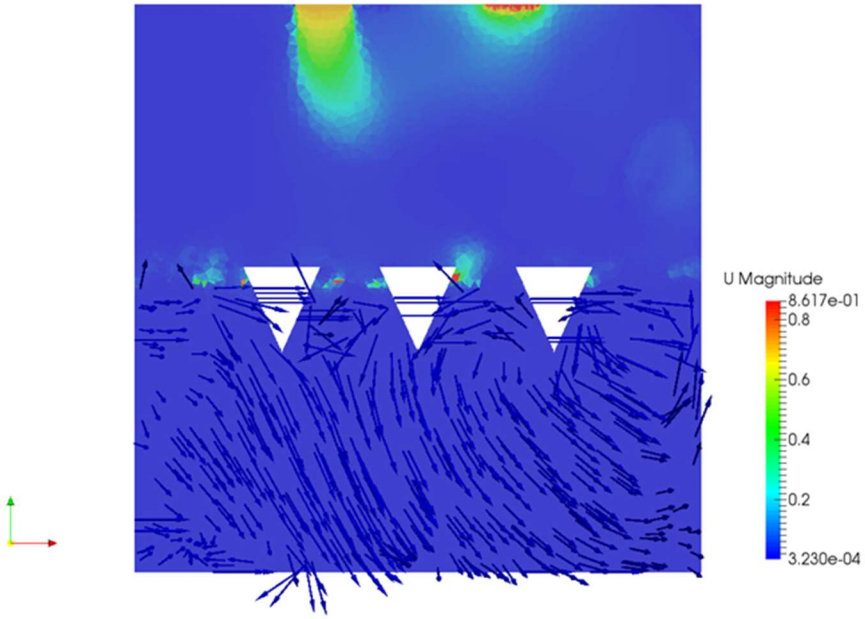

Figure B.36. Velocity vectors in the liquid layer for 25 Cones, at Re = 2400.

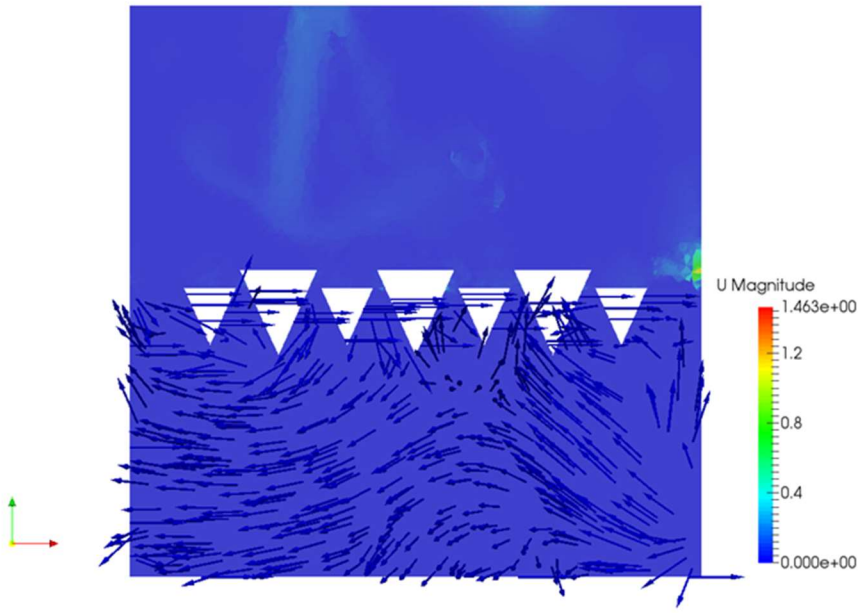

Figure B.37. Velocity vectors in the liquid layer for 49 Cones, at Re = 340.

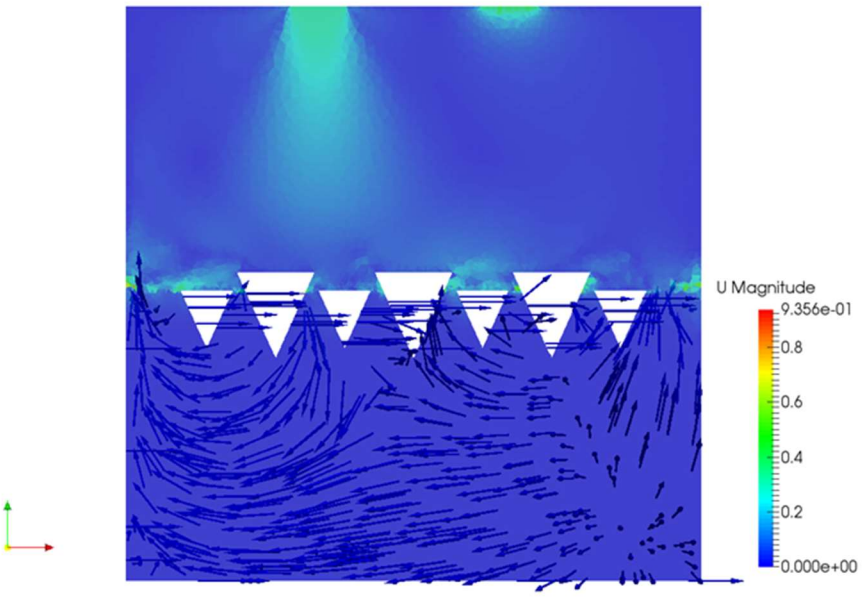

Figure B.38. Velocity vectors in the liquid layer for 49 Cones, at Re = 1000.

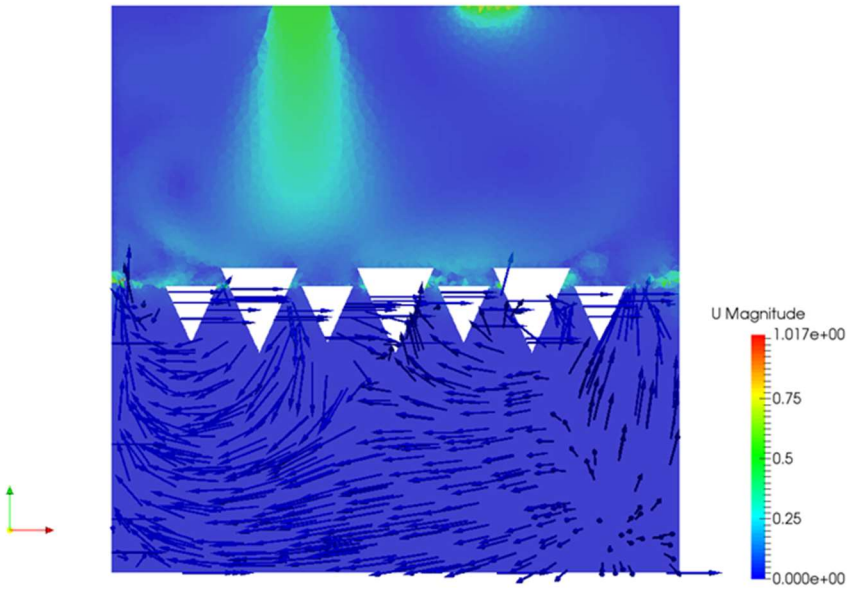

Figure B.39. Velocity vectors in the liquid layer for 49 Cones, at Re = 1700.

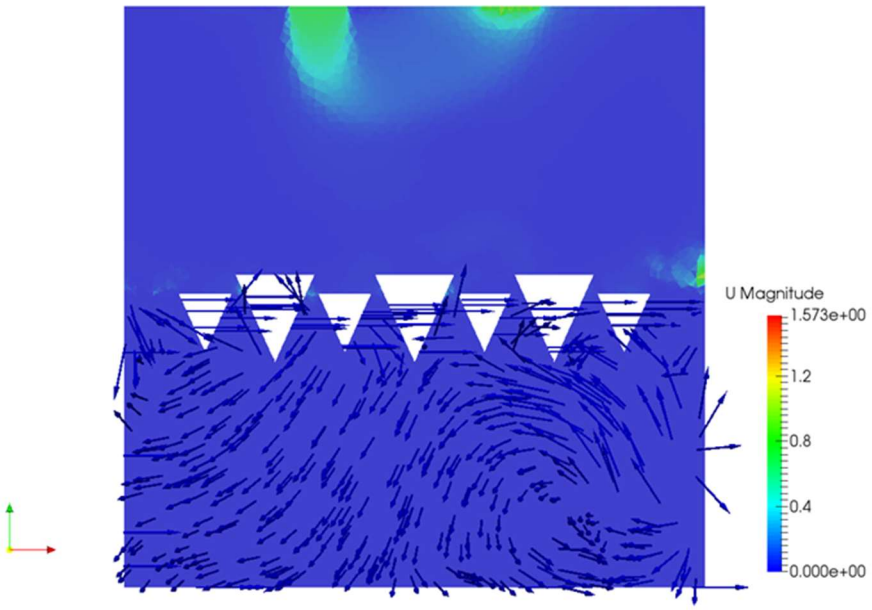

Figure B.40. Velocity vectors in the liquid layer for 49 Cones, at Re = 2400.

APPENDIX C

CFD Simulation with sloshing

Setting up an OpenFOAM simulation with sloshing fluid in the fuel tank requires modifying the solver interDyMFoam. Modeling sloshing can be done by moving the gravity vector in a pattern that mimics a pendulum swinging in the x-z plane. This generates waves as if the fuel tank was rocking on the y-axis at the center of gravity. For a 4 second period, the gravity vector for sloshing is given by

$$\boldsymbol{g}_{slo} = \begin{bmatrix} |\boldsymbol{g}| \cos\left(A \sin\left(\frac{\pi}{2}t\right) + \frac{3}{2}\pi\right) \\ 0 \\ |\boldsymbol{g}| \sin\left(A \sin\left(\frac{\pi}{2}t\right) + \frac{3}{2}\pi\right) \end{bmatrix}, \tag{C.1}$$

where A is the angle of tilt in radians and $\boldsymbol{g}$ is gravity. Using the compound-angle formula trigonometric identity

$$\cos(a+b) = \cos(a)\cos(b) - \sin(a)\sin(b) \tag{C.2}$$

$$\sin(a+b) = \sin(a)\cos(b) + \sin(a)\cos(b)\,, \tag{C.3}$$

the gravity vector (C.1) is simplified to

$$\boldsymbol{g}_{slo} = \begin{bmatrix} |\boldsymbol{g}| \sin\left(A \sin\left(\frac{\pi}{2}t\right)\right) \\ 0 \\ |\boldsymbol{g}| \cos\left(A \sin\left(\frac{\pi}{2}t\right)\right) \end{bmatrix}. \tag{C.4}$$

To implement sloshing at any angle A, the gravity vector is hard coded in the interDyMFoam solver (written in C++) [17] and then recompiled in OpenFOAM. Then the edited gravity vector was inserted at the beginning of each calculation for a new timestep. An example of the gravity vector code for a tilt of 30° is given by:

```
const dimensionedScalar gunits("gunits", dimensionSet (0,1,-2,0,0,0,0), 9.81);
g = gunits*Foam::sin(pi*Foam::sin(runtime.value()*pi/2.0)/6.0)*vector(1,0,0)-
gunits*Foaam::cos(pi*Foam::sin(runtime.value()*pi/2.0)/6.0)*vector(0,0,1);
```

where gunits is the value of gravity, 9.81 m/s^2. Then the following lines were added to override the gravity vector of the previous timestep before the moving mesh is updated: [18]

```
Info<< "Calculating field g.h\n" << endl;
volScalarField gh("gh", g & mesh.C());
surfaceScalarField ghf("ghf", g & mesh.Cf());
```

The solver interDyMFoam is capable of tracking multiple moving meshes allowing each floating object to move independently inside the fuel tank. Using the Partition tool in SALOME, a zone containing the entire mesh except for the floating object of interest is created for each floating object. It is necessary to use an unstructured mesh to avoid singularities as the mesh stretches when the inverted cones move.

The movement of floating objects is limited to tilting around the center of gravity and the moment of inertia for each floating object needs to be added. The center of mass of a solid cone of uniform mass is located ¼ h_{cone} from the base along the center axis and the corresponding moment of inertia is given by

$$I_x = I_y = \frac{3}{80} m(h^2 + 4r^2) \,, \tag{C.5}$$

and

$$I_z = \frac{3}{10} mr^2 \,, \tag{C.6}$$

where m is the mass, h is the height of the cone, and r is the radius of the cone [19].

To accommodate the weighted apex of the inverted cone, the center of mass is set to ¼ h_{cone} from the apex. The parallel axis theorem [5] is used to calculate the moment of inertia around the offset center of mass

$$I_O = I + md^2 \,, \tag{C.7}$$

where I_O is the moment of inertia around the offset center of mass and d is the distance between the center of mass and offset center of mass. Thus, the moment of inertia for the weighted inverted cone becomes

$$I_{O,x} = I_x + md_z^2 \,, \tag{C.8}$$

$$I_{O,y} = I_y + md_z^2 \,, \tag{C.9}$$

and

$$I_{O,z} = I_z \,, \tag{C.10}$$

where d_x and d_y equal zero because the center of mass only changed in the z-direction and d_z is ½ h_{cone}.

VITA

Janna Christine Wai was born and raised in Renton, Washington. From an early age she developed an interest in airplanes, in part, due to her father who is an aeronautical engineer and graduate of the University of Washington. After completing high school, she entered the University of Washington and received a Bachelor of Science in 2009 and Master of Science in 2011 from the department of Aeronautics and Astronautics.